UNIVERSITY OF CALIFORNIA

Los Angeles

Feedback Control of Film Composition and Microstructure in High-κ Thin Film Growth

A dissertation submitted in partial satisfaction of the requirements for the degree of Doctor of Philosophy in Chemical Engineering

by

Dong Ni

2005

UMI Number: 3191405

INFORMATION TO USERS

The quality of this reproduction is dependent upon the quality of the copy submitted. Broken or indistinct print, colored or poor quality illustrations and photographs, print bleed-through, substandard margins, and improper alignment can adversely affect reproduction.

In the unlikely event that the author did not send a complete manuscript and there are missing pages, these will be noted. Also, if unauthorized copyright material had to be removed, a note will indicate the deletion.

UMI®

UMI Microform 3191405

Copyright 2006 by ProQuest Information and Learning Company.

All rights reserved. This microform edition is protected against unauthorized copying under Title 17, United States Code.

ProQuest Information and Learning Company
300 North Zeeb Road
P.O. Box 1346
Ann Arbor, MI 48106-1346

The dissertation of Dong Ni is approved.

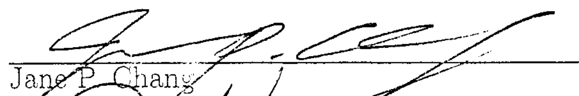

Jane P. Chang

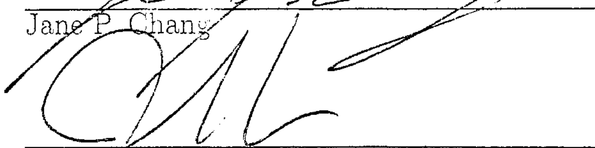

James F. Davis

Tsu-Chin Tsao

Panagiotis D. Christofides, Committee Chair

University of California, Los Angeles

2005

Contents

1 Introduction **1**

1.1 High-κ dielectrics 1

1.2 High-κ dielectric deposition techniques 2

1.3 Process control of semiconductor device fabrication 7

1.4 Dissertation structure 9

2 Real-Time Carbon Content Control for PECVD ZrO_2 Thin Film Growth **12**

2.1 Introduction 12

2.2 ECR high-density PECVD reactor 15

2.3 Optical emission spectroscopy system 18

2.4 Feedback control system: design and implementation 20

2.5 Experimental results and discussion 24

2.5.1 Open-loop system 24

2.5.2 Closed-loop system 28

2.5.3 XPS analysis 31

2.6 Conclusions 37

3 Dynamics and Control of Thin Film Surface Microstructure in a Complex Deposition Process **38**

3.1 Introduction 38

3.2 Surface microstructure model for thin film growth 41

3.2.1 Micro-process model 43

3.2.2 Simulation procedure 46

3.3 Simulation results and discussion 50

3.3.1 Single-component case 50

3.3.2 Multi-component case 56

3.3.3 Effect of gas phase composition 59

3.3.4 Effect of lattice size 60

3.4 Feedback control 61

3.4.1 Surface roughness control in the low temperature regime . 62

3.4.2 Surface roughness control in the high temperature regime . 67

3.5 Conclusions 76

4 Construction of Stochastic PDEs for Feedback Control of Surface Roughness in Thin Film Deposition **78**

4.1 Introduction 78

4.2 Preliminaries 81

4.2.1 Thin film growth process 81

4.2.2 Stochastic PDE model 83

4.3 Model construction 90

4.3.1 Eigenvalues and covariance 90

4.3.2 Dependence on the process parameters 94
4.3.3 Validation of stochastic PDE model 98
4.4 Feedback control 102
4.4.1 Surface roughness 102
4.4.2 Feedback control design 104
4.4.3 Closed-loop simulation 109
4.5 Conclusions 115

5 Multivariable Predictive Control of Thin Film Deposition Using a Stochastic PDE Model 117

5.1 Introduction 117
5.2 Preliminaries 118
5.2.1 Thin film growth process 118
5.2.2 Stochastic PDE model 121
5.3 Model construction 127
5.3.1 Eigenvalues and covariance 128
5.3.2 Dependence on the process parameters 131
5.3.3 Validation of stochastic PDE model 134
5.4 Feedback control 139
5.4.1 Predictive control design 140
5.4.2 Closed-loop simulations 146
5.5 Conclusions 149

6 Conclusions and Future Work 151

6.1 Conclusions 151

6.2 Future work 153

6.2.1 Deposition plasma diagnostic study and thin films characterizations 153

6.2.2 Real-time feedback control using multivariate regression model 156

6.2.3 Stochastic model-based control of thin film growth 158

Bibliography **159**

List of Figures

1.1 Ideal schematic of process flow: (a) exposure of precursor gas, (b) monolayer formation, (c) exposure to reactant gas, and (d) formation and pumping of volatile [60] products. 5

1.2 Illustration of the plasma-enhanced chemical vapor deposition process: (a) vaporization and introduction of reactant molecules (precursor and oxidant) into the reactor, (b) application of reactor operating conditions such as RF or microwave power, (c) electron impact on precursor molecules which lead to generation of radicals and ions, (d) radicals react with molecules to form final gaseous products, (e) diffusion of gaseous particles to the surface, (f) adsorption on surface, (g) surface reaction, (h) development of bulk film structure and properties. 6

2.1 Schematic diagram of the ECR plasma-enhanced CVD system used in this study. 16

2.2 Internal configuration of ECR PECVD chamber. 17

2.3 Block diagram of the closed-loop system under the proposed carbon content controller. 22

2.4 Experimental data of R_f vs. the γ_{ss} from different depositions for fixed argon flow rate 8 sccm, chamber pressure at 40 mTorr and microwave power 300 W. 25

2.5 Response curve of γ of step changes in R_f for argon flow rate 8 sccm, chamber pressure 40 mTorr and microwave power 300 W. . 26

2.6 Simulink representation for the process dynamics. 26

2.7 Evolutions of bulk (A) and surface (B) carbon concentration of a ZrO_2 film computed based on real-time OES measurements during an open-loop deposition with microwave power 300 W, chamber pressure 40 mTorr, Ar flow rate 8.4 sccm and O_2 flow rate 8 sccm. 27

2.8 Evolutions of C_2 and O optical emission intensity during an open-loop deposition with microwave power 300 W, chamber pressure 40 mTorr, Ar flow rate 8.4 sccm and O_2 flow rate 8 sccm. 27

2.9 Evolution of bulk (A) and surface (B) carbon concentration of a ZrO_2 film computed based on real-time OES measurements and profile of manipulated oxygen flow rate (C) during a controlled deposition experiment with microwave power 300 W, chamber pressure 40 mTorr and Ar flow rate 8.4 sccm. 29

2.10 Closed-loop deposition vs. open-loop deposition with same initial deposition condition of microwave power 300W, chamber pressure 40 mTorr, Ar flow rate 8.4 sccm and O_2 flow rate 6 sccm. 30

2.11 Simulated profiles of X_C (left) and f_{O_2} (right) of the closed-loop system with $K_p = 0.27$ (dotted line), $K_p = 0.53$ (dashed line) and $K_p = 0.80$ (solid line). 32

2.12 Simulated profiles of X_C (left) and f_{O_2} (right) of the closed-loop system with $\tau_p = 5$ (dotted line), $\tau_p = 10$ (dashed line) and $\tau_p = 15$ (solid line). 32

2.13 XPS survey spectra obtained from ZrO_2 thin films deposited by closed-loop deposition with set-point values of 1.4%, 1.9% and 2.5%. 33

2.14 Carbon 1s peaks of the XPS spectra obtained from ZrO_2 thin films deposited by closed-loop deposition with set-point values for carbon content of 1.4%, 1.9% and 2.5%. 34

2.15 Comparison of deconvoluted carbon-oxygen peaks in C(1s) XPS spectra obtained from ZrO_2 thin films deposited by closed-loop operation with set-point values of 1.4%, 1.9% and 2.5%. 35

2.16 XPS compositional analysis results for closed-loop deposited ZrO_2 thin films. 35

3.1 Thin film growth process. 42

3.2 Surface of a thin film deposited with $w_a^A = 0s^{-1}$, $w_a^B = 0.1s^{-1}$ and $T = 800$ K - $t = 550s$. 51

3.3 Surface roughness of thin films deposited with $w_a^A = 0s^{-1}$, $w_a^B = 0.1s^{-1}$ for different substrate temperature - $t = 550s$. 51

3.4 Surface of a thin film deposited with $w_a^A = 0.1s^{-1}$, $w_a^B = 0s^{-1}$ and $T = 640$ K - $t = 570s$. 52

3.5 Surface of a thin film deposited with $w_a^A = 0.1s^{-1}$, $w_a^B = 0s^{-1}$ and $T = 760$ K - $t = 570s$. 53

3.6 Surface roughness of thin films deposited with $w_a^A = 0.1s^{-1}$, $w_a^B = 0s^{-1}$ for different substrate temperature - $t = 570s$. 54

3.7 Surface roughness of thin films during depositions with a. $w_a^A = 0s^{-1}$, $w_a^B = 0.1s^{-1}$ and $T = 800\ K$ (solid line); b. $w_a^A = 0.1s^{-1}$, $w_a^B = 0s^{-1}$ and $T = 640\ K$ (dashed line); c. $w_a^A = 0.1s^{-1}$, $w_a^B = 0s^{-1}$ and $T = 760\ K$ (dotted line). 55

3.8 Surface of a thin film deposited with $w_a^A = 0.05s^{-1}$, $w_a^B = 0.05s^{-1}$ and $T = 640\ K$ - $t = 900s$. 56

3.9 Surface of a thin film deposited with $w_a^A = 0.05s^{-1}$, $w_a^B = 0.05s^{-1}$ and $T = 880\ K$ - $t = 900s$. 57

3.10 Surface roughness of thin films deposited with $w_a^A = 0.05s^{-1}$, $w_a^B = 0.05s^{-1}$ for different substrate temperature - $t = 900s$. 57

3.11 Surface roughness of the thin films deposited for different hopping to adsorption ratio in a. homogeneous deposition, $100\%A$ (solid line); b. heterogeneous deposition, $50\%A + 50\%B$ (dashed line). . 58

3.12 Surface roughness of thin films deposited with different gas phase compositions: a. $100\%A$ (solid line); b. $80\%A + 20\%B$ (dashed line); c. $50\%A + 50\%B$ (dotted line); d. $20\%A + 80\%B$ (dashed dotted line). 60

3.13 Surface roughness of thin films deposited with different substrate temperature computed using different simulation lattice size. . . . 61

3.14 Response of surface roughness with respect to step changes in substrate temperature: a. T changes from 640 K to 680 K at t=400 s (step 1); b. T changes from 640 K to 600 K at t=400 s (step 2). . 63

3.15 Response of surface roughness with respect to step disturbance in gas phase composition: a. gas phase composition changed from $50\%A + 50\%B$ to $70\%A + 30\%B$ (disturbance 1); b. gas phase composition changed from $50\%A + 50\%B$ to $30\%A + 70\%B$ (disturbance 2). 64

3.16 Block diagram of the closed-loop system. 65

3.17 Temperature and surface roughness profiles with surface roughness set-point value of $3.5ML$: a. closed-loop surface roughness (solid line, left scale); b. open-loop surface roughness (dashed line, left scale); c. substrate temperature (dotted line, right scale). 66

3.18 Temperature and surface roughness profiles with surface roughness set-point value of $3.5ML$ in the presence of disturbance: a. closed-loop surface roughness (solid line, left scale); b. open-loop surface roughness (dashed line, left scale); c. substrate temperature (dotted line, right scale). 67

3.19 Response of surface roughness with respect to step changes in substrate temperature: a. T changes from 740 K to 820 K at t=400 s (step 3); b. T changes from 740 K to 660 K at t=400 s (step 4). . 68

3.20 Response of surface roughness with respect to step changes in substrate temperature: a. T changes from 740 K to 820 K at t=200 s (step 5); b. T changes from 740 K to 660 K at t=200 s (step 6); c. T changes from 740 K to 820 K at t=800 s (step 7); d. T changes from 740 K to 660 K at t=800 s (step 8). 68

3.21 Response of surface roughness with respect to step disturbance in gas phase composition: a. gas phase composition changed from $50\%A + 50\%B$ to $80\%A + 20\%B$ (disturbance 3); b. gas phase composition changed from $50\%A + 50\%B$ to $20\%A + 80\%B$ (disturbance 4). 69

3.22 Temperature and surface roughness profiles with surface roughness set-point value of $3.2ML$: a. closed-loop surface roughness (solid line, left scale); b. open-loop surface roughness (dashed line, left scale); c. substrate temperature (dotted line, right scale). 70

3.23 Temperature and surface roughness profiles with surface roughness set-point value of $3.2ML$ in the presence of disturbance: a. closed-loop surface roughness (solid line, left scale); b. open-loop surface roughness (dashed line, left scale); c. substrate temperature (dotted line, right scale). 71

3.24 Temperature and surface roughness profiles with surface roughness set-point value of $3.2ML$ in the presence of disturbance: a. closed-loop surface roughness (solid line, left scale); b. open-loop surface roughness (dashed line, left scale); c. substrate temperature (dotted line, right scale). 72

3.25 Block diagram of the closed-loop system with the kMC model-predictive controller. 73

3.26 Temperature and surface roughness profiles with surface roughness set-point value of $3.2ML$: a. closed-loop surface roughness (solid line, left scale); b. reference surface roughness (dashed line, left scale); c. open-loop surface roughness (dotted line, left scale); d. substrate temperature (dashed dotted line, right scale). 75

3.27 Temperature and surface roughness profiles with surface roughness set-point value of $3.2ML$: a. closed-loop surface roughness (solid line, left scale); b. reference surface roughness (dashed line, left scale); c. open-loop surface roughness (dotted line, left scale); d. substrate temperature (dashed dotted line, right scale). 76

4.1 The thin film growth process. 81

4.2 Covariance profiles of z_{10}, z_{20}, z_{30} and z_{40}. 92

4.3 Eigenvalue spectrums of the infinite stochastic ODE systems identified from the kMC simulation of the deposition process with different lattice size: $k_{max} = 100$, $k_{max} = 500$, $k_{max} = 1000$ and $k_{max} = 2000$. 93

4.4 Eigenspectrums identified from simulated deposition processes with a growth rate $W = 0.5ML/s$ for different substrate temperatures: $T = 600K$, $T = 650K$ and $T = 680K$. 94

4.5 Covariance spectrums identified from simulated deposition processes with a growth rate $W = 0.5ML/s$ for different substrate temperatures: $T = 600K$, $T = 650K$ and $T = 680K$. 95

4.6 Eigenvalue spectrums identified from simulated deposition processes with a substrate temperature $T = 650K$ for different growth rates: $W = 0.5ML/s$, $W = 1.0ML/s$ and $W = 2.0ML/s$. 96

4.7 Covariance spectrums identified from simulated deposition processes with a substrate temperature $T = 650K$ for different growth rates: $W = 0.5ML/s$, $W = 1.0ML/s$ and $W = 2.0ML/s$. 97

4.8 Profile of c_2 as a function of substrate temperature T and thin film growth rate W. 97

4.9 Profile of ς^2 as a function of substrate temperature T and thin film growth rate W. 98

4.10 Final thin film surface profiles generated by kMC simulation and stochastic PDE model for a $1000s$ deposition with substrate temperature $T = 550K$, thin film growth rate $W = 0.1$ ML/s and lattice size $k_{max} = 2000$. 99

4.11 Final thin film surface profiles generated by kMC simulation and stochastic PDE model for a $400s$ deposition with substrate temperature $T = 700K$, thin film growth rate $W = 2.5$ ML/s and lattice size $k_{max} = 2000$. 99

4.12 Expected surface roughness profiles generated by kMC simulation and stochastic PDE model for a $1000s$ deposition with substrate temperature $T = 550K$, thin film growth rate $W = 0.1$ ML/s and lattice size $k_{max} = 2000$. 101

4.13 Expected surface roughness profiles generated by kMC simulation and stochastic PDE model for a 400s deposition with substrate temperature $T = 700K$, thin film growth rate $W = 2.5\ ML/s$ and lattice size $k_{max} = 2000$. 101

4.14 Block diagram of the closed-loop system. 104

4.15 Surface roughness and substrate temperature profiles of a 1000 s closed-loop deposition process with thin film growth rate $W = 0.5$ ML/s and final roughness setpoint $r_{set} = 1.0\ ML$. 110

4.16 Final thin film surface profile of a closed-loop and a open-loop depositions with the same initial substrate temperature $T = 650\ K$, thin film growth rate $W = 0.5\ ML/s$ and deposition length $t_{dep} = 1000\ s$.110

4.17 Histogram of final surface roughness of 100 closed-loop and 100 open-loop thin film depositions targeted at the same surface roughness level. 111

4.18 Surface roughness profile of the undisturbed open-loop deposition (dotted green line), and the surface roughness profile of the process under disturbance, of the open-loop deposition (dashed red line) and closed-loop deposition (solid black line). 113

4.19 Profiles of the process disturbance W, and the manipulated substrate temperature T (in closed-loop deposition). 113

4.20 Histograms of final surface roughness of thin films deposited with open-loop (with and without process disturbance) and closed-loop (with process disturbance) operations. 114

5.1 The thin film growth process. 119

5.2 Eigenvalue spectrum of the infinite stochastic ODE systems identified from the kMC simulation of the deposition process with $W = 0.5\ 1/s$, $T = 650\ K$ and $k_{max} = 100$. 130

5.3 Profile of $(W - c)/W$ as a function of substrate temperature T and adsorption rate W. 131

5.4 Profile of c_2 as a function of substrate temperature T and adsorption rate W. 132

5.5 Profile of $\varsigma^2/(\pi/k_{max})^2$ as a function of substrate temperature T for different adsorption rates. 133

5.6 Final thin film surface profiles generated by kMC simulation (left, $k_{max} = 100$) and stochastic PDE model (right, 20×20 states) for a $200s$ deposition with substrate temperature $T = 610\ K$ and adsorption rate $W = 0.5\ 1/s$. 135

5.7 Final thin film surface profiles generated by kMC simulation (left, $k_{max} = 100$) and stochastic PDE model (right, 20×20 states) for a $200s$ deposition with substrate temperature $T = 710\ K$ and adsorption rate $W = 0.5\ 1/s$. 136

5.8 Expected surface roughness profiles generated by kMC simulation ($k_{max} = 100$) and stochastic PDE model for a $200s$ deposition with substrate temperature $T = 610\ K$ and adsorption rate $W = 0.5\ 1/s$. 137

5.9 Expected surface roughness profiles generated by kMC simulation ($k_{max} = 100$) and stochastic PDE model for a $200s$ deposition with substrate temperature $T = 710\ K$ and adsorption rate $W = 0.5\ 1/s$. 138

5.10 Expected thin film thickness profiles generated by kMC simulation (k_{max} = 100) and stochastic PDE model for: 1) a 200s deposition with substrate temperature T = 610 K and adsorption rate W = 0.5 1/s (the thin lines); 2) a 200s deposition with substrate temperature T = 710 K and adsorption rate W = 0.5 1/s (the thick lines). 138

5.11 Block diagram of the closed-loop system. 140

5.12 Surface roughness and substrate temperature profiles of a 200 s closed-loop deposition process with a thickness setpoint of 100 ML and a final roughness setpoint r_{set} = 1.5 ML; the initial deposition conditions are T = 610 K and W = 1.0 1/s. 147

5.13 Thickness and surface adsorption rate profiles of a 200 s closed-loop deposition process with a thickness setpoint of 100 ML and a final roughness setpoint r_{set} = 1.5 ML; the initial deposition conditions are T = 610 K and W = 1.0 1/s. 147

5.14 Histogram of final surface roughness of 100 closed-loop and 100 open-loop thin film depositions targeted at the same surface roughness level. 148

6.1 Major optical emission peaks and bands of a $ZTB/Ar/O_2$ plasma at pressure of 40 mTorr, microwave power of 300 W, and O_2/Ar flow rate ratio of 2 with no substrate bias or heating, and no silicon wafer. 154

6.2 Mass spectra from a ZTB/Ar/O2 plasma [14] at pressure of 40 mTorr, microwave power of 300 W, and O_2/Ar flow rate ratio of 4. a) Neutral mass spectrum obtained by repelling plasma ions with an extractor potential of +35 V. b) Ion mass spectrum obtained by direct extraction of plasma ions with ionization filaments turned off and an extractor potential of -2 V. 155

6.3 XPS spectra of a ZrO_2 thin film. 157

List of Tables

1.1 Comparison of relevant properties for high-κ material candidates. 3

2.1 Optical emission spectroscopy (OES) channel configurations of wavelength range, start pixel (SP), end pixel (EP) and resolution (in full width at half maximum [FWHM]). 19

2.2 Transitions and wavelengths of atomic emissions observed [64]. . . 19

2.3 Transitions and wavelengths of molecular emissions observed [54]. 20

2.4 XPS atomic sensitivity factors (ASF). 33

3.1 Model parameters. 46

ACKNOWLEDGEMENTS

This dissertation would not have ever existed if there had not been the foresighted guidance and generous help from my advisor Professor Panagiotis Christofides, I would like to express my deepest thankfulness to him, and I feel even more grateful for the things I learned from him, beyond scientific and engineering techniques, but tactics and philosophy towards research.

I would like to thank my talented coworkers in our research group, especially Dr. Yiming Lou and Dr. Dan Shi, for their plentiful contributions and sustained support. I feel so glad that we come together from the other side of the planet made all those great things possible.

I would like to thank Professor Jane Chang as my knowledgable mentor in experimental research, I would also like to thank the students in her research group that I worked with for their intellectual contributions and wonderful company.

I would like to thank Professor James Davis and Professor Tsu-Chin Tsao for agreeing to serve on my thesis committee.

I would like to thank all my friends in Los Angeles and in China, you are my fountain of power and happiness.

Finally, I would like to express my ineffable gratitude to my parents, the most fortunate and blessed thing that ever happens to me is being your child.

VITA

1978	Born, Hangzhou, China
2001	B. Eng., Control Science & Engineering Zhejiang University Hangzhou, China
2002	M. S., Chemical Engineering University of California, Los Angeles Los Angeles, California
2001-05	Graduate Student Department of Chemical Engineering University of California, Los Angeles Los Angeles, California
2004	O. Hugo Shuck Best Paper Award from American Automatic Control Council

PUBLICATIONS

Lou, Y., D. Ni, P. D. Christofides and J. P. Chang, "Modeling and Control of Surface Roughness in a PECVD Reactor," *AIChE Annual Meeting*, paper 261g, Indianapolis, Indiana, 2002.

Ni, D., Y. Lou, P. D. Christofides, L. Sha, , S. Lao and J. P. Chang, "A Method for Real-Time Control of Thin Film Composition Using OES and XPS," *Proceedings of American Control Conference*, 1320-1327, Denver, Colorado, 2003.

Ni, D., Y. Lou, P. D. Christofides, L. Sha, S. Lao and J. P. Chang, "Real-Time Control of High-k Dielectric Thin Film Composition and Thickness," *AIChE Annual Meeting*, paper 176d, San Francisco, California, 2003.

Ni, D., Y. Lou, P. D. Christofides, L. Sha and J. P. Chang,, "Real-Time Feedback Control of Carbon Content of Zirconium Dioxide Thin Films Using Optical Emission Spectroscopy," *Proceedings of 5th International Symposium on Advanced Control of Chemical Processes*, 615-620, Hong Kong, P. R. China, 2004.

Ni, D., Y. Lou, P. D. Christofides, L. Sha, S. Lao and J. P. Chang, "Real-Time Carbon Content Control for PECVD ZrO_2 Thin-Film Growth," *IEEE Transactions on Semiconductor Manufacturing*, **17**, 221-230, 2004.

Ni, D. and P. D. Christofides, "Predictive Control of Thin Film Microstructure in a Complex Deposition Process," *Proceedings of 7th IFAC Symposium on Dynamics and Control of Process Systems*, 6 pages, Boston, Massachusetts, 2004.

Ni, D. and P. D. Christofides, "Constructing Linear Stochastic PDE Models for Thin Film Growth Processes," *AIChE Annual Meeting*, paper 441b, Austin, Texas, 2004.

Ni, D. and P. D. Christofides, "Multivariable Predictive Control of Thin Film Deposition Using a Stochastic PDE," *AIChE Annual Meeting*, paper 434b, Austin, Texas, 2004.

Ni, D. and P. D. Christofides, "Dynamics and Control of Thin Film Microstructure in a Complex Deposition Process," *Chemical Engineering Science*, **60**, 1603-1617, 2005.

Ni, D. and P. D. Christofides, "Multivariable Predictive Control of Thin Film Deposition Using a Stochastic PDE," *Industrial & Engineering Chemistry Research*, in press, 2005.

Ni, D. and P. D. Christofides, "Multivariable Predictive Control of Thin Film Deposition Using a Stochastic PDE," *Proceedings of the American Control Conference*, to appear, Portland, Oregon, 2005.

Ni, D. and P. D. Christofides, "Construction of Stochastic PDEs for Feedback Control of Surface Roughness in Thin Film Growth," *Proceedings of the American Control Conference*, to appear, Portland, Oregon, 2005.

Ni, D. and P. D. Christofides, "Construction of Stochastic PDEs for Feedback Control of Surface Roughness in Thin Film Deposition," *International Journal of Robust & Nonlinear Control*, accepted, 2005.

ABSTRACT OF THE DISSERTATION

Feedback Control of Film Composition and Microstructure in High-κ Thin Film Growth

by

Dong Ni

Doctor of Philosophy in Chemical Engineering

University of California, Los Angeles, 2005

Professor Panagiotis D. Christofides, Chair

Fabrication of smaller feature size metal-oxide-semiconductor (MOS) devices typically requires tight control of thin film properties such as film composition and microstructure. In this dissertation, the implementation of feedback control on chemical vapor deposition (CVD) processes (especially for high-κ materials) is studied to control variables such as impurity concentration, thickness and surface roughness.

Initially, we present a methodology for real-time control of thin film carbon content (which is considered as impurity in the film) in a plasma-enhanced chemical vapor deposition (PECVD) process using combination of on-line gas phase measurements obtained through optical emission spectroscopy (OES) and off-line (ex-situ) measurements of film composition obtained via x-ray photoelectron spectroscopy (XPS). Using this approach, a real-time control system is developed and implemented on an experimental high density PECVD system to demonstrate

the effectiveness of real-time feedback control of carbon content. Experimental results of depositions and XPS analysis of deposited thin films demonstrate the advantages of operating the process under real-time feedback control in terms of robust operation and lower carbon content.

Then, motivated by recent experimental results on the growth of high-κ dielectric thin films using PECVD, a multi-component kinetic Monte Carlo (kMC) model is developed for a conceptual deposition process which involves multiple gas phase species and is influenced by both short-range and long-range interactions. The dependence of the surface microstructure of the thin film on the deposition conditions is studied. Furthermore, kMC model-based feedback control schemes which use the substrate temperature to control the final surface roughness of the thin film are proposed.

Since kMC models are not available in closed-form and computationally expensive, we develop a systematic method for the construction of linear stochastic partial differential equation (PDE) models for feedback control of surface microstructure in thin film deposition. A linear stochastic PDE model is constructed for a generic one-dimensional thin film deposition process using surface snapshots generated by kMC simulations. An optimization-based feedback controller is designed using the constructed stochastic PDE model and applied to the kMC simulation of the deposition process to control the surface roughness.

This stochastic PDE approach is then extended to two-dimensional case and applied to multivariable control problems. A 2D linear stochastic PDE model is initially constructed which describes the spatio-temporal evolution of the film surface. A multivariable predictive control algorithm is developed which uses a finite-dimensional approximation of the stochastic PDE model to regulate the thin

film thickness and surface roughness at desired levels at the end of the deposition.

Chapter 1

Introduction

1.1 High-κ dielectrics

The decrease of device dimensions has motivated the need for oxides with high dielectric constant (κ) to replace silicon dioxide as a dielectric in metal oxide semiconductor (MOS) devices. This is because for silicon dioxide layers thinner than about 1.6 nm, direct tunnelling currents through the oxide result in an exponential increase of leakage current. Significant leakage current increases the power dissipation and deteriorates the device performance and circuit stability for VLSI circuits [32, 39, 74]. For example a complementary MOS (CMOS) device below 70 nm in gate length will need an oxide thickness of less than 1.5 nm, which correspond to three layers of silicon dioxide atoms. Significant quantum mechanical tunnelling current and the early breakdown of the thin gate dielectric will degrade the reliability of the device. In addition, the minimum dimension of capacitors for 1-4 Gb dynamic random access memory (DRAM) generations falls into the deep sub-micron range, it is questionable whether acceptable capacitors can be fabricated with silicon based materials within such small size regime.

The alternative is to use thicker layers if a "new" high-κ dielectric, with the same equivalent silicon dioxide thickness or capacitance. A large number of high-κ candidate materials have been extensively studied. Table 1.1 shows a list of the most important high-κ materials and their properties. Among the candidate materials listed in Table 1.1, Y_2O_3 and Al_2O_3 have many favorable properties, but their dielectric constants are only 2-3 times larger than SiO_2, and therefore do not offer significant advantages over SiO_2. Although TiO_2 and Ta_2O_5 have considerably high dielectric constants, the instability of TiO_2 on Si and the high leakage current level of Ta_2O_5 film require an additional barrier layer to prevent their reaction or with interdiffusion into silicon. The additional barrier layer will increase the process complexity and limit the scalability of the gate stack.

ZrO_2(as well as HfO_2) has several important properties which make it a leading candidate for an alternative dielectric. The reported dielectric constant is relatively high among the binary-metal oxides ($\kappa \sim 25$). The thermal stability on Si is very good. Reports have indicated that pure ZrO_2 next to Si (with an ultra thin intervening SiO_x layer) remain stable up to 900°C [18]. In addition, ZrO_2 films have superior chemical resistance, good mechanical strength, and a low leakage current level. This work is intended to develop a real-time controller to deposit high quality ZrO_2 thin films in order to fabricate a higk-κ and low leakage current level dielectric.

1.2 High-κ dielectric deposition techniques

A variety of techniques are available today to prepare metal oxide thin films. In general, these techniques can be classified into two main categories: physical vapor deposition (PVD) and chemical vapor deposition (CVD). Moreover, metal oxide

Table 1.1: Comparison of relevant properties for high-κ material candidates.

Dielectric Material	Dielectric Constant	E_{BD} (MV/cm)	E_g(eV)	Crystal Structure(s)
SiO_2	3.9	12-15	8	Amorphous
Si_3N_4	7-9	10-11	5	Amorphous
TiO_2	80-120	0.5	4	Tetragonal (rutile, anatase)
Y_2O_3	12-15	4-5	6	Cubic
Al_2O_3	9-12	10	8	Amorphous
Ta_2O_5	20-25	3-5	3-4	Orthorhombic
ZrO_2	15-22	15-20	5-7	Monoclinic, tetragonal, cubic
HfO_2	25	-	5-7	Monoclinic, tetragonal, cubic

thin films can also be formed by atomic layer deposition (ALD) [58] and the Sol-Gel process [10]. Usually, thin film deposition takes place in a vacuum chamber. Practically, most deposition processes occur in a pressure from $10^3 Pa$ to $10^{-9} Pa$.

A typical example of PVD techniques is molecular beam epitaxy (MBE). Epitaxy means that the crystal structure is the same to the crystal structure of the substrate. MBE has been widely accepted for epitaxial deposition of a variety of materials. Examples include the growth of Si layers on Si substrate, the growth of ZnO layers on sapphire and the growth of high-temperature superconductors. MBE takes place in an ultra-pure, ultra-high vacuum atmosphere to keep the growth free from contaminants. The source species are heated to generate and deposit a flux of atoms or molecules to the substrate. The mean free paths of the particles are long enough to prevent collision of the particles on their way to the substrate. MBE allows the deposition of high-purity films.

Chemical Vapor Deposition (CVD) involves chemical reactions, which modify the gas phase precursors in into solid material which is subsequently deposited on the substrate. Compared to MBE, much higher deposition rates can be achieved

by CVD.

The atomic layer deposition (ALD) method is a deposition technique to improve the combined problems of the physical vapor deposition and chemical vapor deposition. ALD occurs in time-separated steps which are intrinsically self-limited by the nature of the process. The ALD method has a lot of advantages over other deposition methods such as excellent thickness uniformity over large substrate areas, conformality, low-processing temperature, low-impurities content, and completely precise thickness control [59, 68, 65].

A simplified schematic of the process flow is shown in Fig.1.1(a)-(d) [60]. The first ALD step is the exposure of a clean surface to the precursor gas. Then the precursor gas is evacuated from the chamber, while forming approximately 1 monolayer of surface coverage everywhere in the chamber. The physisorbed monolayer film is moderately stable with time on the surface and does not strongly depend on the deposition conditions. After that, a second reactant species is introduced in the gas phase and the adsorbed monolayer. Under the appropriate conditions, the reaction occurs with all of the adsorbed surface molecules, resulting in the formation of volatile product molecules, which are then pumped away in the gas phase, leaving behind a single layer, generally less than a monolayer, of the desired material on the film surface.

Rapid thermal chemical vapor deposition, plasma-enhanced chemical vapor deposition (PECVD) and low-pressure chemical vapor deposition are the most widely used methods of chemical vapor deposition. Since CVD has the advantage over PVD in terms of step coverage, and much higher production rate then ALD, CVD is preferred for fabrication of dynamic random access memory (DRAM) capacitor, in which conformity of as-deposited film on high-aspect ratio structure

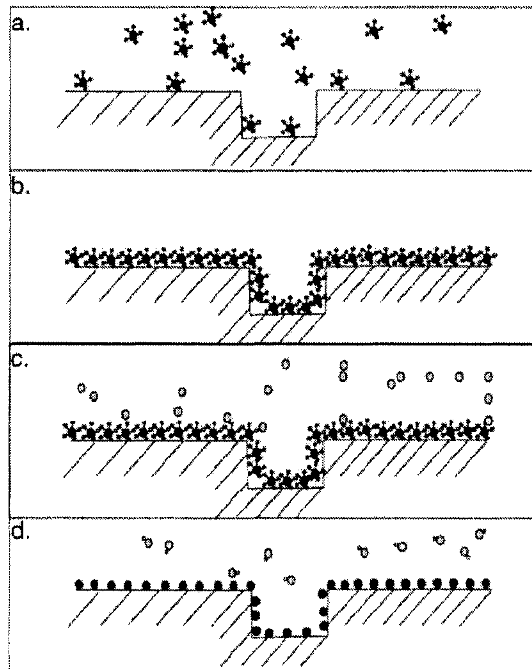

Figure 1.1: Ideal schematic of process flow: (a) exposure of precursor gas, (b) monolayer formation, (c) exposure to reactant gas, and (d) formation and pumping of volatile [60] products.

is important as well as fabrication costs.

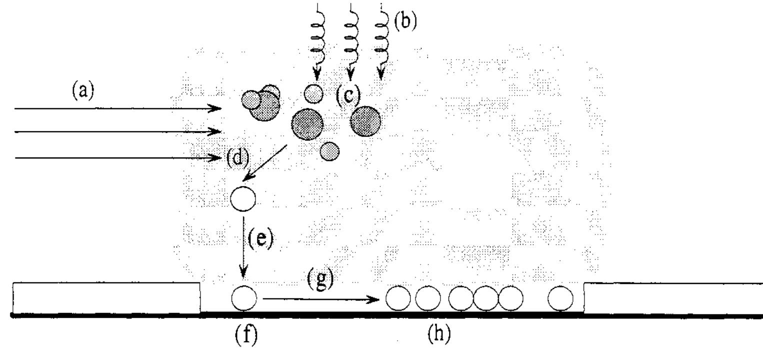

Figure 1.2: Illustration of the plasma-enhanced chemical vapor deposition process: (a) vaporization and introduction of reactant molecules (precursor and oxidant) into the reactor, (b) application of reactor operating conditions such as RF or microwave power, (c) electron impact on precursor molecules which lead to generation of radicals and ions, (d) radicals react with molecules to form final gaseous products, (e) diffusion of gaseous particles to the surface, (f) adsorption on surface, (g) surface reaction, (h) development of bulk film structure and properties.

The PECVD technique is one of the most prominent means of preparing dielectric thin films because of such advantages as low process temperature, high film growth rate, and wide flexibility of deposition conditions. The low temperature operation can prevent the diffusion of shallow junctions and reduced thermal strain leading to defect generation [26]. The basic mechanism of PECVD is that the energetic electrons provide the energy to the precursor undergoing decomposition and generating reactive species, rather than relying on the thermal energy to initiate chemical reactions. Thus, the PECVD process operates at low temperature which circumvent the problem of heating of the substrate surface.

The general plasma deposition process may involve a series of steps represented by Fig.1.2. Specifically it involves: (a) vaporization and introduction of reactant molecules (precursor and oxidant) into the reactor; (b) application of reactor

operating conditions such as RF or microwave power; (c) electron impact on precursor molecules which lead to generation of radicals and ions; (d) radicals react with molecules to form final gaseous products; (e) diffusion of gaseous particles to the surface; (f) adsorption on surface; (g) surface reaction; (h) development of bulk film structure and properties.

Gas phase reactions during PECVD are highly complex since the energetic electron is potentially capable of breaking every chemical bond and the resultant free radicals can recombine to form new molecules. However, progress has been made in recent years and it has been discovered that by varying process conditions, the plasma chemistry can be controlled, which, in turn, can allow controlling in real-time thin film properties. In fact, controlling the film properties is not only feasible but may also greatly improve electrical performance of devices since device performance is strongly dependent on properties of the film it is built on.

1.3 Process control of semiconductor device fabrication

Process control has been used in semiconductor device fabrication ever since the advent of the industry. Problems can be divided into four categories [38]; plant management, contamination control, materials handling, and unit operations control. Much attention has been focused on coordinating the schedules of different unit operations, controlling the purity of the required reactants, and monitoring the transfer of wafers between machines. Relatively less effort has been devoted to improving the control of individual unit operations.

The main unit operations are crystal growth, oxidation, deposition (dielectrics, silicon, metals), physical vapor deposition, dopant diffusion, dopant ion implantation, photolithography, etching, and chemical-mechanical polishing [66]. The

primary focus of modelling and control studies has been on lithography, deposition, and etching. A recent review of plasma etch, deposition, and lithography modelling and control covering work before 1994 has been presented by Badgwell et al [6].

Currently, process control in microelectronics manufacturing consists mainly of PI (proportional-integral) controllers executing fixed process recipes without feedback of important process outputs. While statistical process control has been adopted in most wafer fabrication facilities, automatic process control has not been implemented on a large scale. This is because in-situ measurements of important process variables are rarely available and the understanding of the process is so poor that it is often difficult to determine which variables should be included in a control scheme. Moreover, processing mistakes cannot be blended away and a processing error can destroy an entire batch of wafers with no hope of recovering the product through further processing.

However, the recent development of in-situ metrology and improved understanding of fabrication processes, as well as the need to reduce cost by improving process operation motivates the development and implementation of real-time feedback control systems on manufacturing processes to achieve much higher levels of accuracy and reduced variation in key quality variables. Several works had been published on real-time feedback control of deposition processes of III-V compound semiconductors using in-situ metrologies where target film properties can be measure directly in real-time [25, 73]. Based on first-principle modelling, model-based feedback control on rapid thermal processing has also been studied [8]. However, for most processes where direct in-situ measurements are not available and little is known of the complex process dynamics, not much have been

done.

More recently, motivated by the growing industrial demands, there have been significant research efforts focusing on modelling and control of thin film growth in order to obtain thin films with well-defined microstructure. In a thin film growth process, the film is directly formed from microscopic random processes (e.g., molecule adsorption, desorption, migration and surface reaction). Precise control of film properties requires models that describe these microscopic processes and directly account for their stochastic nature. Examples of such models include: 1) kinetic Monte-Carlo (kMC) methods [29, 23, 33], and 2) stochastic partial differential equations (PDEs) [20, 72].

1.4 Dissertation structure

In this dissertation, the implementation of feedback control chemical vapor deposition processes is studied to control the principal properties of thin films (especially for high-κ materials) such as thickness, composition and surface roughness to enable the fabrication of smaller feature size devices.

In Chapter 2, we present a methodology for real-time control of thin film carbon content in a PECVD process using combination of on-line gas phase measurements obtained through optical emission spectroscopy (OES) and off-line (ex-situ) measurements of film composition obtained via x-ray photoelectron spectroscopy (XPS). Using this approach, a real-time control system is developed and implemented on an experimental high density PECVD system to demonstrate the effectiveness of real-time feedback control of carbon content. Experimental results of depositions and XPS analysis of deposited thin films demonstrate the advantages of operating the process under real-time feedback control in terms of robust

operation and lower carbon content.

Motivated by recent experimental results on the growth of high-κ dielectric thin films using PECVD, a multi-component kinetic Monte Carlo (kMC) model is developed in Chapter 3 for a conceptual deposition process which involves multiple gas phase species and is influenced by both short-range and long-range interactions. The dependence of the surface microstructure of the thin film on the deposition conditions is studied. Furthermore, kMC model-based feedback control schemes which use the substrate temperature to control the final surface roughness of the thin film are proposed. The closed-loop simulation results demonstrate that robust deposition with controlled thin film surface roughness can be achieved under a kMC estimator-based proportional-integral (PI) feedback controller in the short-range interaction dominated growth regime, while a kMC model-predictive controller is needed to control the surface roughness in the long-range interaction dominated growth regime.

Since kMC models are not available in closed-form and computationally expensive, a systematic method for the construction of linear stochastic partial differential equation (PDE) models for feedback control of surface microstructure in thin film deposition is presented in Chapter 4. A linear stochastic PDE model is constructed for a generic one-dimensional thin film deposition process using surface snapshots generated by kMC simulations. An optimization-based feedback controller is designed using the constructed stochastic PDE model and applied to the kMC simulation of the deposition process to control the surface roughness.

The stochastic PDE approach presented in Chapter 4 is then extended to two-dimensional case and applied to multivariable control problems in Chapter 5. A 2D linear stochastic PDE model is initially constructed which describes the

spatio-temporal evolution of the film surface. A multivariable predictive control algorithm is developed which uses a finite-dimensional approximation of the stochastic PDE model to regulate the thin film thickness and surface roughness at desired levels at the end of the deposition. The predictive controller is then applied to the kinetic Monte-Carlo (kMC) simulation of the deposition process. Closed-loop system simulation results demonstrate that the model is adequately accurate and that the controller is effective in enforcing the desired control objectives and reducing film variance.

Chapter 2

Real-Time Carbon Content Control for PECVD ZrO_2 Thin Film Growth

2.1 Introduction

The decrease of microelectronic device dimensions has motivated the replacement of silicon dioxide with oxides of higher dielectric constant (κ) as a dielectric layer in metal oxide semiconductor (MOS) devices. This is because for silicon dioxide layers thinner than about 1.6 nm, direct tunnelling currents through the oxide result in an exponential increase of leakage current. Significant leakage current increases the power dissipation and deteriorates the device performance and circuit stability for very large scale integrated (VLSI) circuits [32, 39]. In addition, since the minimum dimension of capacitors for 1-4 Gb dynamic random access memory (DRAM) generations falls into the deep sub-micron range, it is questionable whether acceptable charge storage can be achieved with SiO_2 within such small size regime.

The alternative is to use layers of a "new" high-κ dielectric, with the same equivalent oxide thickness or capacitance. A large number of high-κ candidate materials have been extensively studied. Among these candidate materials, ZrO_2 (as well as HfO_2) has several important properties which make it a leading candidate for an alternative dielectric. The dielectric constant of ZrO_2 is relatively high among the binary-metal oxides ($\kappa \sim 25$), and its thermal stability on Si is very good. Moreover, studies have indicated that pure ZrO_2 next to Si (with an ultra thin intervening SiO_x layer) remains stable up to 900°C [18]. In addition, ZrO_2 films have superior chemical resistance, good mechanical strength and a low leakage current level.

A variety of techniques can be used to prepare metal oxide thin films. PECVD is one of the most prominent means of preparing dielectric thin films, especially for memory devices applications, because of such advantages as low process temperature, high film growth rate and wide flexibility of deposition conditions. The use of metal-organic (MO) chemicals as precursors in PECVD of metal oxide thin films enables uniform film growth over large areas and complex surface geometries. However, a potential problem of using MO precursors is the possibility of incorporation of impurities in the deposited thin film. One of the most important impurity species is carbon, which is abundant in the precursors. The incorporation of high concentration of carbon in the deposited film can adversely influence device performance by changing the dielectric constant and the leakage current density [11].

In general, carbon can be incorporated in the films either by forming carbides or oxides with the deposited metal or oxygen or by occupying intergranular positions among the grains of the main deposited compound in the form of cyclic or aliphatic

species. Carbon incorporation can even occur simultaneously in multiple states depending on precursor, material to-be-deposited and operating conditions [69, 47]. Therefore, the development and implementation of real-time feedback control systems for carbon content control could improve the operation and use of MO precursors in the deposition of high-κ materials.

Previous research on control of deposition processes has addressed control of film thickness in PECVD silicon epitaxy [75] and control of deposition spatial uniformity in PECVD amorphous silicon growth [3] (see also [2] for results on feedback control of plasma etching and [15] for results on feedback control of rapid thermal processing, as well as [40] and [41] for results on feedback control of thin film surface roughness). Recently, a method for real-time control of PECVD silicon nitride film properties for a relatively simple deposition chemistry was proposed in [34]; in this work, thin film properties were indirectly controlled by regulating gas phase species compositions. At this stage, direct control of PECVD thin film properties has not been reported due to the complexity of both plasma physics and plasma chemistry and the difficulty to obtain real-time measurements of film properties.

Optical emission spectroscopy (OES) has been widely used to monitor the gas phase species concentrations [17]. Moreover, OES has been used as measurement sensor for closed-loop control to regulate process variables such as the partial pressure of gas phase species[55, 22], and the film thickness based on empirical correlations [22]. However, although many researchers have suggested that OES signals could be utilized to control material properties such as thin film composition [13, 31], no work has been done to design and implement a real-time feedback control system using combination of OES real-time measurements and

off-line XPS measurements to directly control the thin film composition and to verify the closed-loop performance by characterization of the deposited thin films.

In this chapter, we present a methodology for real-time control of thin film carbon content in a plasma-enhanced metal-organic chemical vapor deposition process using combination of on-line gas phase measurements obtained through OES and off-line (ex-situ) measurements of film composition obtained via XPS. The method is used for real-time control of carbon content of ZrO_2 thin films. Initially, an estimation model of carbon content of ZrO_2 thin films based on real-time optical emission spectroscopy data is presented. Then, a feedback control scheme, which employs the proposed estimation model and a proportional-integral controller, is developed to achieve carbon content control. Using this approach, a real-time control system is developed and implemented on an experimental electron cyclotron resonance (ECR) high density plasma-enhanced chemical vapor deposition system to demonstrate the effectiveness of real-time feedback control of carbon content. Experimental results of depositions and XPS analysis of deposited thin films under both open-loop and closed-loop operations are shown and compared. The advantages of operating the process under real-time feedback control in terms of robust operation and lower carbon content are demonstrated.

2.2 ECR high-density PECVD reactor

The schematic of the experimental ECR PECVD reactor system is shown in Fig.2.1. It consists of an ECR type microwave source, a reactor chamber, a pumping system, a pressure control system, a gas delivery system, an OES system and a computer-based real-time process control system.

Fig.2.2 shows the internal configuration of the reactor chamber. A 6-inch-

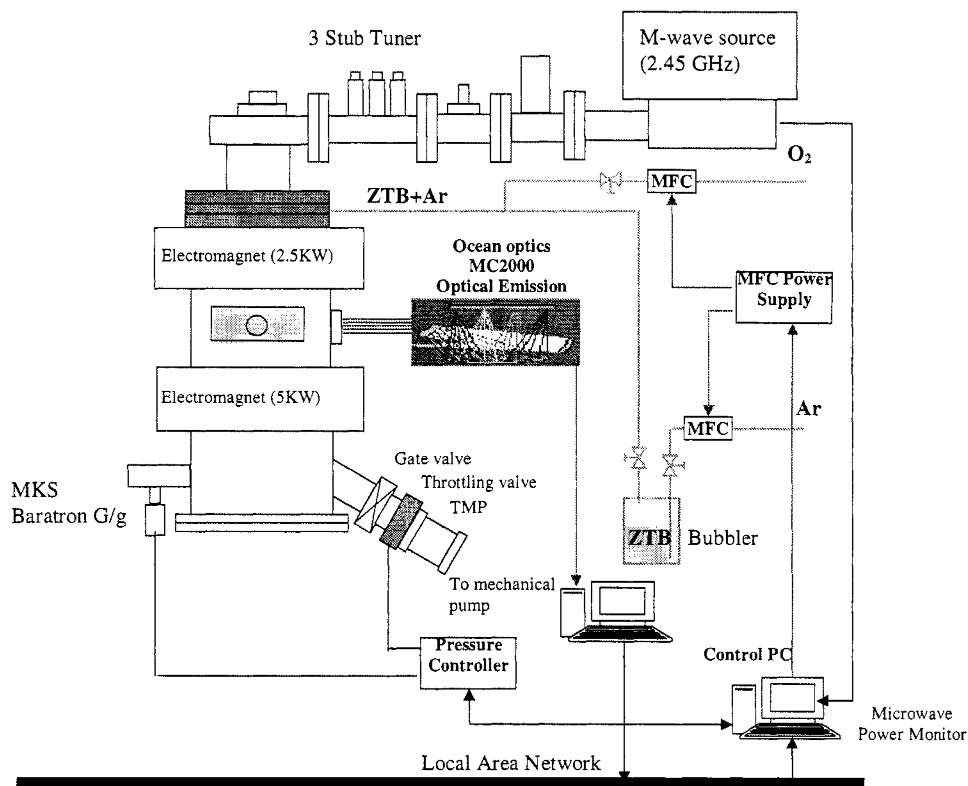

Figure 2.1: Schematic diagram of the ECR plasma-enhanced CVD system used in this study.

diameter cylindrical stainless-steel chamber is surrounded by two circular coaxial electromagnets, which are 7 inches apart. An ASTeX ECR source is on top of the chamber. Microwave at 2.45 GHz is generated from the source and transmitted into the chamber through a 3/8-inch thick vacuum-sealed quartz window and a high-density plasma is generated. A gas diffusion ring is located just below the top quartz window to conduct uniform distribution of the gases. A 4 inch-diameter anodized aluminum substrate holder is centered inside the chamber. The distance between the substrate holder and the top quartz window is adjustable in the range of 6.5 inches to 12 inches. The substrate holder is also connected with a 13.56 MHz radio frequency (RF) power supply tuned by a matching network; this allows controlling the ion impinging energy by applying bias voltage to the substrate.

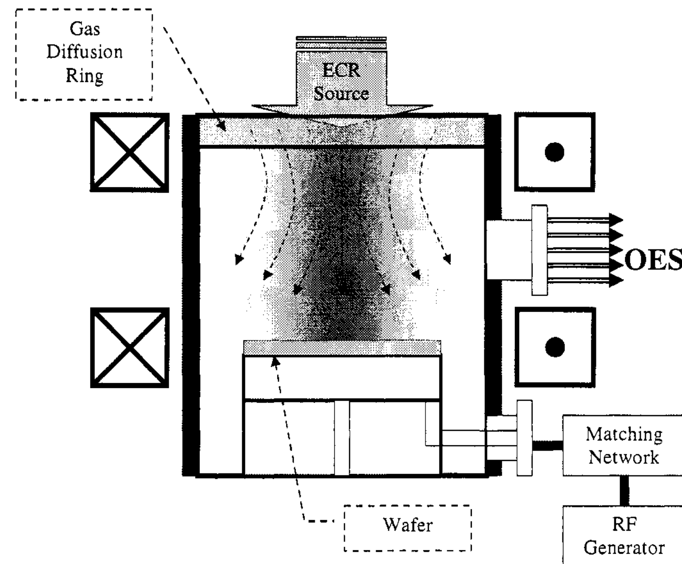

Figure 2.2: Internal configuration of ECR PECVD chamber.

The chamber is pumped by a 140 l/s Alcatel 5150CP turbo-molecular pump (TMP) backed by a mechanical pump. The base pressure is measured with an HPS I-Mag cold cathode ion gauge. The chamber pressure can be controlled and varied between the base pressure and atmospheric pressure. The MKS 651C

pressure controller takes the measurement of chamber pressure by an MKS 626A Baratron gauge as input and manipulates an MKS 253B throttle valve, thereby allowing to control the pressure independently from the gas flow rates.

We chose zirconium tetra-tert-butoxide $[Zr(OC_4H_9)_4]$ (ZTB) as our MO precursor because it has a sufficiently high vapor pressure (0.26 mbar at 60 ^oC) [26]. A bubbler, which is kept at constant temperature (65 ^oC), is used for precursor delivery because ZTB is a liquid at room temperature (boiling point=90 ^oC). Ar is used as a carrier gas of the precursor vapor and the gas line is heated to 80 ^oC to prevent the condensation of precursors. O_2 is used as an oxidant and mixed with Ar and ZTB at a point 8 inches away from the entrance to the reactor.

Throughout this study, the electric currents are fixed at 120 A for the 5 kW top magnet and 150 A for the 2.5 kW bottom magnet. The distance between the top quartz window and the substrate holder is kept constant at 6.5 inches and no bias is applied to the substrate.

2.3 Optical emission spectroscopy system

Optical emission spectroscopy (OES) is the central real-time measurement tool used in this study. We use an Ocean Optics MC2000 OES system with five channels covering the wavelength range from 200 nm to 1000 nm to analyze the plasma. Each channel consists of independent optic setups including slits, gratings, a 2048-element linear silicon charged coupled diode (CCD) array and an optic fiber cable. The configurations of individual channels are shown in Table 2.1. The best optical resolution [full width at half maximum] for this system is 1.4 Å with a 10 μm slit width in the ultraviolet (UV) range. The integration time can be set within the range of 3 ms to 60 s. A sapphire window with minimal UV absorption is used

as the OES port. The transmittance of the window does not vary significantly during each deposition run and the window is cleaned regularly to prevent accumulation of material on chamber walls. The emission spectra are taken 1 in. above the substrate surface in this study so that gas phase information near the wafer surface can be collected.

Table 2.1: Optical emission spectroscopy (OES) channel configurations of wavelength range, start pixel (SP), end pixel (EP) and resolution (in full width at half maximum [FWHM]).

CH	Range (nm)	SP	EP	Res.[FWHM]
0	196.14 ~ 354.44	4	2044	1.5Å
1	327.23 ~ 464.27	0	2047	1.4Å
2	437.93 ~ 617.89	0	2047	1.8Å
3	585.70 ~ 868.81	0	2046	2.8Å
4	786.50 ~ 1039.51	1	2047	2.5Å

Table 2.2: Transitions and wavelengths of atomic emissions observed [64].

Species	Wavelength (nm)	Transition
Ar	750.39	${4s'_{(1/2)}}^o - 4p'_{(1/2)}$
C	247.85	$2p^2\,{}^1S - 3s^1 4P^o$
H_β	486.13	$2p^2 P^o - 4d^2 D$
O	777.42	$3s^5 S^o - 3p^5 P$
Zr	350.93	
	351.96	
Zr^+	339.20	N/A
	343.82	
	349.62	

The major atomic emission peaks and molecular band heads observed in this study are summarized in Table 2.2 and Table 2.3, respectively. The analog signals produced by optical channels are captured by an Ocean Optics ADC1000

high-speed ISA-bus A/D converter installed in a Pentium PC. The OES data are then transmitted through fast ethernet to the computer used for real-time process control.

Table 2.3: Transitions and wavelengths of molecular emissions observed [54].

Species	Wavelength (nm)	Transition
C_2	516.52	$A^3\Pi_g - X^3\Pi_u$
CH	431.42	$A^2\Delta - X^2\Pi$

2.4 Feedback control system: design and implementation

The carbon content of the thin film can not be measured directly in real-time, and thus, estimates of the carbon content, which are obtained based on plasma composition in the reactor chamber by OES, are used in the feedback control system. Previous spectroscopic study of the reaction plasma [13] in this ECR PECVD system has shown that the carbon content in the film has a quasi-linear relationship with respect to the optical emission intensity ratio of C_2 molecules and O atoms in the reacting gas. This can be explained by the fact that carbon molecules are mostly responsible in forming the precursors for carbon incorporation into the film. This result suggests that the information of optical emission intensity ratio of C_2/O can be utilized to estimate the carbon content in the zirconium dioxide film in real-time.

In this work, a mathematical model is constructed to estimate the carbon content of the film based on the optical emission intensity ratio which is obtained through OES in real-time. Following the previous experimental results [13], the relationship between the carbon content in the surface layer and the optical emis-

sion intensity ratio can be written as follows:

$$X_C^s(t) = A\gamma(t) \tag{2.1}$$

where X_C^s is the atomic concentration (%) of carbon in the surface of the film, A is a constant which is related to the configuration and chamber condition of the specific experimental system (experimentally determined for our system to be 11.92) and γ is the optical emission intensity ratio of C_2/O.

The dominant factor that may lead to possible variation in the value of the parameter A is the chamber wall conditions. During the PECVD process, material deposition may occur on the substrate as well as on the reactor chamber wall. Although the deposition on the chamber wall is negligible compared to the deposition on the substrate for a single deposition experiment since the plasma is highly anisotropic, overtime the accumulated coatings on the wall will change the chamber wall potential and may be sputtered off the wall onto the substrate, thereby, leading to a reactor chamber condition corresponding to a different value of A. However, in practice, for each deposition run the change of A is negligible under the range of operating conditions of our interest. Moreover, chamber cleaning is regularly scheduled to avoid material accumulation on the chamber wall. Thus, A can be considered constant for a well-maintained system (nevertheless, to implement the control system on another reactor, experimental calibration of the parameter A may be necessary).

Under the assumption that the film growth rate remains constant, the carbon content of the whole film is obtained using the following formula:

$$X_C(t) = \frac{\int_{t_0}^{t} X_C^s(s)ds}{t - t_0} \tag{2.2}$$

where X_C is the atomic concentration (%) of carbon in the deposited film at time

t and t_0 is the time in which the deposition starts. In this case, we treat X_C as the time average of X_C^s. Combining Eqs.2.1 and 2.2, the following estimation model is obtained:

$$X_C(t) = A\frac{\int_{t_0}^{t} \gamma(s)ds}{t - t_0} \tag{2.3}$$

We note that although the deposition process is a batch process in nature, an optimal operating recipe can not be obtained since no accurate mathematical model describing the relationship between the optical emission intensity ratio and the inlet mass flow rate is currently available. Thus, the control problem for the process is formulated as a set-point regulation problem; this approach is further justified by our experimental results which clearly show that the response time of the closed-loop system is significantly smaller than the total deposition time.

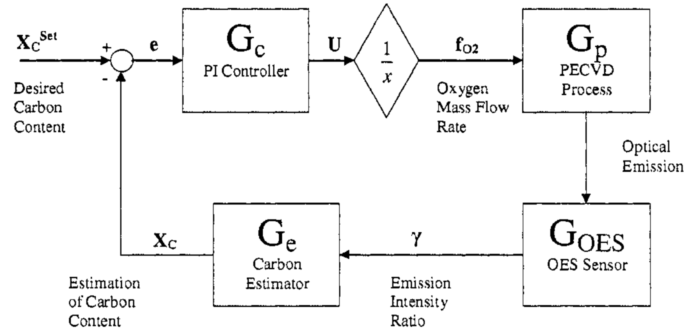

Figure 2.3: Block diagram of the closed-loop system under the proposed carbon content controller.

Fig.2.3 shows the structure of the closed-loop system under the proposed carbon content controller. The input to the controller is the difference between the desired carbon content and the estimated carbon content and the controller manipulates the inlet oxygen mass flow rate. The sensor block G_{OES} can be treated as a pure time delay since it takes a fixed amount of integration time for the OES system to obtain good signal-to-noise ratios and transfer the OES data through the

network. The G_e block is the carbon estimator described above. The G_c block is the controller based on the proportional-integral (PI) control algorithm (described below in detail). The G_p block is the process block describing the relationship between the change of oxygen mass flow rate and the optical emission intensity ratio γ of the plasma. G_p is identified experimentally and the identification procedure will be discussed in detail in subsection 5.1 below.

The oxygen mass flow rate is chosen as the manipulated variable because it provides the most effective way to influence the gas phase composition and it does not disturb the plasma stability compared to other candidate manipulated variables such as the microwave power, the eletromagnetic field strength, the substrate temperature and the chamber pressure. The argon mass flow rate is not selected as the manipulated variable because it significantly affects the film growth rate.

To eliminate unnecessary control actions, which may interfere with the plasma and lead to poor closed-loop performance, the control objective is to stabilize the carbon content value close to the desired set-point (i.e., within a certain tolerance ϵ). A PI control algorithm is used of the following form:

$$\frac{1}{f_{O_2}(t)} = U(t) = \frac{K_c\hat{e}(t) + K_i \int_{t_0}^{t} \hat{e}(\mu)d\mu + \bar{R}_f}{f_{Ar}(t)} \tag{2.4}$$

$$\hat{e}(t) = \begin{cases} e(t) & |e(t)| > \epsilon \\ 0 & |e(t)| \leq \epsilon \end{cases} \tag{2.5}$$

where U is the output of the controller, f_{O_2} is the oxygen mass flow rate, f_{Ar} is the Argon mass flow rate which scales with the precursor vapor flow rate, $\bar{R}_f$ is a steady state bias expressed in terms of the mass flow ratio of Ar/O_2 at steady state, e is the difference between estimated carbon content and the set-point value, K_c is

the proportional gain and K_i is the integral gain. The input of the controller $\hat{e}(t)$ is defined as in Eq.2.5 where ϵ is the tolerance within which we want to approach the desired set-point.

MATLAB simulations of the entire process model are performed to obtain reference values of the controller parameters to be used in the real-time computer control system. The reference values are initially computed by using the Ziegler-Nichols (ZN) tuning method (e.g., [19]) and then adjusted based on closed-loop simulation runs to achieve a desired output response.

The computer process control system was implemented on an Intel Pentium III 700 MHz PC with 512 MB RAM. All the programs used in this study were written in LabVIEW language and National Instruments LabVIEW for Windows Version 6.1 was used as runtime platform.

2.5 Experimental results and discussion

2.5.1 Open-loop system

The objective of the open-loop experiments is to study the dynamic behavior of the deposition process based on real-time OES measurements.

The first set of experiments (3 independent runs) were performed to study the relationship between the steady-state value of γ and the mass flow ratio of Ar/O_2, R_f. The experimental results are shown in Fig.2.4; each data point is obtained by setting R_f at a fixed value and measuring γ after 200 s to guarantee that the process has reached steady-state. The experimental results in Fig.2.4 suggest that the optical emission intensity ratio varies proportionally with respect to the cubic of the mass flow rate ratio; this relationship is shown by the dotted line and can

be mathematically expressed as follows:

$$\gamma_{ss} = K_p R_f^3 \tag{2.6}$$

where γ_{ss} is the steady-state value of the optical emission intensity ratio and K_p is a constant which depends on the processing chamber conditions and the carrier gas flow rate.

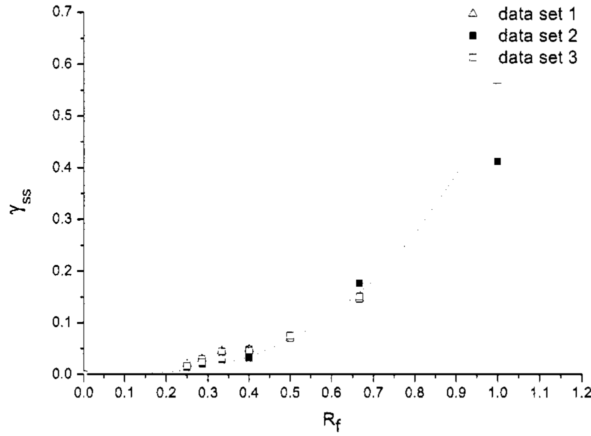

Figure 2.4: Experimental data of R_f vs. the γ_{ss} from different depositions for fixed argon flow rate 8 sccm, chamber pressure at 40 mTorr and microwave power 300 W.

In the second experiment, the process dynamics are identified by varying the mass flow ratio R_f in a way shown in the top curve in Fig.2.5 and measuring γ in real time using OES; the experimental results are presented in Fig.2.5. It can been seen that the process can be approximated by a first-order system which has a small time constant.

Using the experimental results shown in Figs.2.4 and 2.5, we constructed a *Simulink* model shown in Fig.2.6 within a MATLAB environment to obtain initial values of the controller parameters by simulation; $R_f(t)$ is the input and $\gamma(t)$ is the output. The model parameters were identified from the experiments to be

K_p=0.53 and τ_p=10 s.

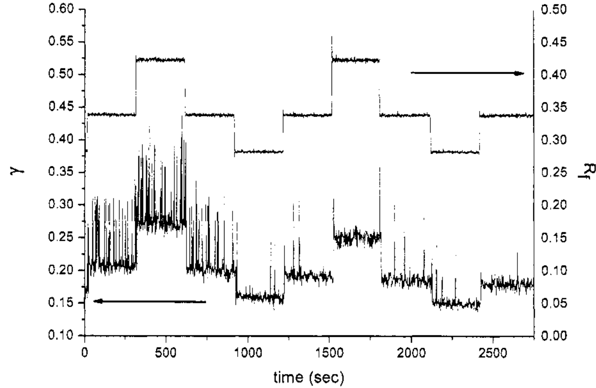

Figure 2.5: Response curve of γ of step changes in R_f for argon flow rate 8 sccm, chamber pressure 40 mTorr and microwave power 300 W.

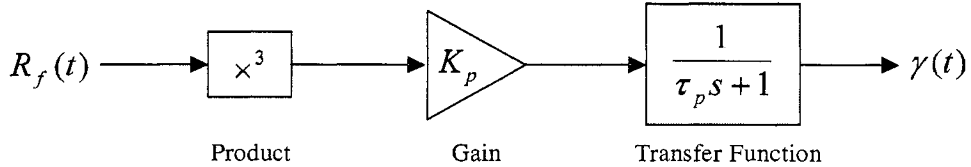

Figure 2.6: Simulink representation for the process dynamics.

Fig.2.7 shows the evolution of the carbon concentration of the surface (A) and of the bulk (B) of a ZrO_2 film during a typical open-loop deposition. The carbon concentrations are computed based on real-time OES measurements using the proposed estimation model. It can be observed that the starting stage of the deposition has relatively higher carbon incorporation. This corresponds to the OES measured high C_2 emission intensity and low O emission intensity during the initial stage of the deposition, as shown in Fig.2.8. Low O emission intensity indicates a low O concentration in the plasma, this may cause incomplete oxidation of the precursor, which leads to a high concentration of C_2 in the plasma during the initiation of the deposition process.

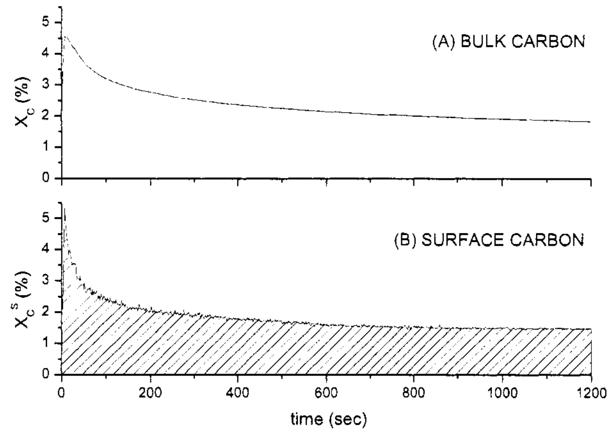

Figure 2.7: Evolutions of bulk (A) and surface (B) carbon concentration of a ZrO_2 film computed based on real-time OES measurements during an open-loop deposition with microwave power 300 W, chamber pressure 40 mTorr, Ar flow rate 8.4 sccm and O_2 flow rate 8 sccm.

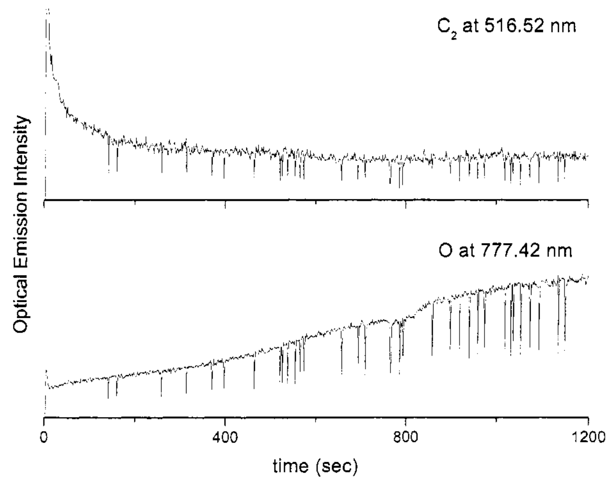

Figure 2.8: Evolutions of C_2 and O optical emission intensity during an open-loop deposition with microwave power 300 W, chamber pressure 40 mTorr, Ar flow rate 8.4 sccm and O_2 flow rate 8 sccm.

It can also be noticed in Fig.2.7 that the carbon concentration of the bulk of the film changes throughout the deposition process. This is not only because the bulk carbon concentration is an average value, but also because the carbon incorporation rate varies with time. This time variation may be explained by the continuous increase of O concentration in the plasma due to the complex and competing serial oxidation and dissociation processes [14]. As a result, reaction products with different compositions are generated and different amount of carbon is incorporated into the film at different times during the deposition process. Moreover, the magnitude of the carbon incorporation rate at the initial stage of the deposition is high and unpredictable (this may be due to the fact that the precursor feed rate which scales with the Ar flow rate is unpredictable as a result of the big pressure difference between the chamber and the bubbler at the beginning of the deposition), the variation would result in significant difference in the bulk carbon concentration, especially for an ultra thin film, since the total duration of the film deposition is quite short. Due to the existence of these uncertainties in the deposition process, the profile of bulk concentration of carbon shown in Fig.2.7 is not reproducible in our experiments; this suggests that it is very difficult to obtain a desired carbon concentration with open-loop operation.

2.5.2 Closed-loop system

Using the developed real-time feedback control system, carbon content-controlled deposition experiments were performed. Fig.2.9 shows a 20-minute long controlled-deposition which was carried out with microwave power fixed at 300 W, chamber pressure controlled at 40 mTorr and Ar flow rate set at 8 sccm. The carbon content controller was implemented with a set-point value for the atomic carbon

concentration of 1.4%, proportional gain K_c=1.0, integral gain K_i=0.05 and error tolerance ϵ=0.03%.

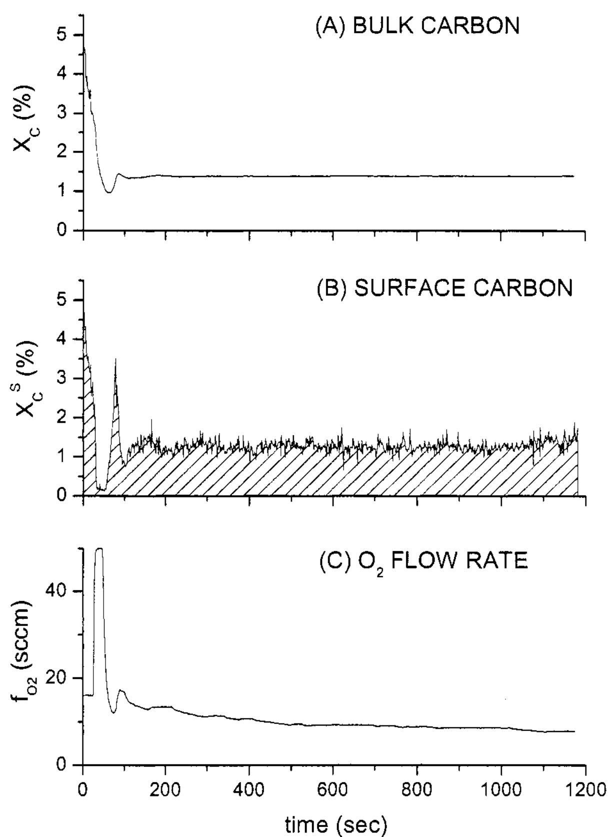

Figure 2.9: Evolution of bulk (A) and surface (B) carbon concentration of a ZrO_2 film computed based on real-time OES measurements and profile of manipulated oxygen flow rate (C) during a controlled deposition experiment with microwave power 300 W, chamber pressure 40 mTorr and Ar flow rate 8.4 sccm.

From the bulk carbon concentration curve in Fig.2.9, we can see that the carbon content of the film was controlled very closely to the desired value of 1.4% in spite of the initial plasma disturbance mentioned above (this result was also verified through off-line XPS analysis of the deposited film shown in Fig.2.16 below). The response time is relatively small compared to the deposition duration

which supports our set-point regulation formulation of this control problem.

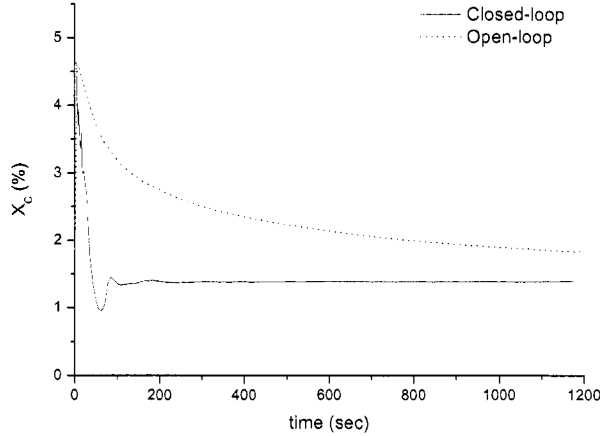

Figure 2.10: Closed-loop deposition vs. open-loop deposition with same initial deposition condition of microwave power 300W, chamber pressure 40 mTorr, Ar flow rate 8.4 sccm and O_2 flow rate 6 sccm.

A comparison of the bulk carbon concentration profile of the thin films under closed-loop (Fig.2.9) and open-loop (Fig.2.7) conditions with the same initial deposition conditions is shown in Fig.2.10. It can be clearly seen that the carbon content of the film was reduced by more than a factor of 5 under closed-loop control.

Moreover, to examine the robustness of the closed-loop system, we modify the set-point of the Ar mass flow controller so that the actual f_{Ar} is 5% higher than its nominal value. We observed in the XPS compositional analysis that the sample deposited under open-loop conditions slightly higher carbon due to the variation in f_{Ar}, while the sample deposited under closed-loop operation has a carbon content that is very close to the desired set-point value (within the error range of XPS compositional analysis, which is about $\pm$ 0.1 atomic percent). This result clearly demonstrates that closed-loop operation has better tolerance to

process disturbances than open-loop operation, and thus, with currently available equipment, closed-loop operation is expected to reduce thin film variability, which is the result of variation in the operating conditions.

Because the controller parameters are determined based on computer simulation using the identified values for the process parameters K_p and τ_p, we have also tested the sensitivity of the closed-loop system with respect to variations on the values of K_p and τ_p. Since the experimentally determined variations of K_p and τ_p in the range of operating conditions of interest are within the same order of magnitude, closed-loop simulations in which K_p and τ_p are varied by $\pm$ 50% have been performed. In these simulations, the set-point of the bulk carbon content is fixed at the original value (1.4%) and the controller parameters determined for the original process model ($K_p = 0.53$, $\tau_p = 10$), K_c=1.0 and K_i=0.05, have been used in all scenarios. Fig.2.11 and Fig.2.12 show the profiles of the controlled variable X_C and manipulated variable f_{O_2} for varying K_p and τ_p respectively. It can be seen that the stability of the closed-loop system is not affected by the variations in either K_p or τ_p and there are no significant deteriorations in the achievable closed-loop output response.

2.5.3 XPS analysis

The x-ray photoelectron spectra were obtained by a VG ESCALAB 5 electron spectrometer using an Al Kα x-ray radiation source (1486.6 eV). The take-off angle of 90° was used in all analysis. Survey scans ranging from 10-1200 eV were recorded using 1 eV step and 50 eV electron analyzer pass energy. High-resolution regional spectra of main elemental constituents are recorded using 0.1 eV step and 20 eV electron analyzer pass energy. The sampling depth is approximately

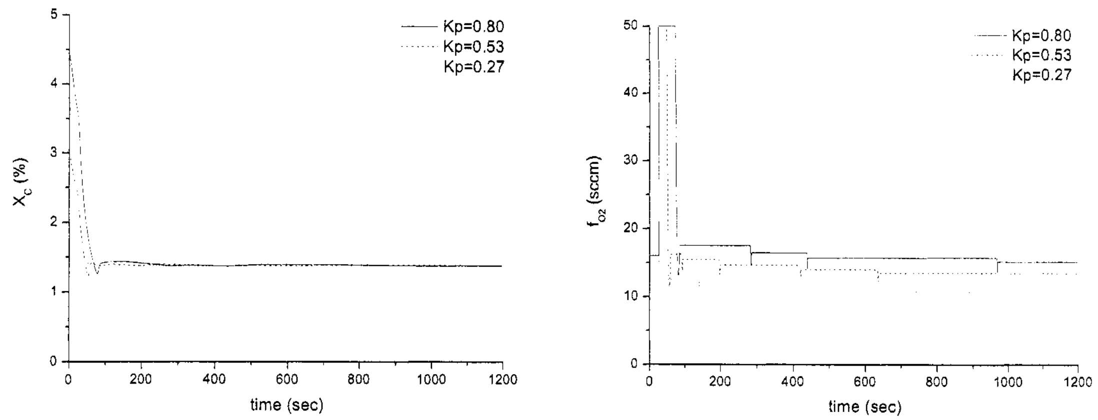

Figure 2.11: Simulated profiles of X_C (left) and f_{O_2} (right) of the closed-loop system with $K_p = 0.27$ (dotted line), $K_p = 0.53$ (dashed line) and $K_p = 0.80$ (solid line).

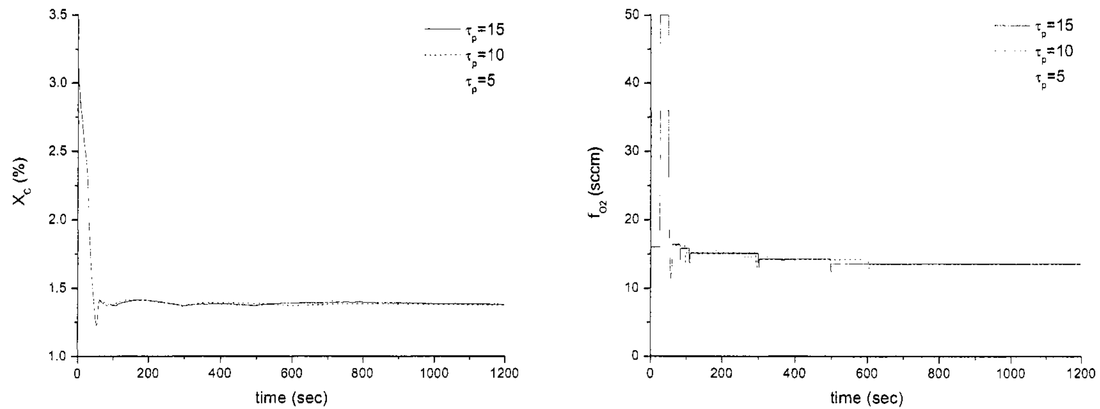

Figure 2.12: Simulated profiles of X_C (left) and f_{O_2} (right) of the closed-loop system with $\tau_p = 5$ (dotted line), $\tau_p = 10$ (dashed line) and $\tau_p = 15$ (solid line).

5-6 nm. The pressure in the analysis chamber is in the 10^{-10} Torr range. The measured binding energy data were referenced to the surface $C(1s)$ peak at 285 eV [49]. Atomic sensitivity factors used for the computation of the concentration of elements of interest are listed in Table 2.4.

Table 2.4: XPS atomic sensitivity factors (ASF).

Element	Peak	ASF
C	1s	0.25
O	1s	0.66
Zr	3d	2.1
Si	2p	0.27

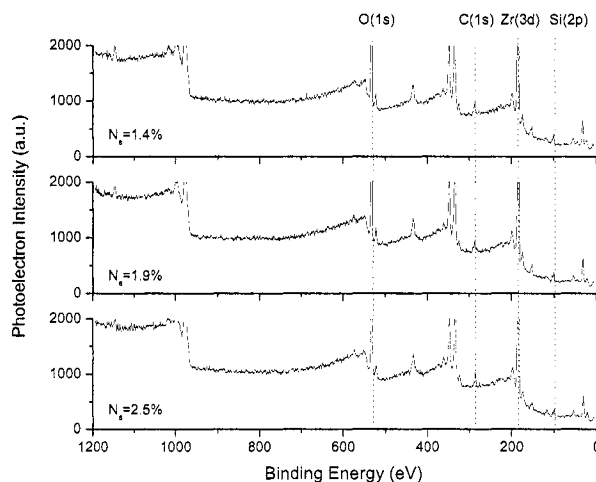

Figure 2.13: XPS survey spectra obtained from ZrO_2 thin films deposited by closed-loop deposition with set-point values of 1.4%, 1.9% and 2.5%.

Fig.2.13 shows the survey spectra obtained from ZrO_2 thin films deposited by closed-loop operation with set-point values of 1.4% (top), 1.9% (middle) and 2.5% (bottom). The thickness of all the deposited films was within the sampling depth of the XPS system since $Si(2p)$ substrate peaks were observable in all spectra.

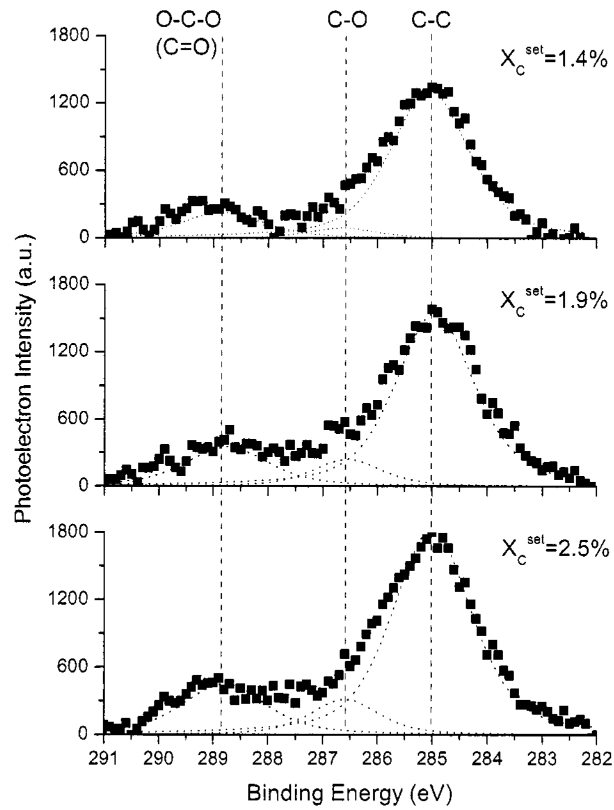

Figure 2.14: Carbon 1s peaks of the XPS spectra obtained from ZrO_2 thin films deposited by closed-loop deposition with set-point values for carbon content of 1.4%, 1.9% and 2.5%.

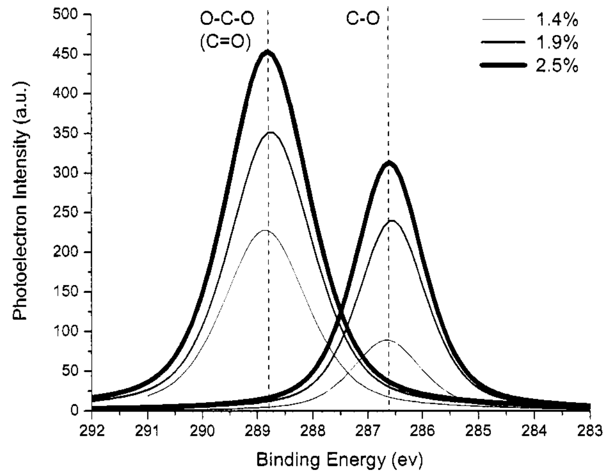

Figure 2.15: Comparison of deconvoluted carbon-oxygen peaks in C(1s) XPS spectra obtained from ZrO_2 thin films deposited by closed-loop operation with set-point values of 1.4%, 1.9% and 2.5%.

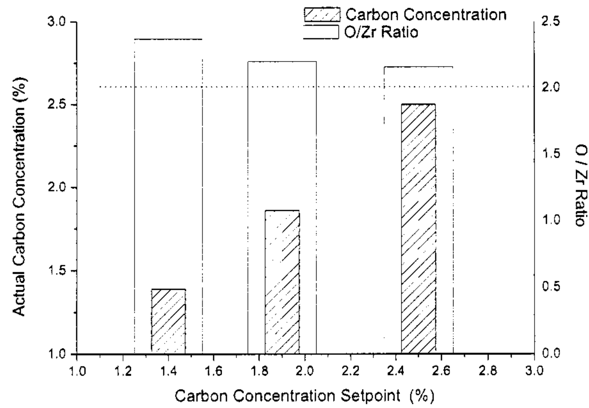

Figure 2.16: XPS compositional analysis results for closed-loop deposited ZrO_2 thin films.

Fig.2.14 shows the carbon $1s$ peaks of the XPS spectra obtained from ZrO_2 thin films deposited by closed-loop deposition with set-point values of 1.4%, 1.9% and 2.5%. The deconvoluted $C(1s)$ peaks at 285.0, 286.6 and 288.8 eV shown as dotted lines in Fig.2.14 are attributed to $C-C$, $C-O$ and $O-C-O$ (or $C=O$) bonds, respectively. From our previous work, we confirmed that most of the $C-C$ incorporation comes from the ambient contamination to the film surface during sample transfer from the PECVD system to the XPS system, and thus, the amount of $C-C$ bonds is not accounted for in the compositional analysis. The area of carbon-oxygen peaks in the XPS spectra are considered as a measure of the amount of carbon incorporation into the ZrO_2 films.

A comparison of the deconvoluted carbon-oxygen peaks from ZrO_2 films obtained by closed-loop depositions with different set-points is shown in Fig.2.15. It is evident that the lower the carbon content set-point in the controlled-deposition, the smaller the peak area for both carbon oxidation states, which is a good demonstration of the effectiveness of the real-time carbon content control system on the ZrO_2 thin film deposition.

The actual carbon concentration as well as the O/Zr ratio of ZrO_2 thin films from closed-loop deposition with different carbon content set-point values are computed from XPS spectra and presented in Fig.2.16. The $C-C$ peaks which were considered as ambient contamination were removed from the calculations. The O/Zr ratio was computed by subtracting the $O-C$ bonds to obtain the actual stoichiometric ratio of ZrO_2 in the film. The actual carbon concentration of the closed-loop deposited films matches quite well with the corresponding set-point values. The O/Zr ratios for all the films are greater than 2, which implies that fully stoichiometrically grown ZrO_2 films were deposited. The O/Zr ratios

are slightly higher than 2; this is due to the fact that a small portion of the measured $O(1s)$ intensity was due to $O - H$ bonds whose binding energies were indistinguishable from the $O - Zr$ bonds in the XPS analysis.

2.6 Conclusions

In this chapter, a method for real-time control of thin film composition in a PECVD process using combination of on-line OES and off-line XPS was presented. The method was used for real-time carbon content control of ZrO_2 thin films. An estimation model of carbon content of ZrO_2 thin films based on real-time optical emission spectroscopy data was initially developed. A feedback control scheme, which employs the proposed estimation model and a proportional-integral controller, was designed to achieve carbon content control. Based on this methodology, a real-time control system was developed and implemented on an experimental ECR PECVD system. Experimental results of depositions and XPS analysis of deposited thin films under both open-loop and closed-loop operations were shown and compared. The advantages of operating the process under real-time feedback control in terms of robust operation and lower carbon content were demonstrated.

Chapter 3

Dynamics and Control of Thin Film Surface Microstructure in a Complex Deposition Process

3.1 Introduction

While earlier research efforts focused on feedback control of thin film deposition processes with emphasis on deposition spatial uniformity control and on thin film composition control (see Chapter 2), there have been significant research efforts more recently, motivated by the growing industrial demands, focusing on modelling and control of thin film growth in order to obtain thin films with well-defined microstructure. While deposition uniformity control can be accomplished on the basis of continuum type distributed models, precise control of film properties requires models that predict how the film state (microscopic scale) is affected by changes in the controllable process parameters (macroscopic scale). This need has motivated extensive research on the development of fundamental mathematical models describing thin film growth.

Kinetic Monte-Carlo (kMC) simulation provides a framework for modeling the effect of macroscopic process variables on the thin film microstructure and has been widely used to simulate CVD processes (see [9] for a review of kMC simulation of CVD). However, the majority of these works have focused on studying the growth kinetics or interface structure while only a few works [70, 56] have addressed the computational efficiency which strongly affects the use of such kMC models within real-time feedback control systems. Recently, a methodology for feedback control of thin film growth using kMC models was developed in [40] and [41]. The methodology leads to the design of (a) real-time roughness estimators by using multiple small lattice kMC simulators, adaptive filters and measurement error compensators, and (b) feedback controllers based on the real-time roughness estimates. The method was successfully applied to control surface roughness in a $GaAs$ deposition process using an experimentally determined kMC process model [43]. Other approaches have also been developed to: (a) identify linear deterministic models from outputs of kinetic Monte-Carlo simulators and perform controller design by using linear control theory [63, 4], (b) construct reduced-order approximations of the master equation [27], and (c) construct stochastic partial differential equation models using kMC simulations [50, 51].

However, among these computationally attractive models, most of them consider only single component systems, and long-range interactions have not been modelled explicitly. In reality, most CVD processes are heterogeneous deposition processes where more than one species participate in the film growth. Moreover, direct long-range interactions [21] and substrate-mediated long-range interactions [48] are very important in many of these processes. For example, in the PECVD ZrO_2 process, there is a large number of different species present in the gas phase

during the deposition, and many of them participate in the thin film growth, particularly, zirconium hydroxide and hydrocarbon species (see [14] for detailed experimental results). Moreover, recent experimental results [12] have shown that, when zirconium hydroxides are the dominant species in the gas phase, the deposited ZrO_2 thin film has a very smooth surface with a roughness value less than half ZrO_2 monolayer, which suggests that the zirconium hydroxide species tend to uniformly cover the substrate surface. On the other hand, when hydrocarbons dominate the gas phase, the deposited ZrO_2 thin film has a very rough surface characterized by big islands, which suggests that the aggregation of the hydrocarbon species on the substrate surface, as a result of long-range interactions, is quite significant. It is quite obvious that a single component kMC model considering only short-range interactions is inadequate to describe the thin film growth in this process. Therefore, a computationally efficient kMC model of heterogeneous deposition processes in which long-range interactions are accounted for is needed.

In this chapter, a complex deposition process, which includes two types of macromolecules whose growth behaviors are very different, is investigated. This deposition process is influenced by both short-range and long-range interactions. The study of this process is motivated by recent experimental results on the growth of high-κ dielectric thin films using PECVD. A multi-component kMC model is developed for the deposition. Both single-component and multi-component cases are simulated and the dependence of the surface microstructure of the thin film, such as island size and surface roughness, on substrate temperature and gas phase composition are studied. The surface morphology is found to be strongly influenced by these two factors and growth regimes governed by short-range and long-range

interactions are observed. Furthermore, two kMC model-based feedback control schemes which use the substrate temperature to control the final surface roughness of the thin film are proposed. The closed-loop simulation results demonstrate that robust deposition with controlled thin film surface roughness can be achieved under a kMC estimator-based proportional integral (PI) feedback controller in the short-range interaction dominated growth regime, while a kMC model-predictive controller is needed to control the surface roughness in the long-range interaction dominated growth regime.

3.2 Surface microstructure model for thin film growth

Deposition processes such as PECVD, often involve large numbers of participating species with heterogeneous growth behaviors. Here, we study a heterogeneous deposition process in which two types of macromolecules of very different growth behavior, type A and type B, are present. Type A macromolecule is significantly affected by long-range attractions and tends to aggregate with other A macromolecules into clusters, i.e., it favors Volmer-Weber (VW) growth mode [30]. Hydrocarbon molecules generated from the decomposition of metal-organic (MO) precursors in a PECVD process are good examples of such type. Type B macromolecule favors surface sites of local minimum height, which usually results in Frank-van der Merwe (FM) type of film growth [30]. Metal oxides or hydroxides originated from the MO precursors may behave similar to macromolecules of type B as discussed in the introduction.

The geometry of the deposition process is shown in Fig.3.1. The gas flux is perpendicular to the substrate surface. Flux compositions, i.e., flux of A and B, in terms of the number of macromolecules encountered per unit time per surface

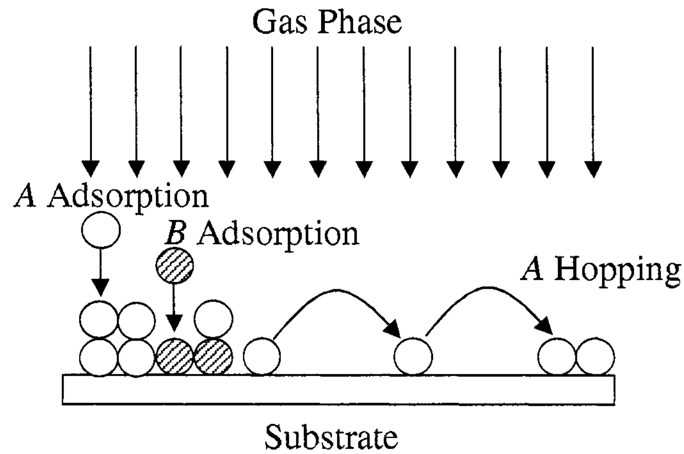

Figure 3.1: Thin film growth process.

site, are taken as macroscopic process parameters. They can be measured directly (via mass spectrometer for example) or determined based on the measurements of the partial pressures for each species and gas phase temperature using kinetic theory [36]. Thus, we model only the micro-processes taking place on the substrate surface. Both A and B can diffuse from the gas phase onto the substrate, however, B type macromolecules settle to surface sites of local minimum height (surface relaxation) simultaneously during adsorption. Surface migration and desorption processes are ignored (generally true for low temperature CVD processes such as PECVD), while hopping of A type macromolecules is allowed (as if A is firstly physisorbed). Surface reactions are not explicitly considered in this process, however, the long-range behavior of A and the surface relaxation of B could be consequences of surface reactions (i.e., surface mediated).

3.2.1 Micro-process model

The growth micro-process model is constructed based on a standard kMC scheme [29] which assumes the growth process to be a Poisson process. Therefore, the dynamics of the deposition process are governed by the master equation which describes the evolution of probabilities of the surface being in specific micro-configurations. Monte-Carlo simulation is used to obtain realizations of this stochastic process which are consistent with the master equation.

To simulate the heterogeneous deposition process studied in this chapter, a simple cubic lattice structure, which is a good approximation for amorphous films, is used. The simulated surface domain is a square grid of 100 lattice points by 100 lattice points. To improve computational efficiency, the solid-on-solid assumption is made (i.e., voids and overhangs can be neglected), and the adsorption of vapor phase macromolecules are always lined up with surface sites. We consider a multilayer growth and assume that all the sites are available for adsorption of all gas phase species at all times, and, thus, the adsorption rates of A (w_a^A) and B (w_a^B) are taken to be site independent; they can be obtained in real-time as discussed above.

To incorporate different growth behaviors into a kMC scheme, a viable way is to set up specific rules for the micro-processes considered in the scheme (see [61] for an example of rule-based modelling of coating microstructure). Although, such rules may be arbitrary and may sacrifice the fidelity of the model with respect to the detailed physics and chemistry, they are very favorable from a computational point of view, and thus, preferable for real-time applications. Furthermore, when mechanisms of such behaviors are unknown, which is true for most of the complex PECVD processes, rule-based modelling must be used. In this work, we set up

two rules for aggregation of A type macromolecule and surface relaxation of B type macromolecule, respectively.

For A type macromolecules, we enforce a rule on the hopping process. To encourage the aggregation of the surface A macromolecules over long-range, we select the hopping direction of an A type macromolecule based on the number of the surface As that the hopping A can see in each direction instead of randomly picking among the possible hopping directions. Specifically, the hopping direction of a specific A macromolecule is determined by comparing the distance-weighted sum of all the A macromolecules in each direction and pick the one with largest value of the sum. The weighted sum, for example, in the positive x direction of an A located at the surface lattice point (x_0, y_0), $N^A_{h,+x}(x_0, y_0)$, is computed as follows:

$$N^A_{h,+x}(x_0, y_0) = \sum_{x=1}^{l_a} \sum_{y=-x}^{x} S^A_{(x_0+x, y_0+y)}(1 - \frac{\sqrt{x^2+y^2}}{l_a}) \tag{3.1}$$

where l_a is the maximum range of attraction, and the value of the occupancy factor $S^A_{(i,j)}$ is unity when the surface site (i, j) is occupied by an A and zero otherwise. Eq.3.1 imitates the sight of a surface A which fades out with distance, i.e., the near neighbors are weighted more than the distant neighbors. $1 - \dfrac{\sqrt{x^2+y^2}}{l_a}$ is picked as the weighting function to employ a linearly decaying weighting which goes to zero at the boundary of the attraction zone, however, one can use any meaningful weighting function here to carry out simulations to simulate or validate specific deposition mechanisms.

The rate of the surface hopping of an A type macromolecule depends on the local activation energy barrier. Considering only the interactions of the first nearest side neighbors and the first nearest bottom neighbor to determine the hopping rate at a specific site, the hopping rate of a macromolecule of type A on the surface

with n first nearest side neighbors is given by

$$w_h^A(n) = k_{h0}^A \exp(-\frac{E_s^A + nE_n^A}{kT}) \tag{3.2}$$

where k_{h0}^A is the hopping frequency constant, E_s^A and E_n^A are the energy barriers associated with surface hopping of A for bottom and side neighbors respectively (we note that for simplicity we do not distinguish the neighboring macromolecules of different types).

For B type macromolecules, we enforce a surface relaxation rule on the adsorption process. During an adsorption event, a site, (i, j), is first randomly picked among the sites of the whole lattice; the final site in which the B macromolecule adsorbs onto could be different from the initially chosen site for the adsorption event. In particular, when the initially chosen site does not have the local minimum height, B will be adsorbed onto one of the neighboring sites that has the local minimum height. In this work, only the 4 first nearest neighbor sites and 4 second nearest neighbor sites are considered. In addition, the sticking probability of type B macromolecule on surface site occupied by type A macromolecules is considered very small (5% in this study). This is because when this sticking probability is close to unity, the surface would be smoothed by type B macromolecules independently of the presence of type A macromolecules, and thus, the dynamics of the two-component deposition would not be observable. All other sticking probabilities are considered to be unity for simplicity.

The life time of each Monte-Carlo event in the simulation τ can be determined by the following expression (see [29] for a detailed proof):

$$\tau = -\frac{\ln \xi}{w_a^A + w_a^B + \sum_{n=0}^{4} N_n^A w_h^A(n)} \tag{3.3}$$

where ξ is a random number that follows the uniform distribution in the unit

interval and N_n^A is the number of A type macromolecules on the surface with n first nearest side neighbors.

Remark 3.1 *Since we treat hopping events towards different hopping directions as different microscopic events, the KMC simulation does not need to determine which hopping direction the macromolecule needs to go once the event is selected, and therefore, overriding the direction chosen by KMC by the micro-process rule is not an issue here, and the time increment can be calculated using Eq.5.3. Hopping processes towards different hopping directions are treated as independent Poisson processes just like the adsorption of A and the adsorption of B. As long as the dynamical hierarchy of transition rates is preserved in the kinetic Monte-Carlo simulation, the time increment should be selected from the exponential distribution of Eq.5.3.*

3.2.2 Simulation procedure

Table 3.1: Model parameters.

A ads. sticking prob. on A	s_A^A	100	%
A ads. sticking prob. on B	s_B^A	100	%
A hopping freq. const.	k_{h0}^A	10^{13}	s^{-1}
A hopping energy (bottom)	E_s^A	1.6	eV
A hopping energy (side)	E_n^A	0.4	eV
A attraction range	l_a	20	units
B ads. sticking prob. on A	s_A^B	5	%
B ads. sticking prob. on B	s_B^B	100	%

The parameters, k_{h0}^A, E_s^A, E_n^A and l_a in the model can be determined by optimal parameter estimation using experimental data, however, the parameters used in this study are arbitrarily chosen and are shown in Table 3.1. When the lattice is set and the rates of the three events (A adsorption, B adsorption, A hopping) are determined based on measurements or its corresponding rate expression (Eq.3.2),

a kinetic Monte-Carlo simulation is executed following the algorithm reported in [70]. First, the surface A macromolecules are grouped into five classes based on the number of side neighbors (from 0 to 4 side neighbors); in each class, the macromolecules have the same hopping rates, however, they may have different hopping directions depending on the surface micro-configuration; the adsorption rates of the A and B macromolecules are both site independent. Then, a random number is generated to select an event to be run based on the rates; if the event is A hopping, the class in which the event will happen is also selected. After that, a second random number is generated to select the site where the event will be executed; if the event is A or B adsorption, the site is randomly picked from sites in the entire lattice; if the event is A hopping, the site is randomly picked from the list of the sites in the selected class. After the site is selected, the MC event is executed. If the event is adsorption, it is executed by adding one macromolecule on the selected site (B adsorption rule is applied if the event is B adsorption); if the event is A hopping, the A type macromolecule on the site is moved to the next site in the direction selected by the hopping rule. Upon an executed event, a time increment τ computed based on Eq.5.3 is added to the process time t. Periodic boundary conditions are used in the simulation to satisfy the mass balance of the hopping macromolecules.

Referring to the kinetic Monte-Carlo (kMC) simulation of the surface evolution using the microscopic process rules defined in the manuscript, it is important to note that we treat the surface evolution as a sequence of Poisson processes. Under this assumption, the evolution of the probability that the process (surface) is at a certain microscopic configuration σ at time t is determined by the so-called master

equation:

$$\frac{\partial P(\sigma,t)}{\partial t} = \sum_{\sigma'} W(\sigma' \to \sigma)P(\sigma',t') - \sum_{\sigma'} W(\sigma \to \sigma')P(\sigma,t) \tag{3.4}$$

where σ and σ' are successive states of the system, $P(\sigma,t)$ is the probability that the system is in state σ at time t, and $W(\sigma' \to \sigma)$ is the probability per unit time that the system will undergo a transition from state σ' to σ. When the process reaches equilibrium (i.e., $\frac{\partial P(\sigma,t)}{\partial t} = 0$), this equation reduces to the so-called detailed-balance criterion:

$$\sum_{\sigma'} W(\sigma' \to \sigma)P(\sigma',t') = \sum_{\sigma'} W(\sigma \to \sigma')P(\sigma,t) \tag{3.5}$$

From Eqs.3.4 and 3.5, it follows that during the dynamical evolution of the process (i.e., $\frac{\partial P(\sigma,t)}{\partial t} \neq 0$), the detailed balance should not be satisfied. Moreover, the strict detailed-balance criterion ($W(\sigma' \to \sigma)P(\sigma', eq) = W(\sigma \to \sigma')P(\sigma, eq)$) does not even need to be satisfied at process equilibrium.

However, to correctly simulate the dynamical phenomena of a Poisson process, regardless of the existence of a process equilibrium, one needs to guarantee that the transition probabilities reflect unique transition rates. These probabilities should be formulated so that a dynamical hierarchy of transition rates is established in terms of appropriate models for the rates of the microscopic events considered in the entire process. To achieve such dynamical hierarchy for our process (which does not reach equilibrium), we choose the transition probability to be the rate of a specific event (e.g., the rate of a hopping event in a specific direction), divided by the sum of all the rates of the microscopic events. As we describe in the manuscript, we first choose a microscopic event among all possible adsorption events (A and B) and hopping events (A only, including hopping to all directions) based on the transition probabilities of adsorption and hopping; then, in the

case of a hopping event, we choose a class of hopping events among all classes (each class includes hopping events towards different directions); once the class of the hopping event is selected, a hopping event of a specific macromolecule is randomly picked, since there are macromolecules with different hopping directions in each hopping class, the probability of picking a macromolecule hopping to the $+x$ direction should be $N^A_{n,+x}/N^A_n$ (where $N^A_{n,+x}$ is the number of surface macromolecules which have n nearest neighbors and hop towards the $+x$ direction once they are selected to hop). Therefore, the transition probability of a hopping event of an n nearest-neighbor surface macromolecule towards the $+x$ direction to occur can be computed as follows:

$$
\begin{aligned}
W_{h,+x}(n) &= \frac{N^A_n w^A_h(n)}{w^A_a + w^B_a + \sum_{n=0}^{4} N^A_n w^A_h(n)} \times \frac{N^A_{n,+x}}{N^A_n} \\
&= \frac{N^A_{n,+x} w^A_h(n)}{w^A_a + w^B_a + \sum_{n=0}^{4} (N^A_{n,+x} + N^A_{n,-x} + N^A_{n,+y} + N^A_{n,-y}) w^A_h(n)}
\end{aligned}
\tag{3.6}
$$

where $N^A_{n,-x}$, $N^A_{n,+y}$ and $N^A_{n,+y}$ are the number of surface macromolecules which have n nearest neighbors and hop towards the $-x$, $+y$ and $-y$ directions once they are selected to hop, respectively. We can see that the transition probability $W_{h,+x}$ is picked as the ratio of the rate of the $+x$ hopping event $N^A_{n,+x}w^A_h(n)$ over the sum of the rates of all microscopic events, and therefore, the transition probability is uniquely specified by the rate of the hopping event.

Moreover, if we were to study a process that would reach equilibrium, then the microscopic process rules should have been defined in a way such that the process is able to reach equilibrium, and accordingly, the detailed balance of the transition probabilities should have been satisfied at equilibrium. When the transition probabilities are formulated in the same way as we described above for a set of

microscopic rules that constitute a process which goes to equilibrium, a dynamical hierarchy is achieved and the detailed balance criterion will be satisfied when the process reaches equilibrium.

3.3 Simulation results and discussion

Using the proposed growth model, a parametric analysis of the growth process is conducted. We study the effects of substrate temperature (in the range of 600 K to 880 K, which is the normal operating temperature of low temperature CVD processes such as PECVD) and gas phase composition on the surface microstructure of the deposited thin films in both homogeneous and heterogeneous deposition processes. Furthermore, the effect of simulation lattice size has also been investigated. This study provides valuable insight for the formulation of the control problem.

Island sizes of the thin films obtained under different process conditions are qualitatively compared and the surface roughness of each film, r, is computed in a root-mean-square fashion by the following expression:

$$r = \sqrt{\frac{\sum_{i=0}^{N}\sum_{j=0}^{N}(h_{ij} - \bar{h})^2}{N \times N}} \tag{3.7}$$

where N is the size of the lattice, $\bar{h}$ is the average height of the film and h_{ij} is the height of the surface at position (i, j).

3.3.1 Single-component case

The simulation of a single component deposition process can be executed by setting either parameter w_a^A or w_a^B in the heterogeneous model equal to 0.

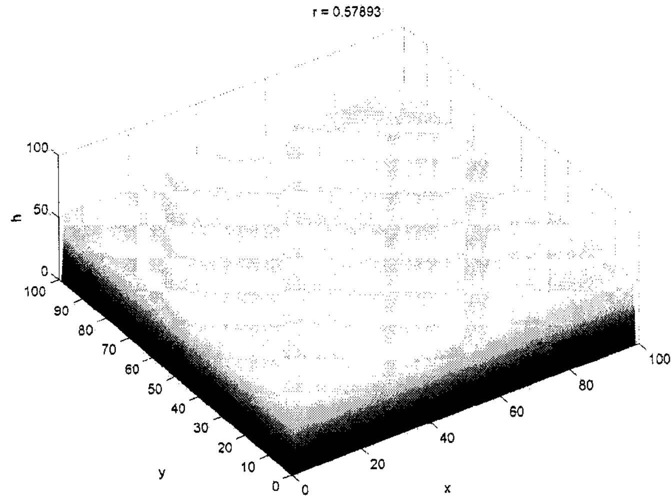

Figure 3.2: Surface of a thin film deposited with $w_a^A = 0s^{-1}$, $w_a^B = 0.1s^{-1}$ and $T = 800$ K - $t = 550s$.

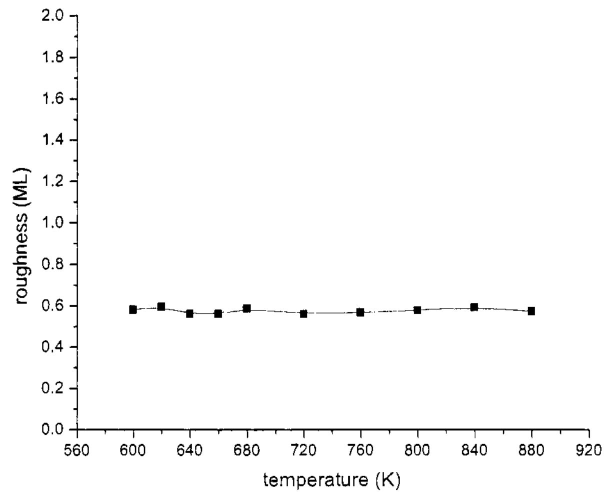

Figure 3.3: Surface roughness of thin films deposited with $w_a^A = 0s^{-1}$, $w_a^B = 0.1s^{-1}$ for different substrate temperature - $t = 550s$.

Fig.3.2 shows the surface morphology of a thin film obtained by a deposition with only B type macromolecules present in the gas phase. It can be seen that the surface of the thin film is very smooth due to the surface relaxation of B, and the film growth is in FM mode (see Fig.3.7 (solid line) for the profile of the surface roughness during the deposition). Since the adsorption rate is independent of the substrate temperature, the surface microstructure of the thin film has no dependence on substrate temperature (Fig.3.3).

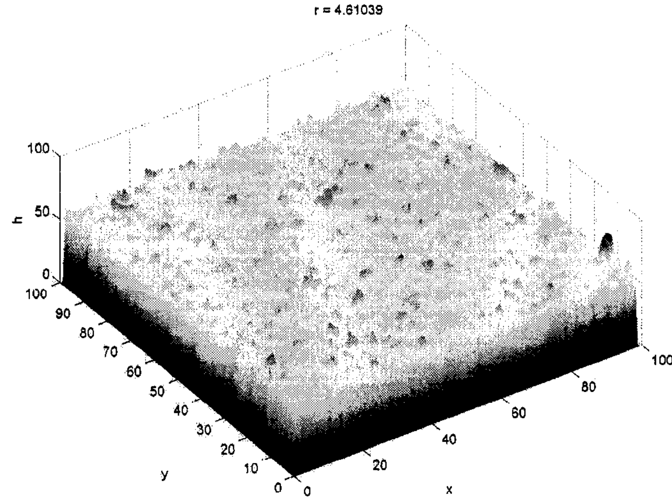

Figure 3.4: Surface of a thin film deposited with $w_a^A = 0.1s^{-1}$, $w_a^B = 0s^{-1}$ and $T = 640$ K - $t = 570s$.

Figs.3.4 and 3.5 show the surface morphologies of thin films obtained by depositions with only A type macromolecules present in the gas phase at low and high substrate temperatures, respectively. The thin film deposited at low substrate temperature (T = 640 K) has a high island density but a small lateral island size. The thin film deposited at high substrate temperature (T = 760 K) has a low island density but a large lateral island size.

The very different surface microstructure observed for these two films, which have similar roughness values, can be explained by the different growth modes in

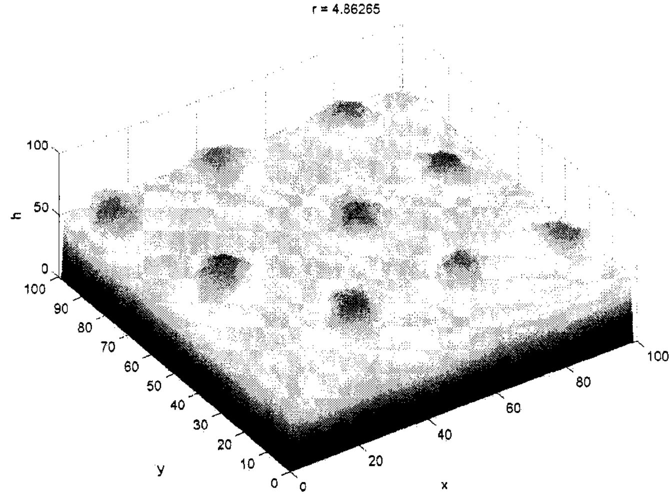

Figure 3.5: Surface of a thin film deposited with $w_a^A = 0.1s^{-1}$, $w_a^B = 0s^{-1}$ and $T = 760$ K - $t = 570s$.

these two temperature regimes. According to the hopping rate equation (Eq.3.2), surface hopping of A type macromolecules has an Arrhenius type dependence on substrate temperature T. Thus, at low substrate temperature, the hopping rate is much smaller than the rate at high substrate temperature. This suggests that at low temperature, the dominant surface micro-process is the adsorption process, therefore, although the long-range attraction tends to drive the surface A type macromolecules together, the hopping rate is so low that these macromolecules are not able to move along the direction of attraction far enough to form large islands. Therefore, the effect of long-range attraction is not significant and the aggregation mostly occurs in the vertical direction (one dimensional aggregation) by A adsorption. This growth mechanism results in a surface with islands of large height and small lateral size.

On the other hand, when the substrate temperature is high, the rate of hopping becomes large, surface A type macromolecules are able to move along the direction of attraction for a distance comparable to the range of attraction. Therefore, the

effect of long-range attraction becomes very significant and aggregation occurs in both vertical and horizontal direction (three dimensional aggregation, i.e., VW growth mode) by adsorption and hopping. This growth mechanism leads to the formation of islands with large dimensions in both the vertical and the horizontal directions. Furthermore, we note that although the range of attraction is limited to l_a, the lateral size of the islands are not limited by the range of interaction due to the coalescence between islands. Islands of lateral size larger than l_a are observed in our simulations for high substrate temperature depositions.

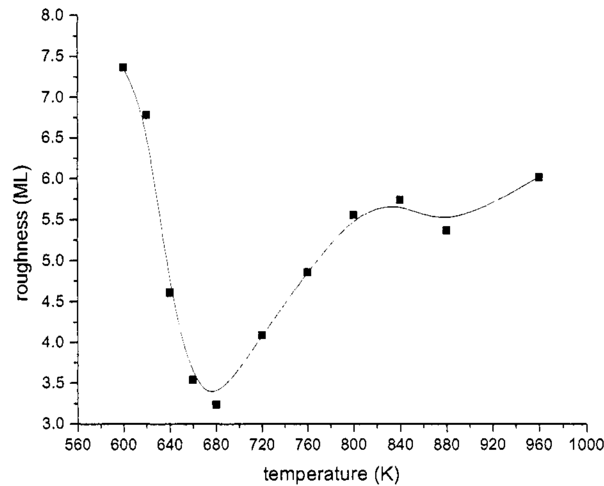

Figure 3.6: Surface roughness of thin films deposited with $w_a^A = 0.1s^{-1}$, $w_a^B = 0s^{-1}$ for different substrate temperature - $t = 570s$.

Fig.3.6 shows the surface roughness of thin films deposited at different substrate temperatures. It can be clearly seen that there are two temperature regimes in which thin film growth is quite different. In the low temperature regime, the surface roughness drops with increasing temperature, in the high temperature regime, the surface roughness rises with increasing temperature (however, the surface roughness drops again when the substrate temperature is very high when

stable surface islands start to coalesce and form islands with lateral dimension larger than the range of attraction). Based on the discussion above about the different growth modes at low and high substrate temperatures, the transition from the low temperature regime to the high temperature regime corresponds to the change in growth process from short-range interaction dominant to long-range attraction dominant. The substrate temperature at which the minimum roughness is achieved corresponds to the separation of the two temperature regimes.

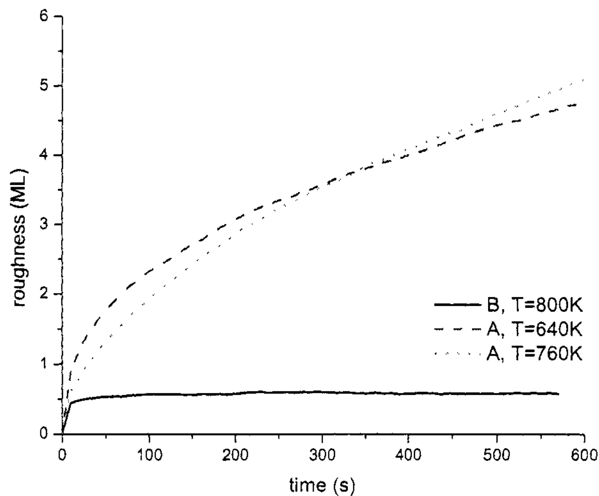

Figure 3.7: Surface roughness of thin films during depositions with a. $w_a^A = 0s^{-1}$, $w_a^B = 0.1s^{-1}$ and $T = 800\ K$ (solid line); b. $w_a^A = 0.1s^{-1}$, $w_a^B = 0s^{-1}$ and $T = 640\ K$ (dashed line); c. $w_a^A = 0.1s^{-1}$, $w_a^B = 0s^{-1}$ and $T = 760\ K$ (dotted line).

Fig.3.7 shows the profiles of the thin film surface roughness during the deposition. It can be clearly seen that the thin film growth in the B only deposition is 2D growth (the surface roughness saturates over time) while the growth in the A only deposition, with either low or high substrate temperature, is 3D growth (the surface roughness never saturates).

3.3.2 Multi-component case

We have also simulated multi-component deposition which is heterogeneous, using the proposed process model. Both A and B types of macromolecules are present in the gas phase and the relative ratio of the two species is set to be unity in the simulated case for simplicity.

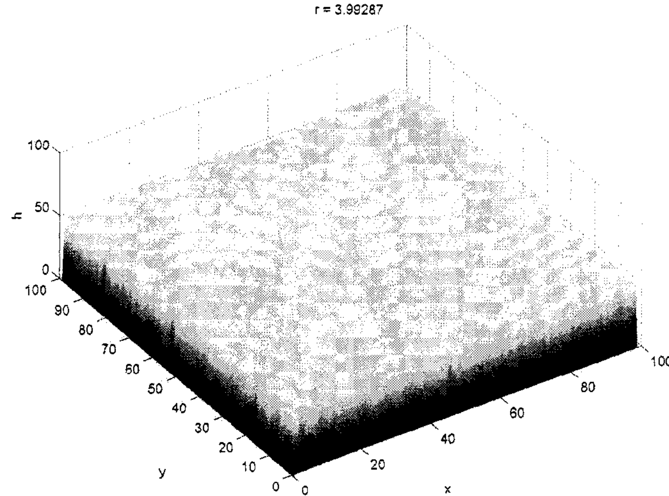

Figure 3.8: Surface of a thin film deposited with $w_a^A = 0.05s^{-1}$, $w_a^B = 0.05s^{-1}$ and $T = 640\ K$ - $t = 900s$.

Figs.3.8 and 3.9 show the surface morphology of thin films obtained by depositions at low (T = 640 K) and high (T = 880 K) substrate temperatures, respectively. The difference in surface morphology between the two thin films is similar to the single component case in which only A type of macromolecules are present in the gas phase. This is expected since the behavior of the two types of macromolecules is considered independent of each other in the simulation.

Fig.3.10 shows the surface roughness of thin films deposited at different substrate temperatures. Two temperature regimes can also be observed in the multi-component case, however, the absolute surface roughness values of the high sub-

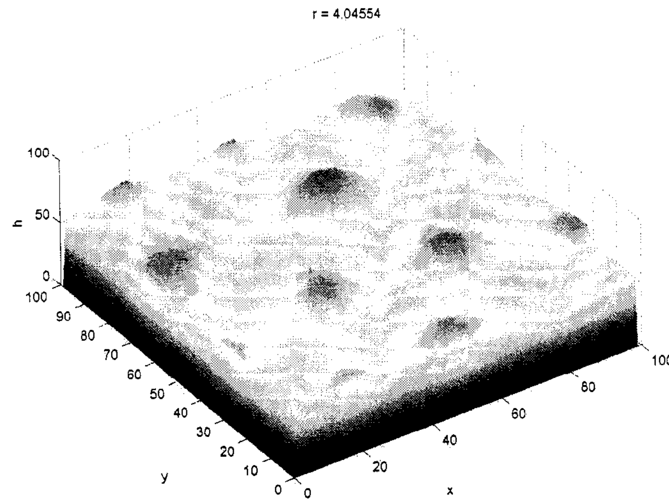

Figure 3.9: Surface of a thin film deposited with $w_a^A = 0.05s^{-1}$, $w_a^B = 0.05s^{-1}$ and $T = 880\ K$ - $t = 900s$.

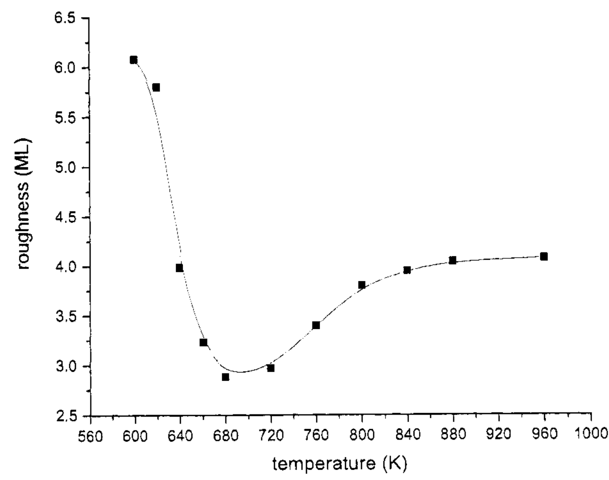

Figure 3.10: Surface roughness of thin films deposited with $w_a^A = 0.05s^{-1}$, $w_a^B = 0.05s^{-1}$ for different substrate temperature - $t = 900s$.

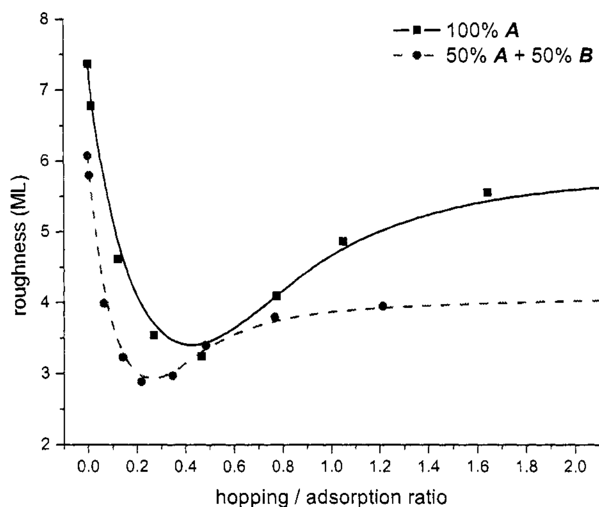

Figure 3.11: Surface roughness of the thin films deposited for different hopping to adsorption ratio in a. homogeneous deposition, 100%A (solid line); b. heterogeneous deposition, 50%A + 50%B (dashed line).

strate temperature regime are relatively small. To effectively compare the temperature dependence of surface roughness between homogeneous and heterogeneous processes, roughness values are plotted in Fig.3.11 versus hopping to adsorption ratio (the ratio of the total number of hopping events to the total number of adsorption events in the overall simulation time), since the adsorption and the hopping events directly shape the surface of the thin films. In addition, this ratio of hopping to adsorption monotonically increases with increasing substrate temperature. It can be seen in Fig.3.11 that a lower roughness value is observed for the heterogenous deposition compared to the homogeneous deposition. Furthermore, we note that the presence of B type macromolecules does affect the transition of the growth process from the short-range interaction dominant regime (low substrate temperature) to the long-range interaction dominant regime since the value of hopping to adsorption ratio that separates the two regimes of the multi-

component case is smaller than that of the single-component case. This may be due to the fact that the presence of B type macromolecules in the gas phase facilitates the smoothening of the film surface by adsorbing onto surface sites with local minimum heights. However, in both cases the dependence of surface roughness on substrate temperature is almost the same; this observation suggests that the temperature dependence of the heterogeneous deposition is qualitatively determined by A type macromolecules.

3.3.3 Effect of gas phase composition

Since different gas phase compositions can be used to tailor the material properties of the thin films obtained by the depositions for different applications, simulations of depositions for different gas phase compositions have been run to study the effect of gas phase composition on the surface microstructure based on the proposed growth model. We note that since the adsorption of type B macromolecule is surface site-dependent, the growth rate of the thin film varies with gas phase composition. Therefore, comparison has been conducted between thin films with the same thickness.

Fig.3.12 shows the surface roughness of thin films deposited for different gas phase compositions. It can be seen that the increase of relative concentration of A leads to increasing surface roughness and vice versa. Moreover, when the relative concentration of A is larger than 50%, the presence of two temperature regimes is quite clear. This again suggests that type A macromolecules have significant effect on the surface microstructure when the relative concentrations of A and B are comparable.

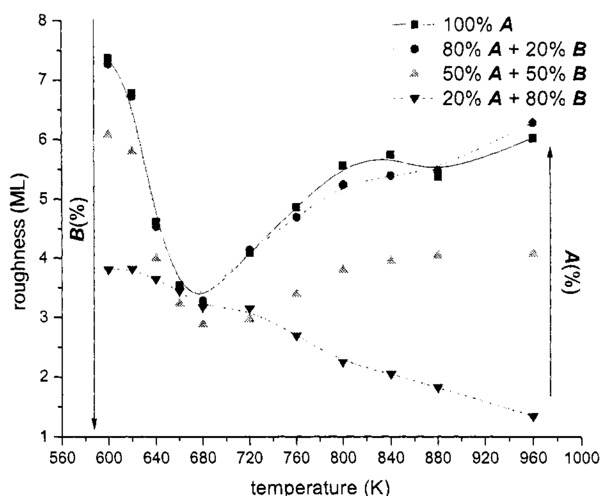

Figure 3.12: Surface roughness of thin films deposited with different gas phase compositions: a. $100\%A$ (solid line); b. $80\%A + 20\%B$ (dashed line); c. $50\%A + 50\%B$ (dotted line); d. $20\%A + 80\%B$ (dashed dotted line).

3.3.4 Effect of lattice size

Because the dimension of the wafers used in a real deposition process is usually in the 10^8 nm regime, it is impossible to simulate the film growth for the entire wafer even with the most efficient Monte-Carlo algorithm and the best available computing power, and thus, a lattice size which corresponds to a very small spatial domain compared to the actual wafer dimension is used in this work. However, to better gauge the results from such simulations, investigating the lattice size dependency of the simulation results is necessary.

Fig.3.13 shows the surface roughness of thin films deposited with different substrate temperature computed using different simulation lattice size. It can be seen that simulation results from kMC runs with lattice size larger than 50×50 agree very well with each other, while simulation results from the 50×50 lattice

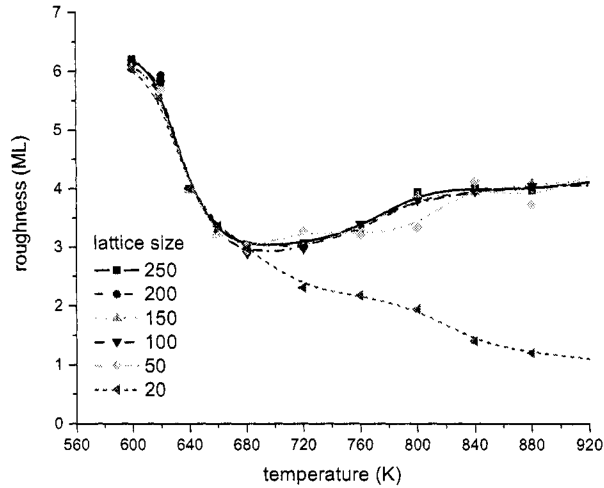

Figure 3.13: Surface roughness of thin films deposited with different substrate temperature computed using different simulation lattice size.

show qualitative agreement with the results from the larger lattice runs. However, the result from the 20×20 lattice is inconsistent with all other results. Such results suggest that the lattice size used in the kMC simulation should be at least twice as large as the surface interaction radius (20 in this work) to capture the dynamics of the thin film growth process. Moreover, the stochastic noise of the simulation decreases with increasing lattice size. For this work in particular, simulation lattice size of 100×100 is large enough to describe the process dynamics with low stochastic noise, and therefore, such a lattice size (or larger) will be used in the subsequent simulations.

3.4 Feedback control

To obtain thin films of desired and reproducible surface microstructure, it is necessary to operate the deposition process under feedback control. In this process,

since there are two temperature regimes for which thin film surface morphologies are quite different, control of surface roughness in these two regimes is considered separately.

The final surface roughness of the thin film is selected as the controlled variable because this is the quantity of interest from a practical point of view. The manipulated variable is chosen to be the substrate temperature T, since, in low temperature CVD processes, such as PECVD, the substrate temperature is usually one of the few process variables that could be allowed to vary in practice. Moreover, the manipulation of substrate temperature is relatively easy and has been integrated on most deposition systems. The major disturbance to the deposition process is the variation of the gas phase composition. Such variation may be caused by gas flow spikes in the gas delivery system.

3.4.1 Surface roughness control in the low temperature regime

For thin film applications where high island density is desired, surface roughness control can be implemented on the low temperature regime, in which the growth process is dominated by short-range interactions. Real-time feedback control of deposition processes which are characterized by short-range interactions has been discussed in detail in [40, 41], where the control problem was formulated as regulation of instantaneous surface roughness. In this work, a feedback control scheme inspired by the methodology proposed in [40, 41] is developed to regulate the final surface roughness. To ensure that the surface of the thin film has a high island density, the substrate temperature is restricted within 600 K - 680 K.

Open-loop response

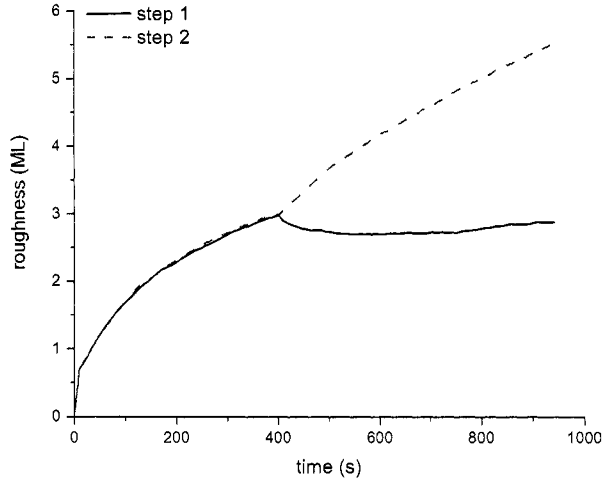

Figure 3.14: Response of surface roughness with respect to step changes in substrate temperature: a. T changes from 640 K to 680 K at t=400 s (step 1); b. T changes from 640 K to 600 K at t=400 s (step 2).

Fig.3.14 shows the response profiles of the surface roughness with respect to step changes (± 40 K) in the substrate temperature at time $t = 400$ s. We can see that the value of the surface roughness at the end of the deposition can be controlled by manipulating the substrate temperature. The final surface roughness can be computed based on the current thin film surface, the gas flux composition and the substrate temperature using the proposed kMC growth model. In all simulation runs, the final surface roughness is considered to be the roughness at $t = 950$ s.

Fig.3.15 shows the profiles of surface roughness with respect to disturbances in the gas phase composition (i.e., gas flux pattern). It can be seen that increasing concentration of A type macromolecules in the gas phase, i.e., increasing w_a^A, results in a rise in the final thin film surface roughness and vice versa. Therefore, feedback control is needed to reject such disturbances.

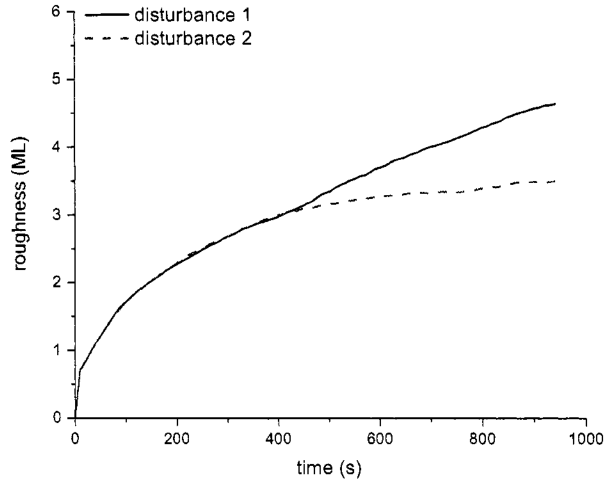

Figure 3.15: Response of surface roughness with respect to step disturbance in gas phase composition: a. gas phase composition changed from $50\%A + 50\%B$ to $70\%A + 30\%B$ (disturbance 1); b. gas phase composition changed from $50\%A+50\%B$ to $30\%A+70\%B$ (disturbance 2).

Controller design - closed-loop simulation

Based on the open-loop system analysis, a real-time surface roughness feedback control scheme is designed for the process. Fig.3.16 shows the block diagram of the closed-loop system. The thin film growth is influenced by the substrate temperature and the macromolecule adsorption rates which are determined by gas phase composition. Since we choose the final surface roughness as the variable to control, an estimate is computed for every control cycle using the proposed kMC model based on the operating conditions and the thin film surface configuration which can be measured in real-time by advanced surface characterization tools such as the GISAXS [57].

The substrate temperature, is then computed based on a proportional integral

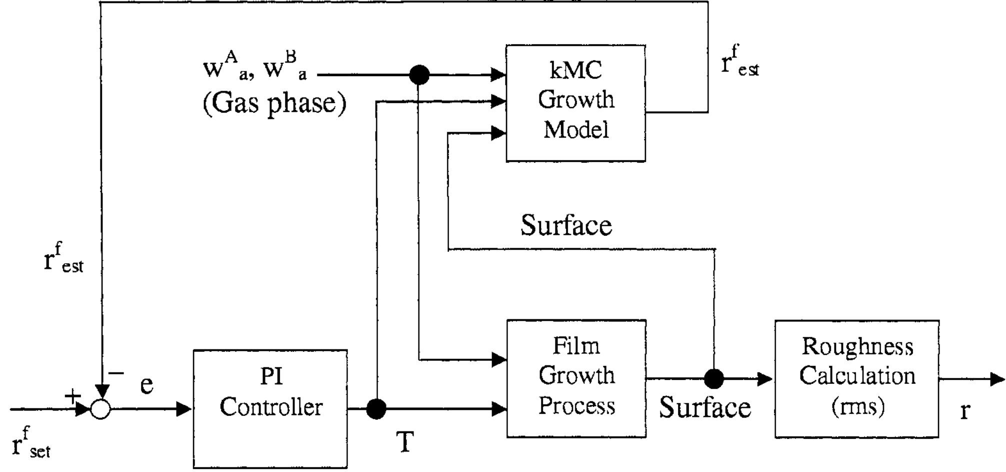

Figure 3.16: Block diagram of the closed-loop system.

(PI) control algorithm as follows:

$$T(t) = K_c\hat{e}(t) + K_i \int_{t_0}^{t} \hat{e}(\mu)d\mu + T_0 \tag{3.8}$$

$$\hat{e}(t) = \begin{cases} e(t) & |e(t)| > \epsilon \\ 0 & |e(t)| \leq \epsilon \end{cases} \tag{3.9}$$

where $T(t)$ is the controller output (i.e., substrate temperature), T_0 is the initial substrate temperature, K_c is the proportional gain, K_i is the integral gain, $e(t)$ is the error of the final surface roughness (i.e., the difference between the desired final surface roughness and the estimated final surface roughness computed using the proposed kMC model based on the surface configuration and operating conditions at the instance of last control action) and ϵ is the error tolerance ($\epsilon = 0.05$ in this work).

The closed-loop thin film growth process which employs the proposed real-time feedback control scheme has been simulated. The controller parameters K_c and K_i are set to be -0.1 and -0.5 respectively. For all the closed-loop simulations, the deposition duration is set to be $950s$ and the adsorption rates w_a^A and w_a^B are

both set to be $0.05s^{-1}$. The estimator and controller are activated at $t = 400s$ and the control action is applied to the process every 10 s.

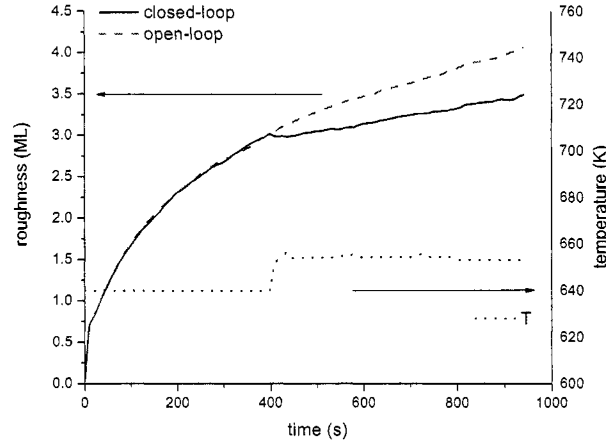

Figure 3.17: Temperature and surface roughness profiles with surface roughness set-point value of $3.5ML$: a. closed-loop surface roughness (solid line, left scale); b. open-loop surface roughness (dashed line, left scale); c. substrate temperature (dotted line, right scale).

Fig.3.17 shows the temperature and surface roughness profiles with final surface roughness set-point value of $3.5ML$. It can be seen that the surface roughness value of the thin film at the end of the deposition has been controlled at the desired value which is 12.5% lower than the surface roughness of the thin film deposited by open-loop deposition with the same initial deposition conditions.

Fig.3.18 shows the temperature and surface roughness profiles with final surface roughness set-point value of $3.5ML$. A disturbance in the gas phase composition is introduced in this simulation represented by a step change in the adsorption rates at $t = 400s$ to $t = 500s$. Specifically, w_a^A changed from $0.05s^{-1}$ to $0.1s^{-1}$ and w_a^B changed from $0.05s^{-1}$ to $0s^{-1}$ at $t = 400s$, while at $t = 500s$, w_a^A and w_a^B both changed back to $0.05s^{-1}$. It can be seen that the surface roughness of the thin

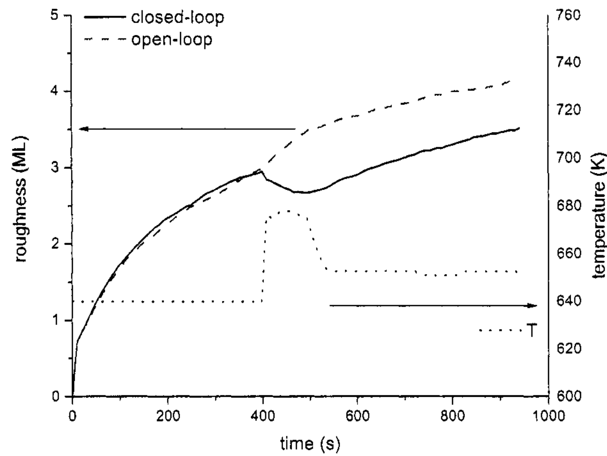

Figure 3.18: Temperature and surface roughness profiles with surface roughness set-point value of $3.5ML$ in the presence of disturbance: a. closed-loop surface roughness (solid line, left scale); b. open-loop surface roughness (dashed line, left scale); c. substrate temperature (dotted line, right scale).

film at the end of the deposition has been controlled at the desired value in spite of the disturbance in the gas phase, while the thin film deposited by open-loop deposition has a surface roughness 19.2% higher than the desired value due to the disturbance.

3.4.2 Surface roughness control in the high temperature regime

For thin film applications where large island size is desired, surface roughness control can be implemented for the high temperature regime, in which the growth process is dominated by long-range interactions. To ensure the surface of the thin film has a low island density, the substrate temperature is restricted within the range of 680 K $\sim$ 840 K.

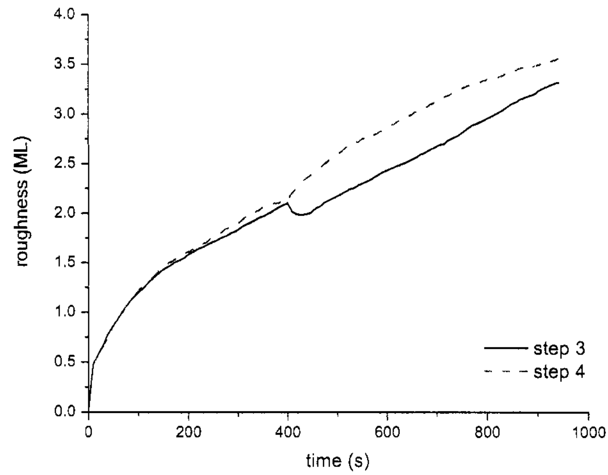

Figure 3.19: Response of surface roughness with respect to step changes in substrate temperature: a. T changes from 740 K to 820 K at t=400 s (step 3); b. T changes from 740 K to 660 K at t=400 s (step 4).

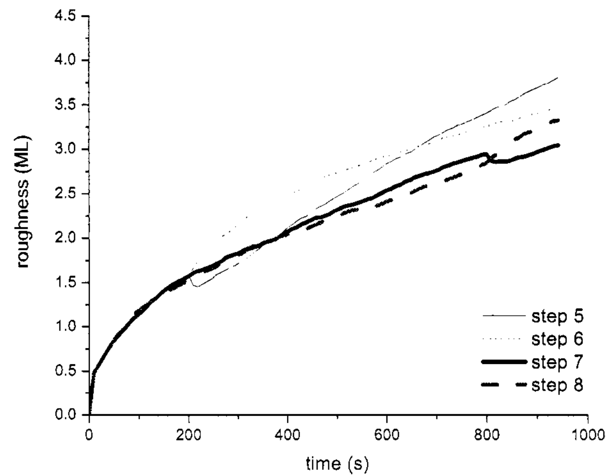

Figure 3.20: Response of surface roughness with respect to step changes in substrate temperature: a. T changes from 740 K to 820 K at t=200 s (step 5); b. T changes from 740 K to 660 K at t=200 s (step 6); c. T changes from 740 K to 820 K at t=800 s (step 7); d. T changes from 740 K to 660 K at t=800 s (step 8).

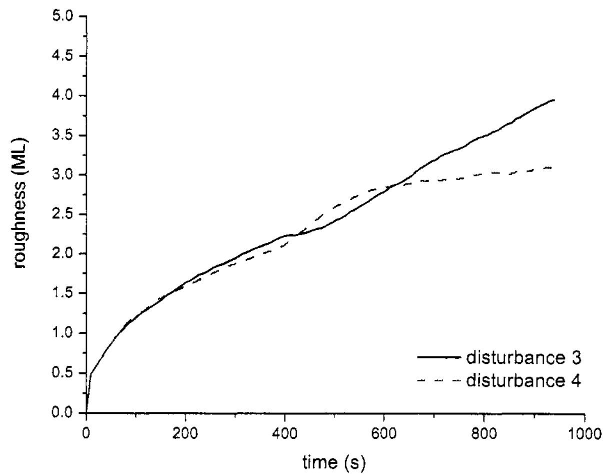

Figure 3.21: Response of surface roughness with respect to step disturbance in gas phase composition: a. gas phase composition changed from $50\%A + 50\%B$ to $80\%A + 20\%B$ (disturbance 3); b. gas phase composition changed from $50\%A+50\%B$ to $20\%A+80\%B$ (disturbance 4).

Open-loop response

Fig.3.19 shows the response profiles of the surface roughness with respect to step changes (± 80 K) in substrate temperature at time $t = 400$ s. We can see that, in the high temperature regime, the value of the surface roughness at the end of the deposition can also be controlled by manipulating the substrate temperature. However, the responses to step changes in substrate temperature exhibit inverse dynamics as shown in Fig.3.20. This result suggests that a more advanced controller may be needed to control the surface roughness in the high temperature regime. Fig.3.21 shows the profiles of surface roughness with respect to disturbances in the gas phase composition (i.e., gas flux pattern). It can be seen that, in the high temperature regime, the effect of disturbance in the gas phase composition on the surface roughness also leads to inverse response, and thus, the

proposed growth model is needed to predict the evolution of the surface roughness.

Controller design - PI control

The high temperature regime closed-loop thin film growth process which employs the proposed real-time feedback control scheme for the low temperature regime but with different controller parameters has been simulated. The controller parameters K_c and K_i are set to be -2 and -0.2, respectively.

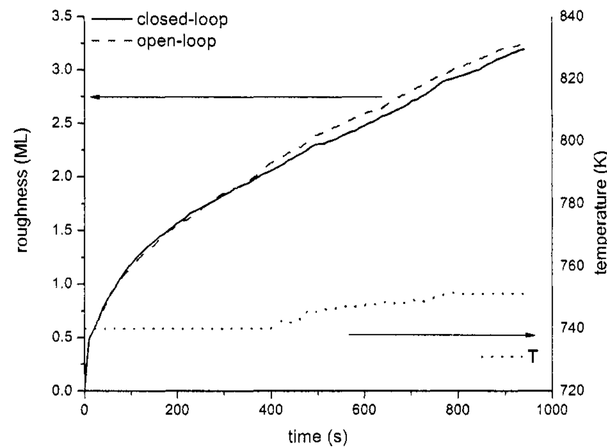

Figure 3.22: Temperature and surface roughness profiles with surface roughness set-point value of $3.2ML$: a. closed-loop surface roughness (solid line, left scale); b. open-loop surface roughness (dashed line, left scale); c. substrate temperature (dotted line, right scale).

Fig.3.22 shows the temperature and surface roughness profiles with final surface roughness set-point value of $3.2ML$. It can be seen that the surface roughness value of the thin film at the end of the deposition has been controlled at the desired value which is about the same as the surface roughness of the thin film deposited by open-loop deposition with the same initial deposition conditions.

Fig.3.23 shows the temperature and surface roughness profiles with final surface

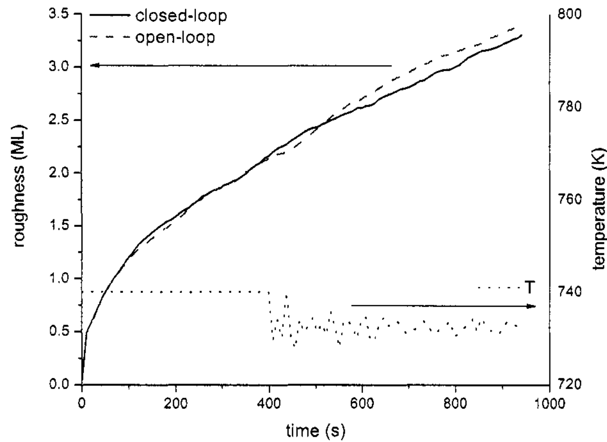

Figure 3.23: Temperature and surface roughness profiles with surface roughness set-point value of $3.2ML$ in the presence of disturbance: a. closed-loop surface roughness (solid line, left scale); b. open-loop surface roughness (dashed line, left scale); c. substrate temperature (dotted line, right scale).

roughness set-point value of $3.2ML$. A disturbance in the gas phase composition is introduced in this simulation in terms of a step change in the adsorption rates at $t = 400s$ to $t = 420s$. Specifically, w_a^A changed from $0.05s^{-1}$ to $0.1s^{-1}$ and w_a^B changed from $0.05s^{-1}$ to $0s^{-1}$ at $t = 400s$, while at $t = 420s$, w_a^A and w_a^B both changed back to $0.05s^{-1}$. It can be seen that the final surface roughness has been controlled at the desired value which is 5.9% lower than the one obtained under open-loop operation in spite of the disturbance in the gas phase.

Fig.3.24 shows the temperature and surface roughness profiles with final surface roughness set-point value of $3.2ML$. A disturbance in the gas phase composition is introduced in this simulation in terms of a step change in the adsorption rates at $t = 400s$ to $t = 500s$. Specifically, at $t = 400s$, w_a^A changed from $0.05s^{-1}$ to $0.1s^{-1}$ and w_a^B changed from $0.05s^{-1}$ to $0s^{-1}$, while at $t = 500s$, w_a^A and w_a^B both changed back to $0.05s^{-1}$. It can be seen that the surface roughness is not

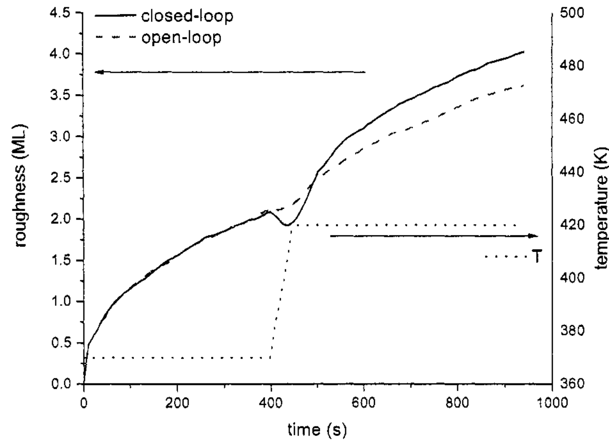

Figure 3.24: Temperature and surface roughness profiles with surface roughness set-point value of $3.2ML$ in the presence of disturbance: a. closed-loop surface roughness (solid line, left scale); b. open-loop surface roughness (dashed line, left scale); c. substrate temperature (dotted line, right scale).

controlled at the desired value and that the controller output hits the high limit of the control actuator. The final surface roughness is about 13.9% higher than the one obtained under open-loop operation. This suggests that the kMC estimator-based PI controller does not provide satisfactory closed-loop performance when the disturbance to the process is significant, and therefore, a more advanced control scheme is needed.

Controller design - kMC model-based predictive control

In order to achieve robust closed-loop operation in the high temperature regime, a kMC model-based predictive control scheme is proposed. Fig.3.25 shows the block diagram of the closed-loop system. A reference trajectory of the instantaneous surface roughness of the thin film is selected based on off-line optimization, and in this work for simplicity, the profile of the surface roughness of the thin film

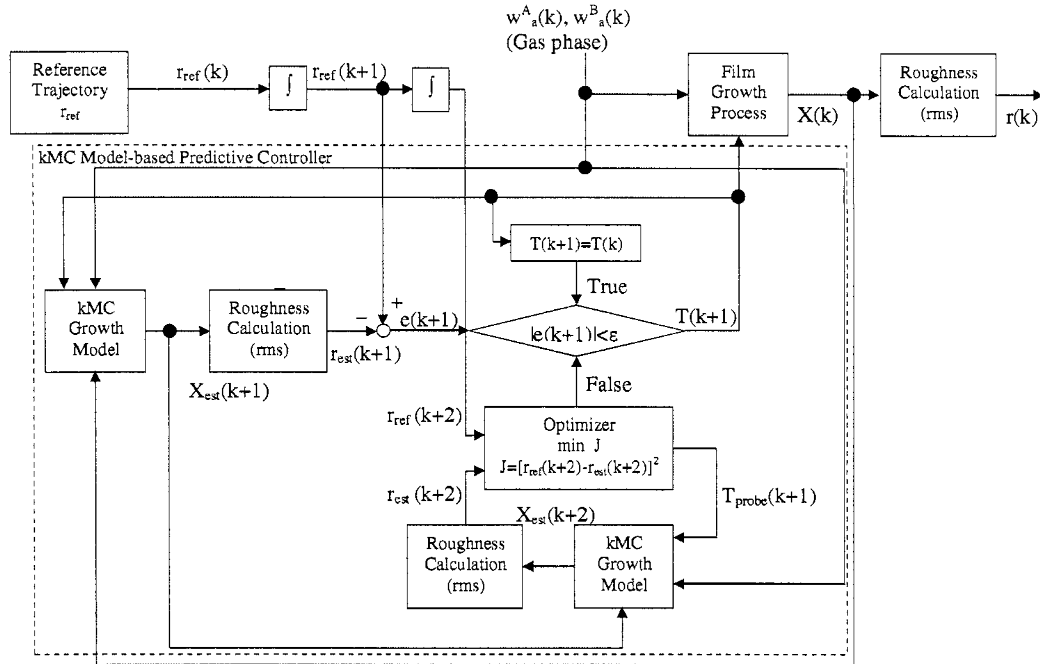

Figure 3.25: Block diagram of the closed-loop system with the kMC model-predictive controller.

in an ideal open-loop deposition (no disturbance is assumed to affect the process and the final surface roughness is taken to be the desired value) is chosen. Using such a reference trajectory, instead of solving the receding horizon optimization problem of minimizing the difference between the final surface roughness and the desired value with multiple decision variables, we only need to solve the fixed short horizon optimization problem of minimizing the difference between the instantaneous surface roughness and the reference value with a single decision variable. Therefore, the computation time of each optimization is greatly reduced, since the kMC simulation duration is reduced from the scale of the total deposition time to the controller turnover time. This is very important since kMC simulation is relatively time consuming and large scale numerical optimization using kMC models is almost impossible to solve in real-time.

During each control cycle, the surface configuration $X(k)$ (i.e., the height and the types of the top two macromolecules of each surface site) is first measured. An estimate of the surface configuration at the next control action time $X_{est}(k+1)$ is computed based on the current process conditions using the proposed kMC model, and the estimated surface roughness value $r_{est}(k+1)$ is compared with the reference value $r_{ref}(k+1)$. If the error is less than ε ($\varepsilon = 0.05$ in this work), the next controller output $T(k+1)$ is set to be the same as the current output $T(k)$. If the error is larger than ε, the optimizer is called to compute the output value of the next control action $T(k+1)$ so that the error between the surface roughness after the next control action $r(k+2)$ and the reference value $r_{ref}(k+2)$ is minimized.

The optimizer uses direct search to find the optimal solution since the kMC model does not have a closed-form expression. The estimate of the surface roughness after the next control action $r_{est}(k+1)$ is computed using the proposed kMC model based on the estimated surface configuration before the next control action $X_{est}(k+1)$, the probe output value $T_{probe}(k+1)$ and current process conditions. The search precision specified in this work is 2 K, and since the proposed kMC model is highly computationally efficient, the optimization problem can be solved by an entry level personal computer within the controller turnover time (10 s). Furthermore, the speed and the precision of the direct search optimization algorithm can be substantially improved by parallel computing.

Fig.3.26 shows the temperature and surface roughness profiles with final surface roughness set-point value of $3.2ML$. The reference trajectory is computed by averaging the open-loop surface roughness profiles from six independent simulation runs. It can be seen that the surface roughness value of the thin film follows the

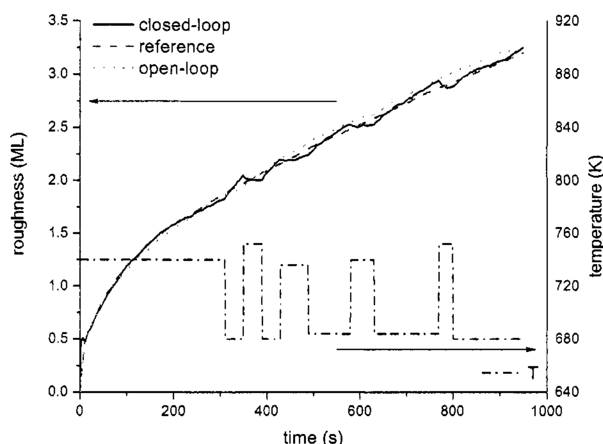

Figure 3.26: Temperature and surface roughness profiles with surface roughness set-point value of $3.2ML$: a. closed-loop surface roughness (solid line, left scale); b. reference surface roughness (dashed line, left scale); c. open-loop surface roughness (dotted line, left scale); d. substrate temperature (dashed dotted line, right scale).

reference trajectory closely and the final surface roughness has been controlled at the desired value.

Fig.3.27 shows the temperature and surface roughness profiles with final surface roughness set-point value of $3.2ML$. A disturbance in the gas phase composition is introduced in this simulation in terms of a change in the adsorption rates at $t = 400s$ to $t = 500s$, specifically, w_a^A changed from $0.05s^{-1}$ to $0.1s^{-1}$ and w_a^B changed from $0.05s^{-1}$ to $0s^{-1}$ at $t = 400s$, while at $t = 500s$, w_a^A and w_a^B both changed back to $0.05s^{-1}$. It can be seen that the surface roughness follows closely the reference trajectory and the final surface roughness has been controlled at the desired value which is 13.5% lower than the open-loop value. Compared to the failure of the PI controller on the same closed-loop simulation case, the kMC model-based predictive controller delivers substantially improved and robust closed-loop performance.

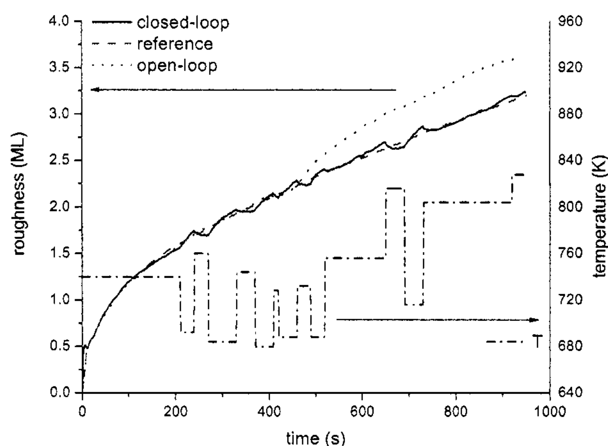

Figure 3.27: Temperature and surface roughness profiles with surface roughness set-point value of $3.2ML$: a. closed-loop surface roughness (solid line, left scale); b. reference surface roughness (dashed line, left scale); c. open-loop surface roughness (dotted line, left scale); d. substrate temperature (dashed dotted line, right scale).

3.5 Conclusions

In this chapter, a complex deposition process, which included two types of macromolecules whose growth behaviors were very different, was investigated. This deposition process was influenced by both short-range and long-range interactions. A multi-component kMC model was developed for the deposition. Both single-component and multi-component cases were simulated and the dependence of the surface microstructure of the thin film, such as island size and surface roughness, on substrate temperature and gas phase composition were studied. The surface morphology was found to be strongly influenced by these two factors and growth regimes governed by short-range and long-range interactions were observed. Furthermore, two kMC model-based feedback control schemes which use the substrate temperature to control the final surface roughness of the thin film

were proposed. The closed-loop simulation results demonstrated that robust deposition with controlled thin film surface roughness could be achieved under a kMC estimator-based PI feedback controller in the short-range interaction dominated growth regime, while a kMC model-predictive controller was needed to control the surface roughness in the long-range interaction dominated growth regime.

Chapter 4

Construction of Stochastic PDEs for Feedback Control of Surface Roughness in Thin Film Deposition

4.1 Introduction

In a thin film growth process, the film is directly formed from microscopic random processes (e.g., molecule adsorption, desorption, migration and surface reaction). Precise control of film properties requires models that describe these microscopic processes and directly account for their stochastic nature. Examples of such models include: 1) kinetic Monte-Carlo (kMC) methods [29, 23, 33], and 2) stochastic partial differential equations (PDEs) [20, 72].

Kinetic Monte-Carlo methods can be readily developed and can describe the microscopic growth processes to atomistic details with multiple species and both short-range and long-range interactions as discussed in Chapter 3. However, the

fact that kMC models are not available in closed-form makes very difficult to use them for system-level analysis and the design and implementation of real-time model-based feedback control systems. Motivated by this, an approach was reported in [63, 4] to identify linear deterministic models from outputs of kinetic Monte-Carlo simulators and design controllers using linear control theory to control macroscopic variables which are low statistical moments of the microscopic distributions (e.g., surface coverage, which is the zeroth moment of adspecies distribution on a lattice). However, to control higher statistical moments of the microscopic distributions, such as the surface roughness (the second moment of height distribution on a lattice), or even the microscopic configuration (such as the surface morphology), linear deterministic models may not be sufficient, because the effect of the stochastic nature of the microscopic processes becomes very significant and must be addressed both in the model construction and controller design.

Stochastic PDE models, on the other hand, which are available in closed-form, have been developed to describe the evolution of the height profile for surfaces in certain physical and chemical processes such as epitaxial growth [72] and ion sputtering [37]. More recently, Lou and Christofides [44] presented a method for feedback control of surface roughness in a thin film growth process whose surface height fluctuation can be described by the Edwards-Wilkinson equation [20], a second-order stochastic parabolic PDE (see also [42] for results on control of surface roughness in a sputtering process using the stochastic Kuramote-Sivashinsky equation). A feedback controller was designed based on the stochastic PDE model and successfully applied to the kMC model of the deposition process regulating the surface roughness to desired values. However, the construction of stochastic

PDE models for thin film growth processes directly based on microscopic process rules [46, 53, 71] is a very difficult task. This issue has prohibited the development of stochastic PDE models, and subsequently the design of model-based feedback control systems, for realistic deposition processes which are, in general, highly complex.

In this chapter, we develop a systematic method for the construction of linear stochastic PDE models for feedback control of surface roughness in thin film deposition. A linear stochastic PDE model is constructed for a generic thin film deposition process and is used to design a real-time feedback controller to control the thin film surface roughness. We initially reformulate a general linear stochastic PDE into a system of infinite stochastic ordinary differential equations (ODE) by using modal decomposition and derive the analytical expressions of the first and second statistical moments of the ODE states. Then, we use a kMC code to generate surface snapshots for different instants during process evolution to obtain values of the state vector of the stochastic ODE system. Subsequently, the eigenvalues and the covariance of the stochastic ODE system that correspond to the deposition process are computed based on the kMC simulation results. Finally, a linear stochastic PDE model is determined by least-square fitting the pre-derivative coefficients to match the spectrum of the stochastic PDE system to the identified spectrum of the stochastic ODE system. The dependence of the model parameters of the stochastic PDE on the process parameters is investigated and the least-square-optimal form of the stochastic PDE model with model parameters expressed as functions of the process parameters is determined. Furthermore, an optimization-based feedback controller is designed using the constructed stochastic PDE model and applied to the kMC simulation of the deposition process

to control the surface roughness. Closed-loop system simulation results demonstrate that the model is adequately accurate and that the controller is capable of controlling the surface roughness of the thin film.

4.2 Preliminaries

4.2.1 Thin film growth process

In this chapter, we consider a thin film growth process of deposition from vapor phase, in which, the formation of the thin film is governed by two microscopic processes that occur on the surface as shown in Fig.5.1, i.e., the adsorption of vapor phase molecules on the surface and the migration of surface molecules. This process is, in fact, a very common thin film growth process that can be traced in most chemical vapor deposition processes. A third microscopic process, the desorption of surface molecules, can also be added to constitute a more generic growth scheme, however, for the sake of conciseness of the demonstration of our methodology, it is not considered in this chapter.

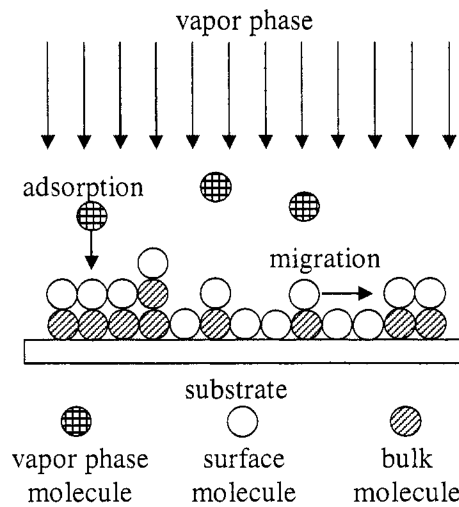

Figure 4.1: The thin film growth process.

More specifically, we consider a single species growth on a 1-dimensional lattice for simplicity (a full-scale model would consist of a 2-dimensional lattice, however, the extension of the approach proposed in this chapter to the 2-dimensional case is conceptually straightforward). The adsorption rate which depends on the vapor phase concentration is considered uniform over the spatial domain and constant (i.e., fixed growth rate) during each deposition, however, it could vary for different deposition runs. All surface sites are available for adsorption for all time and the adsorption rate for each surface site is given by:

$$w_a = W \tag{4.1}$$

where W is the growth rate in ML/s (monolayers per second).

The migration rate of each surface molecule depends on its local environment. Under the consideration of only first nearest-neighbor interactions, the migration rate of surface molecules from a surface site with n first nearest-neighbors is given by:

$$w_m(n) = k_{m0} e^{-\dfrac{E_s + nE_n}{k_B T}} \tag{4.2}$$

where E_s is the energy barrier associated with migration due to surface effects, E_n is the energy barrier associated with migration due to nearest neighbor interactions, k_{m0} is the frequency constant associated with migration, k_B is the Boltzmann's constant and T is the substrate temperature. The values of migration energy barriers and frequency constant used in this study are taken from the literature [62] for a molecular beam epitaxy $GaAs$ process and are as follows: $E_s = 1.58\ eV$, $E_n = 0.28\ eV$ and $k_{m0} = 2k_BT/h$, where h is the Planck's constant.

A kinetic Monte-Carlo simulation code following the algorithm reported in [70] is used to simulate the deposition process and obtain surface snapshots. First,

the surface molecules are grouped into three classes based on the number of first nearest-neighbors (from 0 to 2 neighbors); in each class, the molecules have the same migration rate and the adsorption rate is site independent. Then, a random number is generated to select an event to be executed based on the rates; if the event is migration, the class in which the event will occur is also selected. After that, a second random number is generated to select the site where the event will be executed; if the event is adsorption, the site is randomly picked among all the sites in the entire lattice; if the event is migration, the site is randomly picked from the list of the sites in the selected class. After the site is selected, the Monte-Carlo event is executed. If the event is adsorption, it is executed by adding one molecule on the selected site; if the event is migration, the molecule on the site is moved to one of the vacant neighboring sites with equal probability. Upon an executed event, a time increment τ is added to the process time t, computed based on the following equation (see [29] for a detailed proof):

$$\tau = -\frac{\ln \zeta}{w_a k_{max} + \sum_{n=0}^{2} N_n w_m(n)} \tag{4.3}$$

where ζ is a random number that follows the uniform distribution in the unit interval, N_n^A is the number of surface molecules with n first nearest neighbors and k_{max} is the total number of surface sites. Furthermore, periodic boundary conditions are used in the kMC simulation to satisfy the mass balance of the migration of the surface molecules.

4.2.2 Stochastic PDE model

As we discussed in the introduction, although there exist many first principles-based simulation codes for simulating the microscopic processes, most of them are

computationally very expensive. Therefore, closed-form stochastic PDE models are favored for applications in which computation efficiency is essential, such as, for the purpose of model-based real-time feedback control.

Without any *a priori* knowledge of the deposition process, we assume that there exists a one-dimensional linear stochastic PDE of the following general form that can adequately describe the evolution of the surface of the thin film during the deposition:

$$\frac{\partial h}{\partial t} = c + c_0 h + c_1 \frac{\partial h}{\partial x} + c_2 \frac{\partial^2 h}{\partial x^2} + \cdots + c_w \frac{\partial^w h}{\partial x^w} + \xi(x,t) \tag{4.4}$$

where $x \in [0, \pi]$ is the spatial coordinate, t is the time, $h(x,t)$ is the height of the surface at position x and time t, and $\xi(x,t)$ is a Gaussian noise with zero mean and covariance:

$$\langle \xi(x,t)\xi(x',t') \rangle = \varsigma^2 \delta(x-x')\delta(t-t') \tag{4.5}$$

where $\delta(\cdot)$ is the Dirac function. Furthermore, the pre-derivative coefficients c and c_j in Eq.5.4 and the parameter ς^2 in Eq.5.5 depend on the process parameters (gas flow rates, substrate temperature, etc.) $p_i(t)$:

$$\begin{array}{rcl} c & = & C[p_1(t), p_2(t), \cdots, p_d(t)] \\ c_j & = & C_j[p_1(t), p_2(t), \cdots, p_d(t)] \quad j = 0, \cdots, w \\ \varsigma^2 & = & C_\xi[p_1(t), p_2(t), \cdots, p_d(t)] \end{array} \tag{4.6}$$

where $C(\cdot)$, $C_j(\cdot)$ and $C_\xi(\cdot)$ are nonlinear functions to be determined.

The stochastic PDE of Eq.5.4 is subjected to the following periodic boundary conditions:

$$\frac{\partial^j h}{\partial x^j}(0,t) = \frac{\partial^j h}{\partial x^j}(\pi,t) \quad j = 0, \cdots, w-1 \tag{4.7}$$

and the initial condition:

$$h(x,0) = h_0(x) \tag{4.8}$$

Remark 4.1 *In this chapter, we assume that a linear stochastic PDE model adequately describes the process dynamics, however, for the cases in which the nonlinear dynamics are significant, nonlinear stochastic PDE models would be needed. Also, we note that we use a scaler function, $h(\cdot)$, to represent the height profile of the thin film surface in the model. In general, $h(\cdot)$ can be a vector function and be used to represent any appropriate microscopic description of the thin film (such as the defect locations, grain boundaries, etc), in such a case, several stochastic PDEs should be considered simultaneously.*

To study the dynamics of Eq.5.4, we initially consider the eigenvalue problem of the linear operator of Eq.5.4, which takes the form:

$$\begin{aligned} A\phi_n(x) &= c_0\phi_n(x) + c_1\frac{d\phi_n(x)}{dx} + c_2\frac{d^2\phi_n(x)}{dx^2} + \cdots + c_w\frac{d^w\phi_n(x)}{dx^w} = \lambda_n\phi_n(x) \\ \frac{d^j\phi_n}{dx^j}(0) &= \frac{d^j\phi_n}{dx^j}(\pi) \quad j = 0, \cdots, w-1 \quad n = 1, \cdots, \infty \end{aligned} \tag{4.9}$$

where λ_n denotes an eigenvalue and ϕ_n denotes an eigenfunction. A direct computation of the solution of the above eigenvalue problem yields:

$$\begin{aligned} \lambda_n &= c_0 + I2nc_1 + (I2n)^2c_2 + \cdots + (I2n)^w c_w \\ \phi_n(x) &= \sqrt{\frac{1}{\pi}}e^{I2nx} \quad n = 0, \pm1, \cdots, \pm\infty \end{aligned} \tag{4.10}$$

where λ_n denotes the nth eigenvalue, $\phi_n(x)$ denotes the nth eigenfunction and $I = \sqrt{-1}$.

To present the method that we use for parameter identification of the stochastic PDE of Eq.5.4, we first derive an infinite stochastic ODE representation of Eq.5.4 using modal decomposition and parameterize the infinite stochastic ODE system using kMC simulation. We first expand the solution of Eq.5.4 in an infinite series in terms of the eigenfunctions of the operator of Eq.5.9 as follows (i.e., the Fourier expansion in the complex form):

$$h(x,t) = \sum_{n=-\infty}^{\infty} z_n(t)\phi_n(x) \tag{4.11}$$

where $z_n(t)$ are time-varying coefficients. Substituting the above expansion for the solution, $h(x,t)$, into Eq.5.4 and taking the inner product, the following system of infinite stochastic ODEs is obtained:

$$\frac{dz_n}{dt} = \lambda_n z_n + c_{zn} + \xi_n(t) \quad n = 0, \pm 1, \cdots, \pm\infty \tag{4.12}$$

and the initial conditions:

$$z_n(0) = z_{n0} \quad n = 0, \pm 1, \ldots, \pm\infty \tag{4.13}$$

where $c_{zn} = c\int_0^\pi \phi_n^*(x)dx$ (apparently $c_{z0} = c\sqrt{\pi}$ and $c_{zn} = 0 \;\forall\; n \neq 0$), $\xi_n(t) = \int_0^\pi \xi(x,t)\phi_n^*(x)dx$ and $z_{n0} = \int_0^\pi h_0(x)\phi_n^*(x)dx$. $\phi_n^*(x)$ is the complex conjugate of $\phi_n(x)$, the superscript star is used to denote complex conjugate in the remainder of this manuscript.

The covariances of $\xi_n(t)$ can be computed by using the following result:

Result 4.1 *If (1) $f(x)$ is a deterministic function, (2) $\eta(x)$ is a random variable with $\langle\eta(x)\rangle = 0$ and covariance $\langle\eta(x)\eta(x')\rangle = \sigma^2\delta(x-x')$, and (3) $\epsilon = \int_a^b f(x)\eta(x)dx$, then ϵ is a random number with $\langle\epsilon\rangle = 0$ and covariance $\langle\epsilon^2\rangle = \sigma^2\int_a^b f(x)f^*(x)dx$ [5].*

Using Result 5.1, we obtain $\langle\xi_n(t)\rangle = 0$ and $\langle\xi_n(t)\xi_n^*(t')\rangle = \varsigma^2\delta(t-t')$. We note that $\xi_n(t)$ is a complex Gaussian random variable and the probability distribution function of the Gaussian distribution, $P(\xi_n, t)$, on the complex plane with zero mean and covariance $\varsigma^2\delta(t-t')$ is defined as follows:

$$P(\xi_n, t) = \frac{1}{\sqrt{2\pi}\varsigma\delta(t-t')} e^{\frac{\xi_n\xi_n^*}{2\varsigma^2\delta(t-t')}} \tag{4.14}$$

To parameterize this system of infinite stochastic ODEs, we first derive the analytic expressions for the statistical moments of the stochastic ODE states,

including the expected value and covariance. By comparing the analytical expression to the statistical moments obtained by multiple kMC simulations, the parameters of the stochastic ODE system (i.e., λ_n and ς) can be determined.

The analytic solution of Eq.5.12 is obtained as follows to derive the expressions for the statistical moments of the stochastic ODE states:

$$z_n(t) = e^{\lambda_n t} z_{n0} + \frac{(e^{\lambda_n t} - 1)c_{zn}}{\lambda_n} + \int_0^t e^{\lambda_n (t-\mu)} \xi_n(\mu) d\mu \tag{4.15}$$

Using Result 5.1, Eq.5.14 can be further simplified as follows:

$$z_n(t) = e^{\lambda_n t} z_{n0} + \frac{(e^{\lambda_n t} - 1)c_{zn}}{\lambda_n} + \theta_n(t) \tag{4.16}$$

where $\theta_n(t)$ is a complex random variable of normal distribution with zero mean and covariance $\langle \theta_n(t)\theta_n^*(t)\rangle = \varsigma^2 \dfrac{e^{(\lambda_n + \lambda_n^*)t} - 1}{\lambda_n + \lambda_n^*}$. Therefore, the expected value (the first stochastic moment) and the covariance (the second stochastic moment) of state z_n can be expressed as follows:

$$\begin{aligned}
&\langle z_n(t)\rangle = e^{\lambda_n t} z_{n0} + \frac{(e^{\lambda_n t} - 1)c_{zn}}{\lambda_n} \\
&\langle z_n(t) z_n^*(t)\rangle = \varsigma^2 \frac{e^{(\lambda_n + \lambda_n^*)t} - 1}{\lambda_n + \lambda_n^*} + \langle z_n(t)\rangle \langle z_n(t)\rangle^* \\
&n = 0, \pm 1, \cdots, \pm\infty
\end{aligned} \tag{4.17}$$

Eq.5.16 holds for any initial condition z_{n0}. Since we are able to choose any initial thin film surface for simulation, we choose $z_{n0} = 0$ (i.e., the initial surface is flat, $h(x, 0) = 0$) to simplify our calculations. In this case, Eq.5.16 can be further simplified as follows (note that $c_{zn} = 0, \forall n \neq 0$):

$$\begin{aligned}
&\langle z_n(t)\rangle = 0 \\
&\langle z_n(t) z_n^*(t)\rangle = \varsigma^2 \frac{e^{(\lambda_n + \lambda_n^*)t} - 1}{\lambda_n + \lambda_n^*} = \varsigma^2 \frac{e^{2Re(\lambda_n)t} - 1}{2Re(\lambda_n)} \\
&n = \pm 1, \cdots, \pm\infty
\end{aligned} \tag{4.18}$$

where $Re(\lambda_n)$ denote the real part of λ_n, and for $z_0(t)$, it follows from Eq.5.16 with $\lambda_0 = 0$ that,

$$\begin{aligned} \langle z_0(t)\rangle &= \lim_{\lambda_0\to 0}\frac{(e^{\lambda_0 t}-1)c_{z0}}{\lambda_0} = tc_{z0} = t\sqrt{\pi}c \\ \langle z_0^2(t)\rangle &= \varsigma^2 t + t^2\pi c^2 \end{aligned} \tag{4.19}$$

It can be seen in Eq.5.17 that the statistical moments of each stochastic ODE state depend only on the real part of the corresponding eigenvalue, and therefore, to determine the imaginary part of the eigenvalue we need to construct an extra equation. We note that λ_n would be a complex number if the linear operator A is not self-adjoint, i.e., when odd-partial-derivatives are present in the stochastic PDE (see Eq.5.10).

Therefore, we rewrite Eq.5.14 by separating the real part and the imaginary part of $z_n(t)$ as follows with initial condition $z_{n0} = 0$:

$$\begin{aligned} z_n(t) &= \frac{1}{2}\int_0^t [e^{\lambda_n(t-\mu)} + e^{\lambda_n^*(t-\mu)}]\xi_n(\mu)d\mu \\ &+\frac{1}{2}\int_0^t [e^{\lambda_n(t-\mu)} - e^{\lambda_n^*(t-\mu)}]\xi_n(\mu)d\mu \\ & n = \pm 1,\cdots,\pm\infty \end{aligned} \tag{4.20}$$

Accordingly, the real part of $z_n(t)$ can be expressed as follows:

$$\begin{aligned} &Re[z_n(t)] = \frac{1}{2}\int_0^t [e^{\lambda_n(t-\mu)} + e^{\lambda_n^*(t-\mu)}]\xi_n(\mu)d\mu \\ &n = \pm 1,\cdots,\pm\infty \end{aligned} \tag{4.21}$$

where $Re[z_n(t)]$ denotes the real part of $z_n(t)$. By using result 5.1 we have,

$$\begin{aligned}
\langle Re[z_n(t)] \rangle &= 0 \\
\langle Re[z_n(t)]^2 \rangle &= \varsigma^2 [\frac{\lambda_n^* e^{2\lambda_n t} + \lambda_n e^{2\lambda_n^* t} - (\lambda_n + \lambda_n^*)}{8\lambda_n \lambda_n^*} + \frac{e^{(\lambda_n + \lambda_n^*)t} - 1}{2(\lambda_n + \lambda_n^*)}] \\
&= \varsigma^2 \{ \frac{Re(\lambda_n) e^{2Re(\lambda_n)} cos(2Im(\lambda_n)t)}{4[Re(\lambda_n)^2 + Im(\lambda_n)^2]} \\
&\quad + \frac{Im(\lambda_n) e^{2Re(\lambda_n)} sin(2Im(\lambda_n)t)}{4[Re(\lambda_n)^2 + Im(\lambda_n)^2]} \\
&\quad - \frac{Re(\lambda_n)}{4[Re(\lambda_n)^2 + Im(\lambda_n)^2]} + \frac{e^{2Re(\lambda_n)t} - 1}{4Re(\lambda_n)} \} \\
&\quad n = \pm 1, \cdots, \pm\infty
\end{aligned} \tag{4.22}$$

where $Im(\lambda_n)$ denotes the imaginary part of λ_n. Thus, we can use Eq.5.17 to first determine the real part of the eigenvalue, and then use the Eq.5.21 to determine its imaginary part. We note that it is not recommended to determine both parts of the eigenvalue using only Eq.5.21, since in that case, the nonlinear least-square problem involved in the eigenvalue determination would be much more difficult to solve.

Remark 4.2 *Eq.5.17, Eq.5.18 and Eq.5.21 show the analytical relation that relates the linear operator and the Gaussian noise in Eq.5.4 to the statistical moments of the states of Eq.5.12 which can be obtained through multiple experimental measurements or first principle simulations, and therefore, reveal a viable path to systematically construct a linear stochastic PDE of the form of Eq.5.4 that describes the dynamics of the microscopic processes directly from experimental or simulation data.*

4.3 Model construction

Based on the results shown in the previous section, we propose a systematic procedure to construct a linear stochastic PDE for the deposition process described in Section 4.2.1. This procedure can be readily extended to other stochastic processes. In this chapter, we use a kinetic Monte-Carlo code to simulate the deposition process and generate surface snapshots.

The proposed procedure includes the following steps: First, we design a set of simulation experiments that cover the complete range of process operation; second, we run multiple simulations for each simulation experiment to obtain the trajectories of the first and second statistical moments of the states (i.e., Fourier coefficients) computed from the surface snapshots; third, we compute the eigenvalues of the linear operator and covariance of the Gaussian noise based on the trajectories of the statistical moments of the states for each simulation experiment, and determine the model parameters of the stochastic PDE (i.e., the pre-derivative coefficients and the order of the stochastic PDE); finally, we investigate the dependence of the model parameters of the stochastic PDE on the process parameters and determine the least-square-optimal form of the stochastic PDE model with model parameters expressed as functions of the process parameters.

4.3.1 Eigenvalues and covariance

Because there are only two process parameters considered in the deposition process studied in this chapter, the growth rate W and the substrate temperature T, the simulation experiment design is straightforward. Specifically, different W values and T values are evenly selected from the range of process operation of interest and simulation experiments are executed with every selected W value for each

selected T value. Therefore, we start our demonstration of the model construction methodology with the identification of the eigenvalues and covariance. Also, we note that the trajectories of the statistical moments for each simulation experiment are computed based on 100 simulation runs taking place with the same process parameters.

In the previous section we have shown that for a deposition process with a flat initial surface, the covariance of each state $\langle z_n(t)z_n^*(t)\rangle$ should be able to be predicted by Eq.5.17, therefore, we can fit ς^2 and $Re(\lambda_n)$ in Eq.5.17 for the profile of $\langle z_n(t)z_n^*(t)\rangle$.

In order to obtain the profile of $\langle z_n(t)z_n^*(t)\rangle$, we need to generate snapshots of the thin film surface during each deposition simulation and compute the values of $z_n(t)$. Since the lattice consists of discrete sites, we let $h(kL,t)$ be the height profile of the surface at time t with lattice constant L (k denotes the coordinate of a specific surface site), and compute $z_n(t)$ as follows:

$$z_n(t) = \int_0^{\pi} h(x,t)\phi_n^*(x)dx = \sum_{k=0}^{k_{max}} h(kL,t) \int_{kL}^{(k+1)L} \phi_n^*(x)dx \tag{4.23}$$

where $k_{max}L = \pi$ (i.e., the lattice is mapped to the domain $[0,\pi]$). Substituting Eq.5.10 into Eq.5.22, we can derive the following expression for $z_n(t)$:

$$z_n(t) = \sum_{k=0}^{k_{max}} \frac{h(kL,t)e^{-I2kLn}}{I2\sqrt{\pi}n}(1-e^{-I2Ln}) \quad n = \pm 1, \cdots, \pm\infty \tag{4.24}$$

and for $z_0(t)$, we have,

$$z_0(t) = \sum_{k=0}^{k_{max}} h(kL,t)\frac{L}{\sqrt{\pi}} = \sqrt{\pi}t\frac{\sum_{k=0}^{k_{max}} h(kL,t)}{k_{max}t} = t\sqrt{\pi}W \tag{4.25}$$

To capture the dynamics of both the fast states and slow states simultaneously in the same simulation run with few surface snapshots, the snapshots are generated

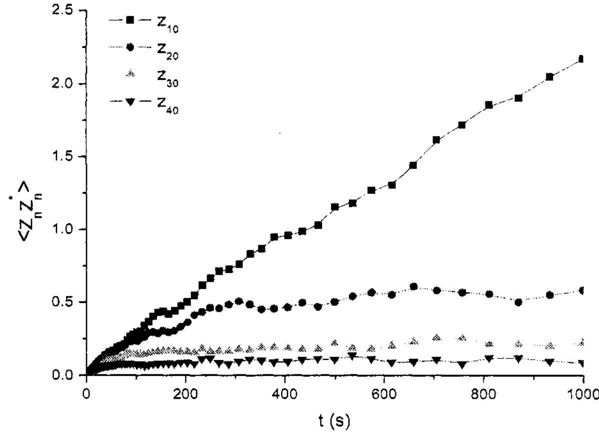

Figure 4.2: Covariance profiles of z_{10}, z_{20}, z_{30} and z_{40}.

in a variable-time-step fashion in which the intervals between two snapshots are increased with time. This procedure is motivated by the fact that the dynamics of the fast states can be detected only at the beginning of each simulation run, and therefore, the evolving surface should be sampled more frequently in the beginning than the remainder to cope with the small time scale of these fast states.

Fig.4.2 shows the typical covariance profiles of different states in a growth process. It can be seen that despite the very different time scales of the states, our method can still generate very smooth profiles for both the fast states (such as z_{40}, whose time scale is less than 50 s) and the slow states (such as z_{10}, whose time scale is larger than 1000 s).

Fig.5.2 shows the eigenvalues identified from thin film depositions occurring under the same operating conditions but simulated with different lattice size (we note that the identified eigenvalues are considered real since the imaginary part of the eigenvalues identified turned out to be very small). It can be seen that the identified spectrums are very close to each other when n is rescaled with the corresponding lattice size. This is expected, since, $\phi_n(x)$ is a basis of the domain

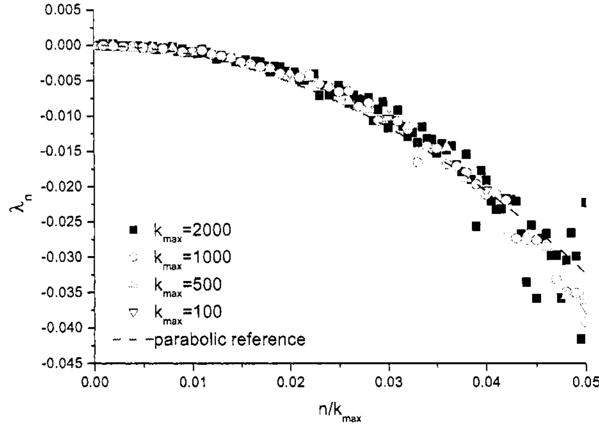

Figure 4.3: Eigenvalue spectrums of the infinite stochastic ODE systems identified from the kMC simulation of the deposition process with different lattice size: $k_{max} = 100$, $k_{max} = 500$, $k_{max} = 1000$ and $k_{max} = 2000$.

of operator A, and is a complex function of the frequency n, accordingly, n/k_{max} is the length scale of the surface fluctuation described by $\phi_n(x)$ when a lattice of size k_{max} is mapped to the domain of $[0, \pi]$ (we note that, for the same reason, the covariance values should be scaled with the inverse of the lattice size, $1/k_{max}$, in order to carry out a meaningful comparison).

It can also be seen in Fig.5.2 that the eigenspectrums are very close to the parabolic reference curve, which implies that a second-order stochastic PDE system of the following form would be able to describe the evolution of the surface height of this deposition process:

$$\frac{\partial h}{\partial t} = c + c_2 \frac{\partial^2 h}{\partial x^2} + \xi(x,t) \tag{4.26}$$

in which c, c_2 and the covariance of the Gaussian noise ξ, ς, all depend on the microscopic processes and operating conditions.

4.3.2 Dependence on the process parameters

We proceed now with the derivation of the parameters of the stochastic PDE of Eq.5.27. From Eq.5.18 and Eq.5.26, we can see that $c = W$ for all cases. However, c_2 and ς^2 identified for different deposition settings can be very different, therefore, we need to investigate their dependence on the deposition parameters to obtain their analytical expressions. c_2 and ς^2 are evaluated for assorted deposition conditions and a lattice size of 1000 (i.e., $k_{max} = 1000$) is used for all the simulation runs in our study.

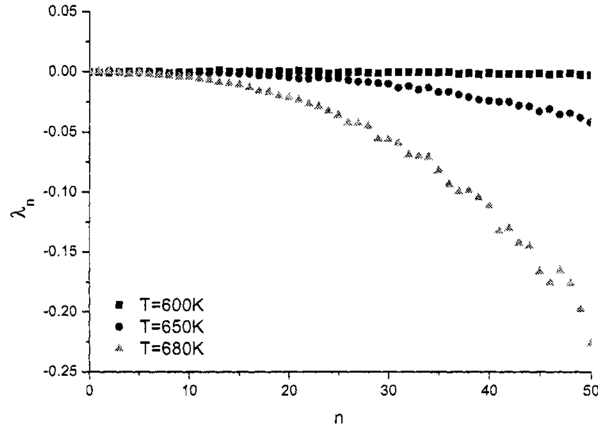

Figure 4.4: Eigenspectrums identified from simulated deposition processes with a growth rate $W = 0.5ML/s$ for different substrate temperatures: $T = 600K$, $T = 650K$ and $T = 680K$.

Fig.4.4 shows the eigenspectrums identified from depositions with the same growth rate ($W = 0.5\ ML/s$) for different substrate temperatures. It can be seen that the magnitude of the eigenvalues decreases faster with increasing n at higher substrate temperature. This implies that a higher substrate temperature corresponds to a larger c_2 in the stochastic PDE model and vice versa.

Fig.4.5 shows the covariance spectrums identified from depositions with the

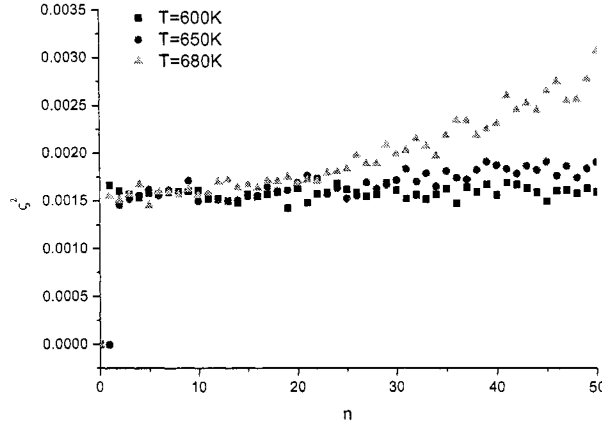

Figure 4.5: Covariance spectrums identified from simulated deposition processes with a growth rate $W = 0.5ML/s$ for different substrate temperatures: $T = 600K$, $T = 650K$ and $T = 680K$.

same growth rate ($W = 0.5\ ML/s$) for different substrate temperature. Although it follows from Eq.4.14 that the covariance of the stochastic noise should be the same for all states, it is not so for high-order states in the high substrate temperature regime (e.g., $T = 680\ K$). However, because these high order states correspond to the surface fluctuations of small length scales, and at the same time, such small length scale surface fluctuations are almost negligible in the high substrate temperature regime due to the significant surface diffusion, the contribution from these high-order states at high substrate temperature becomes very small. Therefore, given that such discrepancy would not significantly affect the accuracy of the model, we compute ς^2 only based on the low-order states. From the covariance of the low-order states shown in Fig.4.5, we may also consider ς^2 to be independent of substrate temperature.

Fig.4.6 shows the eigenspectrums identified from depositions occurring under the same substrate temperature ($T = 650\ K$) and different thin film growth

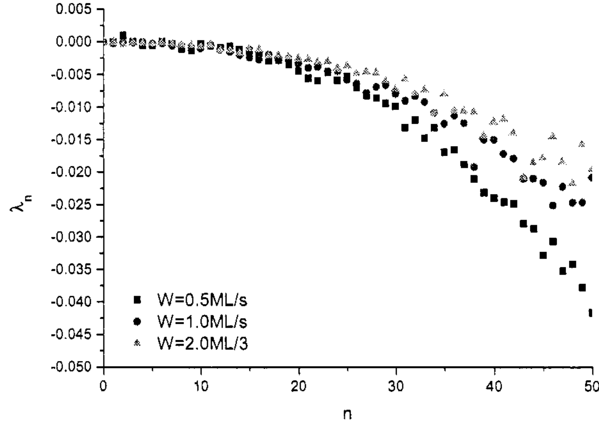

Figure 4.6: Eigenvalue spectrums identified from simulated deposition processes with a substrate temperature $T = 650K$ for different growth rates: $W = 0.5ML/s$, $W = 1.0ML/s$ and $W = 2.0ML/s$.

rates. It can be seen that, at this substrate temperature, the eigenvalues die out a bit slower with increasing growth rate, which implies that a higher growth rate corresponds to a smaller c_2 in the stochastic PDE model and vice versa.

Fig.4.7 shows the covariance spectrums identified from depositions occurring under the same substrate temperature ($T = 650\ K$) and different thin film growth rates. It can be seen that a higher growth rate corresponds to a larger covariance value.

To derive explicit expressions for c_2 and ς^2 as functions of T and W, we evaluate these values for different T and W and the results are shown in Fig.5.4 and Fig.4.9. From Fig.5.4, we can see that $ln\, c_2$ has a quasi-linear relationship with both T and W, and thus, the following expression can be obtained for c_2 as a function of T and W through least square fitting:

$$\begin{aligned} c_2(T, W) &= e^{-45.8176 + 0.0511T - 0.1620W} \\ &= \frac{e^{-32.002 + 0.0511T - 0.1620W}}{k_{max}^2} \end{aligned} \tag{4.27}$$

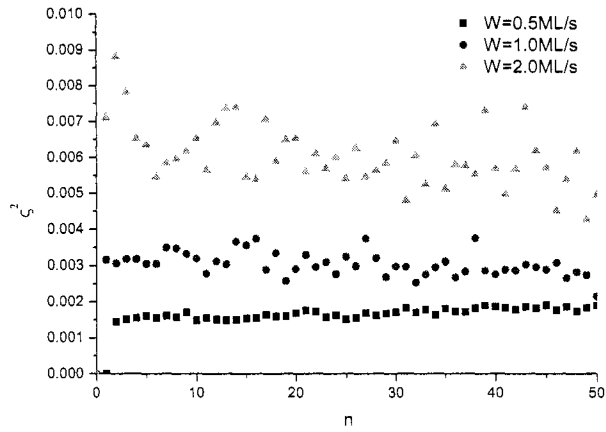

Figure 4.7: Covariance spectrums identified from simulated deposition processes with a substrate temperature $T = 650K$ for different growth rates: $W = 0.5ML/s$, $W = 1.0ML/s$ and $W = 2.0ML/s$.

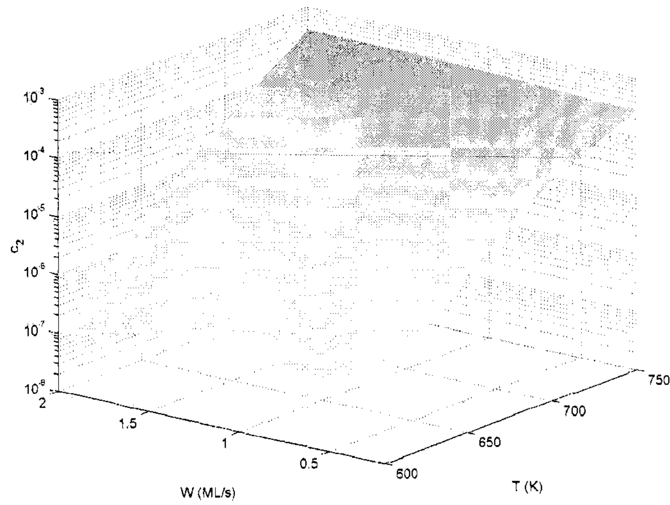

Figure 4.8: Profile of c_2 as a function of substrate temperature T and thin film growth rate W.

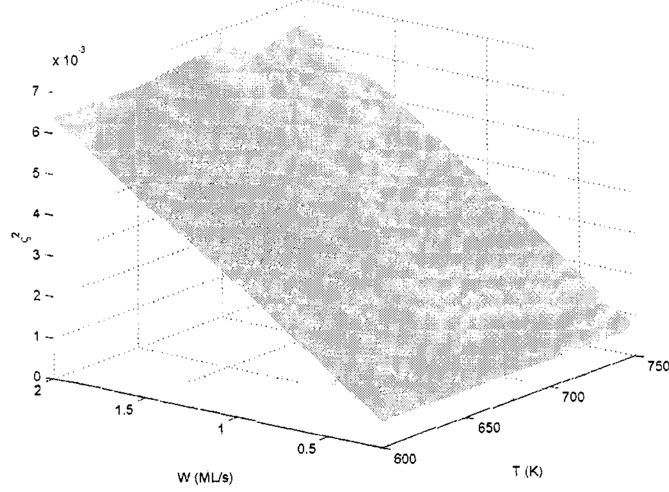

Figure 4.9: Profile of ς^2 as a function of substrate temperature T and thin film growth rate W.

From Fig.4.9 we can see that ς^2 depends almost linearly on both T and W, and thus, the following expression can be obtained for ς^2 as a function of T and W through least square fitting as well:

$$\varsigma^2(T, W) = 5.137 \times 10^{-8}T + 3.2003 \times 10^{-3}W \approx \frac{\pi W}{k_{max}} \tag{4.28}$$

Therefore, the linear stochastic PDE model identified for the deposition process is as follows:

$$\begin{aligned}
\frac{\partial h}{\partial t} &= W + (\frac{e^{-32.002 + 0.0511T - 0.1620W}}{k_{max}^2})\frac{\partial^2 h}{\partial x^2} + \xi(x, t) \\
\frac{\partial h}{\partial x}(0, t) &= \frac{\partial h}{\partial x}(\pi, t), \quad h(0, t) = h(\pi, t), \quad h(x, 0) = h_0(x)
\end{aligned} \tag{4.29}$$

where $\langle \xi(x, t)\xi(x', t') \rangle = \dfrac{5.137 \times 10^{-5}T + 3.2003W}{k_{max}}\delta(x - x')\delta(t - t')$.

4.3.3 Validation of stochastic PDE model

We now proceed with the validation of the stochastic PDE model of the thin film deposition process (Eq.5.31). Validation experiments are conducted for a number

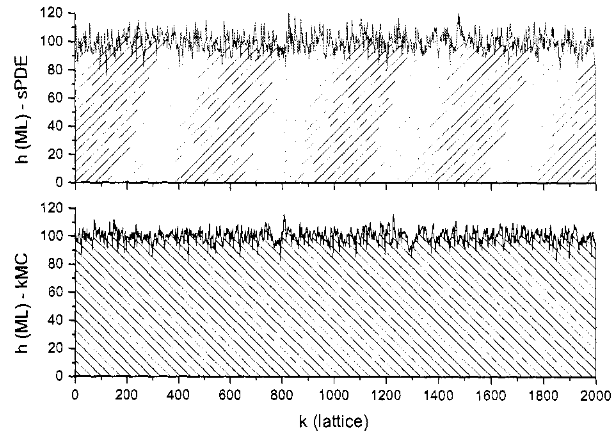

Figure 4.10: Final thin film surface profiles generated by kMC simulation and stochastic PDE model for a 1000s deposition with substrate temperature $T = 550K$, thin film growth rate $W = 0.1\ ML/s$ and lattice size $k_{max} = 2000$.

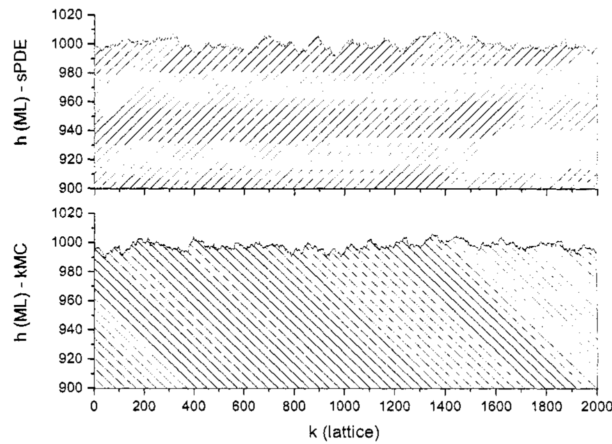

Figure 4.11: Final thin film surface profiles generated by kMC simulation and stochastic PDE model for a 400s deposition with substrate temperature $T = 700K$, thin film growth rate $W = 2.5\ ML/s$ and lattice size $k_{max} = 2000$.

of deposition conditions which have not been used for the model construction. We generate surface profiles using both the stochastic PDE model and the kinetic Monte-Carlo code. Fig.5.6 shows the surface profile at the end of a deposition with substrate temperature $T = 550\ K$, thin film growth rate $W = 0.1\ ML/s$, deposition duration of 1000 s and lattice size $k_{max} = 2000$; Fig.5.7 shows the surface profile at the end of a deposition with substrate temperature $T = 700\ K$, thin film growth rate $W = 2.5\ ML/s$, deposition duration of 400 s and lattice size $k_{max} = 2000$; we can see that both at low and high substrate temperatures, and for different growth rates, the linear stochastic PDE model constructed for the deposition process is very consistent with the kinetic Monte-Carlo simulation.

We also generate expected surface roughness profiles using both the stochastic PDE model and the kinetic Monte-Carlo simulation (average of 100 runs) for the deposition process. For simplicity, the surface roughness is evaluated in a root-mean-square fashion as follows:

$$r(t) = \sqrt{\frac{1}{\pi}\int_0^{\pi}[h(x,t) - \bar{h}(t)]^2 dx} \tag{4.30}$$

where $\bar{h}(t) = \frac{1}{\pi}\int_0^{\pi} h(x,t)dx$ is the average surface height. We note that for more detailed description of the surface morphology, the height-height correlation function may be used to evaluate the surface roughness [67].

Fig.5.8 shows the expected roughness profile of a deposition with substrate temperature $T = 550\ K$ and thin film growth rate $W = 0.1\ ML/s$; Fig.5.9 shows the roughness profile of a deposition with substrate temperature $T = 700\ K$ and thin film growth rate $W = 2.5\ ML/s$; we can see that the linear stochastic PDE model constructed for the deposition process is also very consistent with the kinetic Monte-Carlo simulation in terms of surface roughness, at both low and high substrate temperatures, for different growth rates.

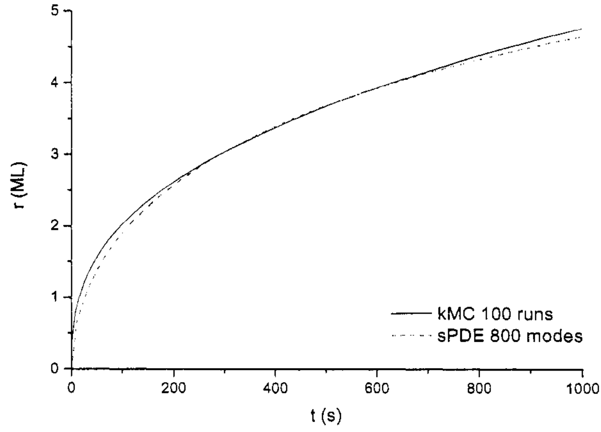

Figure 4.12: Expected surface roughness profiles generated by kMC simulation and stochastic PDE model for a 1000s deposition with substrate temperature $T = 550K$, thin film growth rate $W = 0.1\ ML/s$ and lattice size $k_{max} = 2000$.

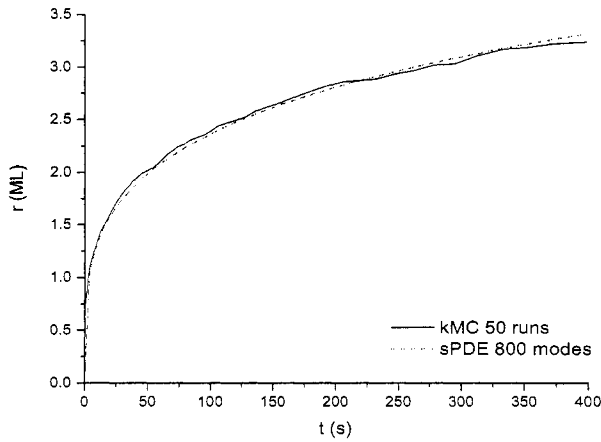

Figure 4.13: Expected surface roughness profiles generated by kMC simulation and stochastic PDE model for a 400s deposition with substrate temperature $T = 700K$, thin film growth rate $W = 2.5\ ML/s$ and lattice size $k_{max} = 2000$.

4.4 Feedback control

In this section, we design a model-based state feedback controller based on the stochastic PDE model of Eq.5.31 to control the thin film surface roughness of the deposition process. The difficulty of obtaining in-situ surface measurements in real-time had been one of the obstacles for implementing feedback control on thin film processes. Recently, researchers made possible to use some of the intrusive scanning probe based techniques such as the scanning tunneling microscopy (STM) [52] and atomic force microscopy (AFM) [45] in-situ, to observe in real-time the growth of the thin film. More recently, it was reported in [57] that a non-intrusive grazing incidence small angle x-ray scattering (GISAXS) method was successfully used to monitor the thin film growth in-situ in real-time; the method was capable of sampling large surface areas with sampling frequency up to 10 Hz and a subnanometer resolution. Such advancements in surface metrology indeed open up the possibility for implementing feedback control systems which rely on real-time surface state measurements. On the other hand, for the cases in which state measurements are not available directly, state estimators could be used to implement output feedback control based on available measurements such as thickness and surface roughness.

4.4.1 Surface roughness

We first proceed with the analysis of the dynamics of the surface roughness based on the stochastic PDE model constructed for the thin film deposition process. The surface roughness, $r(t)$, is defined by Eq.5.32. According to Eq.5.22, we have

$\bar{h}(t) = z_0(t)\phi_0$. Therefore, $r(t)$ can be rewritten in terms of z_n as follows:

$$\begin{aligned} r(t) &= \sqrt{\frac{1}{\pi}\int_0^{\pi}(h(x,t)-\bar{h}(t))^2dx} \\ &= \sqrt{\frac{1}{\pi}\int_0^{\pi}\sum_{n=-\infty,n\neq 0}^{\infty} z_n(t)\phi_n(x)\phi_n^*(x)z_n^*(t)dx} \\ &= \sqrt{\frac{1}{\pi}\sum_{n=-\infty,n\neq 0}^{\infty} z_n(t)z_n^*(t)} \end{aligned} \tag{4.31}$$

and the expected roughness can be computed as follows:

$$\langle r(t)\rangle = \sqrt{\frac{1}{\pi}\sum_{n=-\infty,n\neq 0}^{\infty}\langle z_n(t)z_n^*(t)\rangle} \tag{4.32}$$

In order to design a model-based feedback controller to control the surface roughness, we first derive the analytical expression for the trajectory of $\langle r(t)\rangle$. Substituting Eq.5.16 into Eq.5.34 we obtain the following expression for $\langle r(t)\rangle$ in terms of the eigenvalues of the infinite stochastic ODE system:

$$\begin{aligned} \langle r(t)\rangle &= \sqrt{\frac{1}{\pi}\sum_{n=-\infty,n\neq 0}^{\infty}[\varsigma^2\frac{e^{(\lambda_n+\lambda_n^*)t}-1}{\lambda_n+\lambda_n^*}+e^{(\lambda_n+\lambda_n^*)t}z_{n0}z_{n0}^*]} \\ &= \sqrt{\frac{1}{\pi}\sum_{n=-\infty,n\neq 0}^{\infty}[\varsigma^2\frac{e^{2Re(\lambda_n)t}-1}{2Re(\lambda_n)}+e^{2Re(\lambda_n)t}z_{n0}z_{n0}^*]} \end{aligned} \tag{4.33}$$

Specifically, for the stochastic PDE model of Eq.5.27, $\lambda_n = -4c_2n^2$, thus, Eq.4.33 can be rewritten as follows:

$$\begin{aligned} \langle r(t)\rangle &= \sqrt{\frac{1}{\pi}\sum_{n=-\infty,n\neq 0}^{\infty}(\varsigma^2\frac{e^{-8c_2n^2t}-1}{-8c_2n^2}+e^{-8c_2n^2t}z_{n0}z_{n0}^*)} \\ &= \sqrt{\frac{2}{\pi}\sum_{n=1}^{\infty}(\varsigma^2\frac{e^{-8c_2n^2t}-1}{-8c_2n^2}+e^{-8c_2n^2t}z_{n0}z_{n0}^*)} \end{aligned} \tag{4.34}$$

In order to compute an estimate of the excepted surface roughness at a future time t, we need to compute the infinite sum in Eq.5.35. However, such an infinite

summation cannot be computed directly, instead, a finite summation needs to be used to approximately compute this infinite sum. It can shown by using standard theory of infinite summation [35] that, if the following mth order approximation (only the first mth states are included in the summation) is used,

$$\begin{aligned} \hat{r}(t)^2 &= \frac{2}{\pi}\sum_{n=1}^{m}(\varsigma^2\frac{e^{-8n^2c_2t}-1}{-8n^2c_2}+e^{-8n^2c_2t}z_{n0}z_{n0}^*) \\ &+\frac{1}{2\pi}[e^{-8c_2(m+1)^2t}(\pi r_0^2-\sum_{n=1}^{m}z_{n0}z_{n0}^*)+\frac{\varsigma^2}{2^{m+2}c_2}] \end{aligned} \tag{4.35}$$

where r_0 is the initial roughness value, the approximation error would be subject to the following bound:

$$|\langle r(t)\rangle-\hat{r}(t)|\leq\sqrt{\frac{1}{2\pi}[e^{-8c_2(m+1)^2t}(\pi r_0^2-\sum_{n=1}^{m}z_{n0}z_{n0}^*)+\frac{\varsigma^2}{2^{m+2}c_2}]} \tag{4.36}$$

We note that the approximation error decreases with increasing m.

4.4.2 Feedback control design

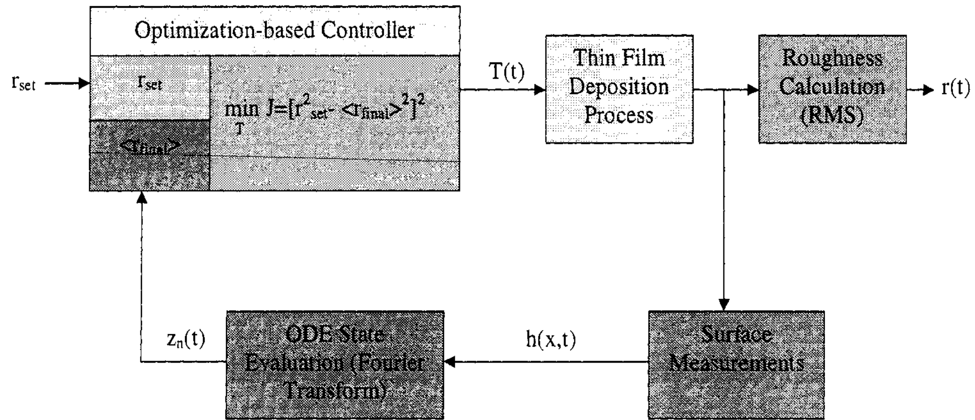

Figure 4.14: Block diagram of the closed-loop system.

We now proceed with the design of the feedback controller. Since the thin film deposition is a batch process, the control objective is to control the final surface roughness of the thin film to a desired level at the end of each deposition

run. Therefore, we use an optimization-based control problem formulation. The substrate temperature, T, is chosen to be the manipulated variable, while the thin film growth rate W is kept constant during each deposition. Furthermore, since the process is stochastic, the controlled variable is the expected value of the final surface roughness, $\langle r(t_{dep})\rangle$, where t_{dep} is the total deposition time.

Fig.5.11 shows the block diagram of the closed-loop system. When a real-time surface profile measurement is obtained, the states of the infinite stochastic ODE system, z_n, are computed. Then, a substrate temperature T is computed based on states z_n and the stochastic PDE model and applied to the deposition process. The substrate is held at this temperature for the rest of the deposition until a different value is assigned by the controller. The value of T is determined at each time t by solving, in real-time, the following optimization problem:

$$\min_{T} J = (r_{set}^2 - \langle r_{final}\rangle^2)^2 \tag{4.37}$$

subject to

$$\begin{aligned}\langle r_{final}\rangle^2 \;=\; & \frac{2}{\pi}\sum_{n=1}^{m}[\varsigma^2\frac{e^{-8n^2c_2(t_{dep}-t)}-1}{-8n^2c_2}+e^{-8n^2c_2(t_{dep}-t)}z_n(t)z_n^*(t)] \\ & +\frac{1}{2\pi}\{e^{-8c_2(m+1)^2(t_{dep}-t)}[\pi r^2(t)-\sum_{n=1}^{m}z_n(t)z_n^*(t)]+\frac{\varsigma^2}{2^{m+2}c_2}\}\end{aligned} \tag{4.38}$$

$$c_2 = \frac{e^{-32.002+0.0511T-0.1620W}}{k_{max}^2} \tag{4.39}$$

$$\varsigma^2 = \frac{\pi W}{k_{max}} \tag{4.40}$$

$$T_{min} \leq T \leq T_{max} \tag{4.41}$$

where T_{min} and T_{max} are the lowest and highest substrate temperature, respectively. We note that J corresponds to the difference between the square of the desired final surface roughness r_{set} and the square of the estimated final surface

roughness $\langle r_{final} \rangle$ computed based on the current states z_n. We choose to minimize the difference of the squares of the surface roughness, i.e., the mean square of the surface height, to simplify the calculation.

The first equality constraint Eq.4.38 (essentially the same as Eq.4.35) states that the estimate of the final surface roughness, r_{final}, is computed based on current states $z_n(t)$ under the assumption that a substrate temperature T will be used and kept constant in the rest of the deposition. The second and third equality constraints are, in fact, Eqs.5.29 and 5.30 of the stochastic PDE model of the deposition process, and since the growth rate W is fixed during each deposition, the third constraint can be removed by substituting the actual value of ς^2 into Eq.4.38.

To solve the above optimization problem, our initial step is to reduce it to a quadratic programming problem with only linear constraints. To do this, we remove the second and fourth constraints (Egs.4.39 and 4.41) by first finding the optimal c_2 that minimizes J and then computing the corresponding optimal T using the equality constraint of Eq.4.39. In addition, we linearize the first constraint Eq.4.38 with respect to c_2 around an initial guess $\tilde{c}_2$ (we note that when $\tilde{c}_2$ is chosen close enough to the optimal c_2, the solution of the linearized problem should be close the solution of the original problem). The value of $\tilde{c}_2$ is computed based on the substrate temperature currently been used in Eq.4.39 (at $t = 0$, the $\tilde{c}_2$ is computed based on the initial substrate temperature). Therefore, the original optimization problem is reduced to:

$$\min_{c_2} J = (r_{set}^2 - \langle r_{final} \rangle^2)^2 \tag{4.42}$$

subject to

$$\langle r_{final}\rangle^2 = \langle r_{final}(\tilde{c}_2)\rangle^2 + (c_2 - \tilde{c}_2)\frac{\partial\langle r_{final}(\tilde{c}_2)\rangle^2}{\partial\tilde{c}_2} \tag{4.43}$$

$$c_{2,min} \leq c_2 \leq c_{2,max} \tag{4.44}$$

where $c_{2,min}$ and $c_{2,max}$ are the lower bound and upper bound of c_2 respectively. The second constraint is added due to the fact that c_2 can only take values within the corresponding range specified by Eqs.4.39 and 4.41, and $c_{2,min}$ and $c_{2,max}$ are determined as follows:

$$\begin{aligned} c_{2,min} &= \frac{e^{-32.002 + 0.0511 T_{min} - 0.1620 W}}{k_{max}^2} \\ c_{2,max} &= \frac{e^{-32.002 + 0.0511 T_{max} - 0.1620 W}}{k_{max}^2} \end{aligned} \tag{4.45}$$

A standard procedure based on the active set method [28] is used to solve the optimization problem of Eq.4.42. First, we drop the inequality constraint Eq.4.44, and a direct computation of the above problem by substituting the equality constraint into the objective function yields:

$$\bar{c}_2 = \tilde{c}_2 + \frac{r_{set}^2 - \langle r_{final}(\tilde{c}_2)\rangle^2}{\frac{\partial\langle r_{final}(\tilde{c}_2)\rangle^2}{\partial\tilde{c}_2}} \tag{4.46}$$

where $\bar{c}_2$ is the optimal value of c_2 without the inequality constraint Eq.4.44. Then, we check whether the inequality constraint is violated by $\bar{c}_2$, if the inequality constraint is inactive (i.e., the constraint is not violated), $\bar{c}_2$ is considered to be the optimal value for the linearized optimization problem. On the other hand, if the inequality constraint is active (i.e., the constraint is violated), the optimization problem is resolved accounting for the active constraint (which serves as another equality constraint). In such case, c_2 can only take the value of $c_{2,min}$ (when the lower bound is violated by $\bar{c}_2$) or $c_{2,max}$ (when the upper bound is violated by $\bar{c}_2$), hence, the optimal value is just the only feasible value $c_{2,min}$ or $c_{2,max}$.

However, since Eq.4.43 is the linearization of Eq.4.38, $\bar{c}_2$ might only be a suboptimal value for the original problem. To this end, we can use this suboptimal $\bar{c}_2$ as a new guess and repeat the linearzation procedure until $\bar{c}_2$ converges to the optimal value (the convergence is guaranteed if the original problem is convex), but for the sake of simplicity, such iterative procedure is not adopted in this work. Once the optimal c_2 is determined, by substituting c_2 into Eq.4.39, the optimal T can be obtained and used as the output of the controller.

Remark 4.3 *Since Eq.4.38, is in fact, a finite approximation of the predicted final surface roughness, to achieve a control precision ϵ, m should be chosen large enough for each optimization computation so that the approximation error is less than ϵ (see the Section 4.4.1 for detailed discussion). However, to achieve the same control precision, the minimum m needed may vary depending on the specific surface configuration (i.e., current states z_n). On one hand, when the length scale of the surface fluctuation is very small, the magnitude of the high-order states becomes significant, hence, m need to be relatively large so that these high-order states are included in the calculation. On the other hand, when the length scale of the surface fluctuation is relatively large, the contribution from the high-order states becomes negligible compared to the low-order states, hence, a relatively small m should be good enough for precise calculation. Therefore, in our implementation, the desired control precision is achieved by adding more states to the finite-dimensional system until the approximation error (computed based on Eq.4.36) is small enough (we note that the approximation error depends on the actual values of the states as shown in Eq.4.36), rather than by specifying the number of states that should be evaluated from the surface snapshot before hand. However, a limit on the maximum number of states to be used is imposed to guarantee that the computation time of the controller does not prevent real-time implementation (control precision may be reduced as a trade off against the computation time).*

Remark 4.4 *Since the control action is computed using closed-form equations (Eqs.4.46 and 4.39), the computation cost is proportional to the number of states used* m *but independent of the optimization horizon* $t_{dep} - t$*; however, to evaluate the values of the* m *states that are used in Eq.4.46, an additional computation time on the order of* $k_{max}m$ *is needed for each surface measurement. Nevertheless, even for a lattice size that corresponds to the largest physical dimension of the sampling area that can be achieved by common surface measurement techniques (i.e., a few microns), such computation can still be completed with seconds using currently available computing power. On the other hand, such task is almost impossible to achieve using a kMC code, whose computation cost is on the order of* $k_{max}^2(t_{dep} - t)$ *for merely a single run. Furthermore, we note that the evaluation of each state is independent of other states, and therefore, can be executed in parallel, while the kMC code, being a serial calculation, is unsuitable for parallel processing.*

4.4.3 Closed-loop simulation

A kMC code with a lattice size $k_{max} = 1000$ is used to simulate the thin film deposition process, and the substrate temperature is restricted within 300 K to 900 K. The measurement interval, as well as the control interval, is set to be 1 s. We limit the maximum number of states to be used (in our case, to $m = 500$) to guarantee the maximum possible computation time for each control action is within certain requirement, however, for most of the time the number of states needed by the controller is much smaller.

Fig.5.12 shows the surface roughness and substrate temperature profiles of a closed-loop deposition process with thin film growth rate $W = 0.5\ ML/s$ and of an open-loop deposition with the same growth rate and a fixed substrate temperature $T = 650\ K$. The control objective is to drive the final surface roughness of the thin film to 1.0 ML (monolayers) at the end of the 1000 s deposition. It can be

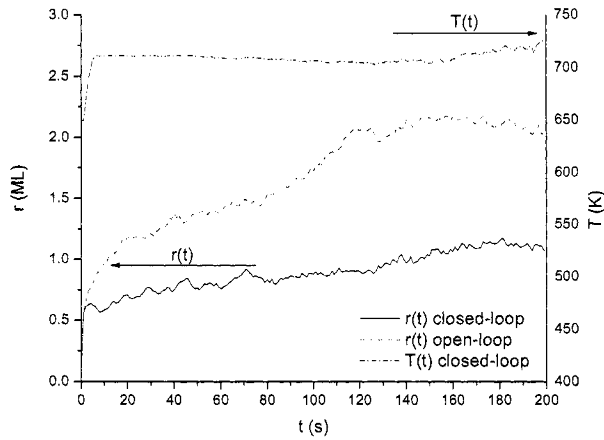

Figure 4.15: Surface roughness and substrate temperature profiles of a 1000 s closed-loop deposition process with thin film growth rate $W = 0.5$ ML/s and final roughness setpoint $r_{set} = 1.0$ ML.

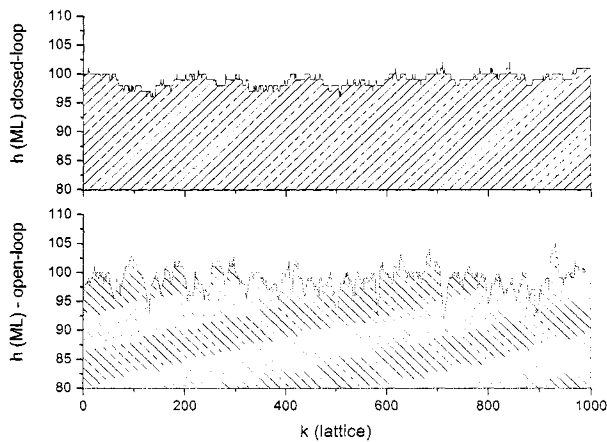

Figure 4.16: Final thin film surface profile of a closed-loop and a open-loop depositions with the same initial substrate temperature $T = 650$ K, thin film growth rate $W = 0.5$ ML/s and deposition length $t_{dep} = 1000$ s.

seen that the final surface roughness is controlled at the desired level while an open-loop deposition with the same initial deposition condition would lead to a 100% higher final surface roughness as shown in Fig.5.12 (a comparison between the surfaces of the thin films deposited with closed-loop and open-loop deposition is shown in Fig.5.13).

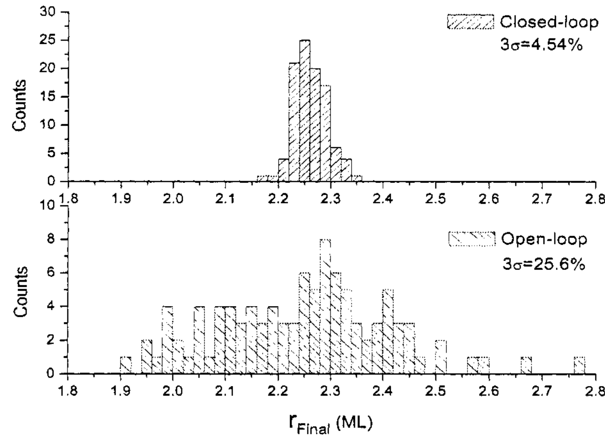

Figure 4.17: Histogram of final surface roughness of 100 closed-loop and 100 open-loop thin film depositions targeted at the same surface roughness level.

Fig.5.14 shows the final surface roughness histogram of the thin films deposited using 100 different closed-loop depositions with final surface roughness setpoint of 2.25 ML and 100 different open-loop depositions. It can be seen that the average surface roughness of the thin films deposited by the open-loop depositions is very close to the average surface roughness of the thin films deposited by the closed-loop deposition and the well-designed recipe-based open-loop depositions, however, the variance among the thin films from different open-loop deposition runs is over 400% higher than that of closed-loop deposition runs even though no process disturbance is considered in the simulations. This is due to the fact that the stochastic nature of the microscopic processes of the film growth cannot

be handled effectively without having a real-time feedback controller that can compensate for the stochastic deviation from the expectation. As a result, if the tolerance on the thin film surface roughness to fabricate a certain device is ± 0.1 ML, over half of the thin films prepared by the recipe-based deposition would be disqualified. Therefore, introducing real-time feedback control system that directly aiming at the material and electrical properties of the thin films is one of the most effective, if not the only, solution to reduce cost and meet the ever increasing film quality requirements demanded by the devices which are already down to the nanometer regime.

To study the robustness of the closed-loop deposition with respect to process disturbance, open-loop and closed-loop depositions are simulated in which same process disturbance are introduced during all depositions. Particularly, for the 200 s deposition, a step change in the adsorption rate is introduced at $t = 80$ s, and W is change from 0.5 ML to 1.5 ML; the adsorption rate W remains at 1.5 ML for 20 s and then drop back to 0.5 ML immediately (such square-wave changes in the adsorption rate may be caused by the spikes in the gas delivery system of the CVD reactor). The roughness set-point of the roughness controller is 1.3 ML, and the substrate temperature of all the open-loop depositions is kept constant at 700 K so that the expected final roughness of the deposited films would be 1.3 ML if no disturbance is present.

Fig. 4.18 shows the typical surface roughness profile of the undisturbed open-loop deposition (dotted green line), and the surface roughness profile of the process under disturbance, of the open-loop deposition (dashed red line) and closed-loop deposition (solid black line). Fig. 4.19 shows the profiles of the disturbance variable W (it is not used to compute the control action, i.e., the roughness controller

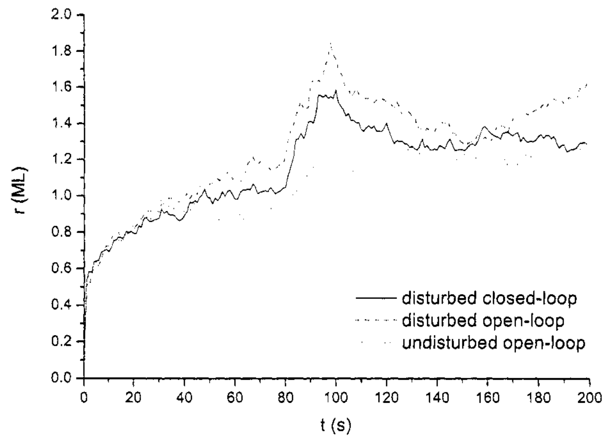

Figure 4.18: Surface roughness profile of the undisturbed open-loop deposition (dotted green line), and the surface roughness profile of the process under disturbance, of the open-loop deposition (dashed red line) and closed-loop deposition (solid black line).

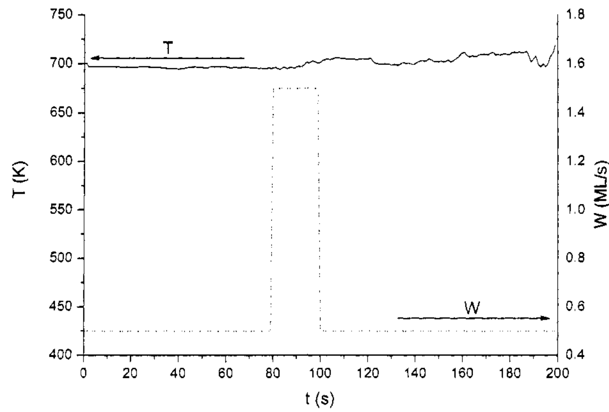

Figure 4.19: Profiles of the process disturbance W, and the manipulated substrate temperature T (in closed-loop deposition).

is unaware of the abnormal adsorption rate) and the manipulated substrate temperature T (in closed-loop deposition). It can be seen that when disturbance is introduced, the final surface roughness of the film deposited with open-loop operation is much higher than the desired level (in this case more than 20 %), while the final surface roughness of the film deposited under feedback control is still kept at the desired level (i.e., the controller is able to bring the final surface roughness down to the desired level after the disturbance when the thin film surface is unexpectedly roughened).

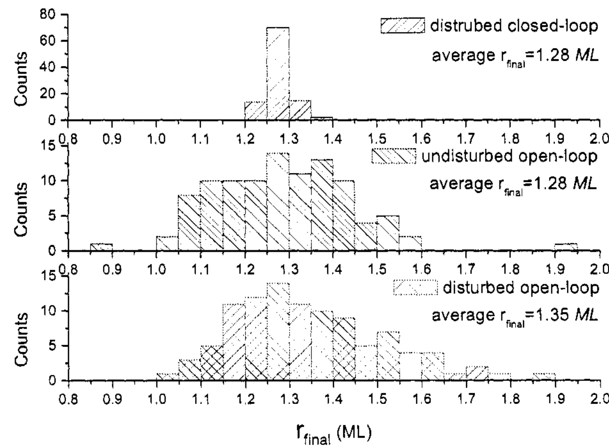

Figure 4 20: Histograms of final surface roughness of thin films deposited with open-loop (with and without process disturbance) and closed-loop (with process disturbance) operations.

Fig.5.14 shows the histograms of the final surface roughness of thin films deposited with open-loop (with and without process disturbance) and closed-loop (with process disturbance) operations, and each histogram include 100 different simulation runs. It can be seen that the average surface roughness of the thin films deposited by the open-loop depositions is shifted up for more than 5% with the presence of process disturbance. Despite of that, the average surface roughness of

the thin films deposited under feedback control is very close to the desired level even with the presence of process disturbance, and the variance is reduced as it is in the previous case where no disturbance is introduced.

4.5 Conclusions

In this chapter, we have developed a systematic method for the construction of linear stochastic PDE models for feedback control of surface roughness in thin film deposition. A linear stochastic PDE model has been constructed for a generic thin film deposition process and has been used to design a real-time feedback controller to control the thin film surface roughness. We have initially reformulated a general linear stochastic PDE into a system of infinite stochastic ordinary differential equations (ODE) by using modal decomposition and have derived the analytical expressions of the first and second statistical moments of the ODE states. We have used a kMC code to generate surface snapshots for different instants during process evolution to obtain values of the state vector of the stochastic ODE system. The eigenvalues and the covariance of the stochastic ODE system that correspond to the deposition process have been computed based on the kMC simulation results. Finally, a linear stochastic PDE model has been determined by least-square fitting the pre-derivative coefficients to match the spectrum of the stochastic PDE system to the identified spectrum of the stochastic ODE system. The dependence of the model parameters of the stochastic PDE on the process parameters has been investigated and the least-square-optimal form of the stochastic PDE model with model parameters expressed as functions of the process parameters has been determined. Furthermore, an optimization-based feedback controller has been designed using the constructed stochastic PDE model and

has been applied to the kMC simulation of the deposition process to control the surface roughness. Closed-loop system simulation results have demonstrated that the model is adequately accurate and that the controller is capable of controlling the surface roughness of the thin film.

Chapter 5

Multivariable Predictive Control of Thin Film Deposition Using a Stochastic PDE Model

5.1 Introduction

Stochastic PDE models, as discussed in the previous chapter, are closed-form models that could be used to describe the evolution of the height profile for surfaces in many physical and chemical processes. In Chapter 4, a systematic method to construct stochastic PDE models for thin film growth using first principles-based microscopic simulations has been presented, and the method has been applied to a representative one-dimensional thin film growth process. In addition, we have also demonstrate the use of such stochastic PDE models in feedback control by the development of an univariable optimization-based feedback controller that regulates the film surface roughness. Furthermore, Lou and Christofides also presented elsewhere a method to design pole-placement controllers directly based on the stochastic PDE models, and the feedback controller was successfully applied

to the kMC model of the process regulating the surface roughness to desired values in deposition [44] and sputtering [42] processes.

In this chapter, we focus on a thin film deposition process which takes place on a 2D lattice and is governed by three microscopic processes including molecule adsorption, surface migration and desorption. A 2D linear stochastic PDE model is initially constructed, following the methodology proposed in Chapter 4, which describes the spatio-temporal evolution of the film surface. Then, the control problem is formulated as the one of regulating the thin film thickness and surface roughness by manipulating the substrate temperature and adsorption rate. Subsequently, a computationally-efficient multivariable predictive control algorithm is developed which uses a finite-dimensional approximation of the stochastic PDE model to regulate the thin film thickness and surface roughness at desired levels at the end of the deposition. The predictive controller is then applied to the kMC simulation of the deposition process. Closed-loop system simulation results demonstrate that the model is adequately accurate and that the controller is effective in enforcing the desired control objectives and reducing film variance.

5.2 Preliminaries

5.2.1 Thin film growth process

In this chapter, we consider a thin film growth process of deposition from vapor phase, in which, the formation of the thin film is governed by three microscopic processes that occur on the surface as shown in Fig.5.1, i.e., the adsorption of vapor phase molecules on the surface, the migration of surface molecules and the desorption of surface molecules. This process is, in fact, a very common thin film growth process that can be traced in most chemical vapor deposition processes.

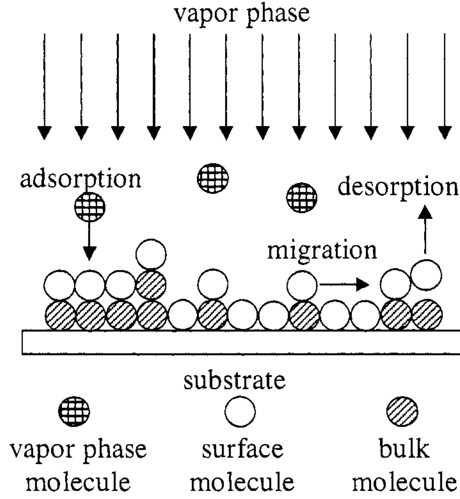

Figure 5.1: The thin film growth process.

More specifically, we consider a single species growth on a 2D lattice. The adsorption rate which depends on the vapor phase concentration is considered uniform over the spatial domain. All surface sites are available for adsorption for all time and the adsorption rate for each surface site is denoted as W (expressed in number of molecules adsorbed per second, $1/s$).

The migration rate of each surface molecule depends on its local environment. Under the consideration of only first nearest-neighbor interactions, the migration rate of surface molecules from a surface site with n first nearest-neighbors is given by:

$$w_m(n) = k_{m0} e^{-\frac{E_s + nE_n}{k_B T}} \tag{5.1}$$

where E_s is the energy barrier associated with migration due to surface effects, E_n is the energy barrier associated with migration due to nearest-neighbor interactions, k_{m0} is the frequency constant associated with migration, k_B is the Boltzmann's constant and T is the substrate temperature. The values of migration energy barriers and frequency constant used in this study are taken from

the literature [62] for a molecular beam epitaxy $GaAs$ process and are as follows: $E_s = 1.58\ eV$, $E_n = 0.28\ eV$ and $k_{m0} = 2k_BT/h$, where h is the Planck's constant.

The desorption rate of each surface molecule also depends on its local environment. Under the consideration of only first nearest-neighbor interactions, the desorption rate of surface molecules from a surface site with n first nearest-neighbors is given by:

$$w_d(n) = k_{d0} e^{-\dfrac{E_d + nE_n}{k_BT}} \tag{5.2}$$

where E_d is the energy barrier associated with desorption due to surface binding, and k_{d0} is the frequency constant associated with desorption. We use the values $E_d = 1.8\ eV$ and $k_{d0} = 2k_BT/h$ in this chapter.

A kinetic Monte-Carlo simulation code following the algorithm reported in [70] is used to simulate the deposition process and obtain surface snapshots. First, the surface molecules are grouped into three classes based on the number of first nearest neighbors (from 0 to 4 neighbors); in each class, the molecules have the same migration rate and desorption rate, and the adsorption rate is site independent. Then, a random number is generated to select an event to be executed based on the rates; if the event is migration or desorption, the class in which the event will occur is also selected. After that, a second random number is generated to select the site where the event will be executed; if the event is adsorption, the site is randomly picked among all the sites in the entire lattice; if the event is migration or desorption, the site is randomly picked from the list of the sites in the selected class. After the site is selected, the Monte-Carlo event is executed. If the event is adsorption, it is executed by adding one molecule on the selected site; if the event is migration, the molecule on the site is moved to one of the vacant neighboring sites with equal probability; if the event is desorption, it is executed by removing

the top molecule on the selected site. Upon an executed event, a time increment τ is added to the process time t, computed based on the following equation (see [29] for a detailed proof):

$$\tau = -\frac{\ln \zeta}{W k_{max}^2 + \sum_{n=0}^{4} N_n [w_m(n) + w_d(n)]} \quad (5.3)$$

where ζ is a random number that follows the uniform distribution in the unit interval, N_n is the number of surface molecules with n first nearest neighbors and k_{max} is the size of the simulation lattice (i.e., the total number of surface sites is k_{max}^2). Furthermore, periodic boundary conditions are used in the kMC simulation to satisfy the mass balance of the migration of the surface molecules.

5.2.2 Stochastic PDE model

We now proceed with constructing a closed-form stochastic PDE model using the approach we developed in [50]. Without any *a priori* knowledge of the deposition process, we assume that there exists a 2D linear stochastic PDE of the following general form that can adequately describe the evolution of the surface of the thin film during the deposition:

$$\frac{\partial h}{\partial t} = c + c_1 \bigtriangledown h + c_2 \bigtriangledown^2 h + \cdots + c_w \bigtriangledown^w h + \xi(x, y, t) \quad (5.4)$$

where $x \in [0, \pi], y \in [0, \pi]$ is the spatial coordinate, t is the time, $h(x, y, t)$ is the height (in the unit of *monolayers*) of the surface at position x, y and time t, and $\xi(x, y, t)$ is a Gaussian noise with zero mean and covariance:

$$\langle \xi(x, y, t) \xi(x', y', t') \rangle = \varsigma^2 \delta(x - x') \delta(y - y') \delta(t - t') \quad (5.5)$$

where $\delta(\cdot)$ is the Dirac function. Furthermore, the pre-derivative coefficients c and c_j in Eq.5.4 and the parameter ς^2 in Eq.5.5 depend on the process parameters, the

substrate temperature T and adsorption rate W (directly determined by vapor phase concentration):

$$\begin{array}{rcl} c & = & C[T(t), W(t)] \\ \varsigma^2 & = & C_\xi[T(t), W(t)] \\ c_j & = & C_j[T(t), W(t)] \quad j = 0, \cdots, w \end{array} \tag{5.6}$$

where $C(\cdot)$ and $C_j(\cdot)$ are nonlinear functions to be determined.

The stochastic PDE of Eq.5.4 is subjected to the following periodic boundary conditions:

$$\begin{array}{l} \nabla^j h(0, y, t) = \nabla^j h(\pi, y, t) \\ \nabla^j h(x, 0, t) = \nabla^j h(x, \pi, t) \quad j = 0, \cdots, w-1 \end{array} \tag{5.7}$$

and the initial condition:

$$h(x, y, 0) = h_0(x, y) \tag{5.8}$$

Remark 5.1 *In this chapter, we assume that a linear stochastic PDE model should adequately describe the process dynamics, however, for the cases in which the nonlinear dynamics are significant, nonlinear stochastic PDE models would be needed. Also, we note that we use a scalar function, $h(\cdot)$, to represent the height profile of the thin film surface in the model. In general, $h(\cdot)$ can be a vector function and be used to represent any appropriate microscopic description of the thin film (such as the defect locations, grain boundaries, etc), in such a case, several stochastic PDEs should be considered simultaneously.*

To study the dynamics of Eq.5.4, we initially consider the eigenvalue problem of the linear operator of Eq.5.4, which takes the form:

$$\begin{array}{rcl} A\phi_{m,n}(x, y) & = & c_1 \nabla \phi_{m,n}(x, y) + c_2 \nabla^2 \phi_{m,n}(x, y) + \cdots + c_w \nabla^w \phi_{m,n}(x, y) \\ & = & \lambda_{m,n}\phi_{m,n}(x, y) \\ \nabla^j \phi_{m,n}(0, y) & = & \nabla^j \phi_{m,n}(\pi, y) \\ \nabla^j \phi_{m,n}(x, 0) & = & \nabla^j \phi_{m,n}(x, \pi) \quad j = 0, \cdots, w-1 \quad m, n = 0, \pm 1, \cdots, \pm\infty \end{array} \tag{5.9}$$

where $\lambda_{m,n}$ denotes the eigenvalue and $\phi_{m,n}$ denotes the eigenfunction. A direct

computation of the solution of the above eigenvalue problem yields:

$$\begin{aligned}
\lambda_{m,n} &= (I2m + I2n)c_1 + [(I2m)^2 + (I2n)^2]c_2 + \cdots + [(I2m)^w + (I2n)^w]c_w \\
\phi_{m,n}(x,y) &= \frac{1}{\pi}(e^{I2mx + I2ny}) \quad m,n = 0,\pm 1,\cdots,\pm\infty
\end{aligned} \tag{5.10}$$

where $\lambda_{m,n}$ denotes the (m,n)th eigenvalue, $\phi_{m,n}(x,y)$ denotes the (m,n)th eigenfunction and $I = \sqrt{-1}$.

To present the method that we use for parameter identification of the stochastic PDE of Eq.5.4, we first derive an infinite stochastic ODE representation of Eq.5.4 using modal decomposition and parameterize the infinite stochastic ODE system using kMC simulation. We first expand the solution of Eq.5.4 in an infinite series in terms of the eigenfunctions of the operator of Eq.5.9 as follows (i.e., the Fourier expansion in the complex form):

$$h(x,y,t) = \sum_{m,n=-\infty}^{\infty} z_{m,n}(t)\phi_{m,n}(x,y) \tag{5.11}$$

where $z_{m,n}(t)$ are time-varying coefficients. Substituting the above expansion for the solution, $h(x,y,t)$, into Eq.5.4 and taking the inner product, the following system of infinite stochastic ODEs is obtained:

$$\frac{dz_{m,n}}{dt} = \lambda_{m,n} z_{m,n} + c^z_{m,n} + \xi_{m,n}(t) \quad m,n = 0,\pm 1,\cdots,\pm\infty \tag{5.12}$$

and the initial conditions:

$$z_{m,n}(0) = z_{m,n,0} \quad m,n = 0,\pm 1,\ldots,\pm\infty \tag{5.13}$$

where $c^z_{m,n} = c\int_0^{\pi}\int_0^{\pi} \phi^*_{m,n}(x,y)dxdy$, $\xi_{m,n}(t) = \int_0^{\pi}\int_0^{\pi} \xi(x,y,t)\phi^*_{m,n}(x,y)dxdy$ and $z_{m,n,0} = \int_0^{\pi}\int_0^{\pi} h_0(x,y)\phi^*_{m,n}(x,y)dxdy$. Apparently, $c^z_{0,0} = \pi c$ and $c^z_{m,n} = 0$ when $m^2 + n^2 \neq 0$. $\phi^*_{m,n}$ is the complex conjugate of $\phi_{m,n}$, the superscript star is used to denote complex conjugate in the remainder of this manuscript.

The covariance of $\xi_{m,n}(t)$ can be computed by using the following result [5]:

Result 5.1 *If (1) f(x) is a deterministic function, (2) $\eta(x)$ is a random variable with $\langle \eta(x) \rangle = 0$ and covariance $\langle \eta(x)\eta^*(x') \rangle = \sigma^2 \delta(x - x')$, and (3) $\epsilon = \int_a^b f(x)\eta(x)dx$, then ϵ is a random number with $\langle \epsilon \rangle = 0$ and covariance $\langle \epsilon\epsilon^* \rangle = \sigma^2 \int_a^b f(x)f^*(x)dx$.*

Using Result 5.1, we obtain $\langle \xi_{m,n}(t) \rangle = 0$ and $\langle \xi_{m,n}(t)\xi^*_{m,n}(t') \rangle = \varsigma^2 \delta(t - t')$. We note that $\xi_{m,n}(t)$ is a complex Gaussian random variable.

To parameterize this infinite stochastic ODE system, we first derive the analytic expressions for the statistical moments of the stochastic ODE states, such as the expected values and covariances. By comparing the analytical expression to the statistical moments obtained by multiple kMC simulations, the parameters of the stochastic ODE system (i.e., $\lambda_{m,n}$ and ς) can be determined.

The analytic solution to Eq.5.12 is obtained as follows to derive the expressions for the statistical moments of the stochastic ODE states:

$$z_{m,n}(t) = e^{\lambda_{m,n} t} z_{m,n,0} + \frac{(e^{\lambda_{m,n} t} - 1)c^z_{m,n}}{\lambda_{m,n}} + \int_0^t e^{\lambda_{m,n}(t - \mu)} \xi_{m,n}(\mu) d\mu \quad (5.14)$$

Using Result 5.1, Eq.5.14 can be further simplified as follows:

$$z_{m,n}(t) = e^{\lambda_{m,n} t} z_{m,n,0} + \frac{(e^{\lambda_{m,n} t} - 1)c^z_{m,n}}{\lambda_{m,n}} + \theta_{m,n}(t) \quad (5.15)$$

where $\theta_{m,n}(t)$ is a complex random variable of normal distribution with zero mean and covariance $\langle \theta_{m,n}(t)\theta^*_{m,n}(t) \rangle = \varsigma^2 \frac{e^{(\lambda_{m,n} + \lambda^*_{m,n})t} - 1}{\lambda_{m,n} + \lambda^*_{m,n}}$. Therefore, the first stochastic moment (the expected value) and the second stochastic moment (the covariance) of state $z_{m,n}$ can be expressed as follows:

$$\begin{aligned} \langle z_{m,n}(t) \rangle &= e^{\lambda_{m,n} t} z_{m,n,0} + \frac{(e^{\lambda_{m,n} t} - 1)c^z_{m,n}}{\lambda_{m,n}} \\ \langle z_{m,n}(t) z^*_{m,n}(t) \rangle &= \varsigma^2 \frac{e^{(\lambda_{m,n} + \lambda^*_{m,n})t} - 1}{\lambda_{m,n} + \lambda^*_{m,n}} + \langle z_{m,n}(t) \rangle \langle z_{m,n}(t) \rangle^* \end{aligned} \quad (5.16)$$

Remark 5.2 *We note that Eqs.5.14, 5.15 and 5.16 hold for all stochastic ODE states. Particularly, when $m = n = 0$ (i.e., for state $z_{0,0}$), $\lambda_{m,n} = 0$, these terms in the equations with $\lambda_{m,n}$ and $\lambda_{m,n} + \lambda^*_{m,n}$ as denominators should be calculated as follows:*

$$\lim_{\lambda_{m,n} \to 0} \frac{(e^{\lambda_{m,n} t} - 1) c^z_{m,n}}{\lambda_{m,n}} = t c^z_{m,n}$$

$$\lim_{\lambda_{m,n} \to 0} \varsigma^2 \frac{e^{(\lambda_{m,n} + \lambda^*_{m,n})t} - 1}{\lambda_{m,n} + \lambda^*_{m,n}} = \varsigma^2 t$$

Eq.5.16 holds for any initial condition $z_{m,n,0}$. Since we are able to choose any initial thin film surface profile for simulation, we choose $z_{m,n,0} = 0$ (i.e., the initial surface is flat, $h(x, y, 0) = 0$) to simplify our calculations. In this case, Eq.5.16 can be further simplified as follows (note that $c^z_{m,n} = 0, \forall m^2 + n^2 \neq 0$):

$$\begin{aligned} &\langle z_{m,n}(t) \rangle = 0 \\ &\langle z_{m,n}(t) z^*_{m,n}(t) \rangle = \varsigma^2 \frac{e^{(\lambda_{m,n} + \lambda^*_{m,n})t} - 1}{\lambda_{m,n} + \lambda^*_{m,n}} = \varsigma^2 \frac{e^{2Re(\lambda_{m,n})t} - 1}{2Re(\lambda_{m,n})} \\ &m, n = 0, \pm 1, \cdots, \pm\infty; \quad m^2 + n^2 \neq 0 \end{aligned} \tag{5.17}$$

where $Re(\lambda_{m,n})$ denotes the real part of $\lambda_{m,n}$. For $z_{0,0}(t)$, it follows from Eq.5.16 with $\lambda_{0,0} = 0$ that

$$\begin{aligned} \langle z_{0,0}(t) \rangle &= t\pi c \\ \langle z^2_{0,0}(t) \rangle &= \varsigma^2 t + t^2 \pi^2 c^2 \end{aligned} \tag{5.18}$$

It can be seen in Eq.5.17 that the statistical moments of each stochastic ODE state depend only on the real part of the corresponding eigenvalue, and therefore, to determine the imaginary part of the eigenvalue we need to construct an extra equation. We note that $\lambda_{m,n}$ would be a complex number if the linear operator A is not self-adjoint, for example, when odd-partial-derivatives are present in the stochastic PDE (see Eq.5.10).

Therefore, we rewrite Eq.5.14 by separating the real part and the imaginary

part of $z_{m,n}(t)$ as follows with initial condition $z_{m,n,0} = 0$:

$$\begin{aligned} z_{m,n}(t) &= \frac{1}{2}\int_0^t [e^{\lambda_{m,n}(t-\mu)} + e^{\lambda^*_{m,n}(t-\mu)}]\xi_{m,n}(\mu)d\mu \\ &+\frac{1}{2}\int_0^t [e^{\lambda_{m,n}(t-\mu)} - e^{\lambda^*_{m,n}(t-\mu)}]\xi_{m,n}(\mu)d\mu \\ & m,n = 0, \pm 1, \cdots, \pm\infty; \quad m^2+n^2 \neq 0 \end{aligned} \tag{5.19}$$

Accordingly, the real part of $z_{m,n}(t)$ can be expressed as follows:

$$\begin{aligned} &Re[z_{m,n}(t)] = \frac{1}{2}\int_0^t [e^{\lambda_{m,n}(t-\mu)} + e^{\lambda^*_{m,n}(t-\mu)}]\xi_{m,n}(\mu)d\mu \\ &m,n = 0, \pm 1, \cdots, \pm\infty; \quad m^2+n^2 \neq 0 \end{aligned} \tag{5.20}$$

where $Re[z_{m,n}(t)]$ denotes the real part of $z_{m,n}(t)$. By using Result 5.1 we have,

$$\begin{aligned} \langle Re[z_{m,n}(t)]\rangle &= 0 \\ \langle Re[z_{m,n}(t)]^2\rangle &= \varsigma^2 \left[\frac{\lambda^*_{m,n}e^{2\lambda_{m,n}t} + \lambda_{m,n}e^{2\lambda^*_{m,n}t} - (\lambda_{m,n}+\lambda^*_{m,n})}{8\lambda_{m,n}\lambda^*_{m,n}} \right. \\ &\left. + \frac{e^{(\lambda_{m,n}+\lambda^*_{m,n})t} - 1}{2(\lambda_{m,n}+\lambda^*_{m,n})}\right] \\ &= \varsigma^2 \left\{ \frac{Re(\lambda_{m,n})e^{2Re(\lambda_{m,n})}cos(2Im(\lambda_{m,n})t)}{4[Re(\lambda_{m,n})^2 + Im(\lambda_{m,n})^2]} \right. \\ &+ \frac{Im(\lambda_{m,n})e^{2Re(\lambda_{m,n})}sin(2Im(\lambda_{m,n})t)}{4[Re(\lambda_{m,n})^2 + Im(\lambda_{m,n})^2]} \\ &\left. - \frac{Re(\lambda_{m,n})}{4[Re(\lambda_{m,n})^2 + Im(\lambda_{m,n})^2]} + \frac{e^{2Re(\lambda_{m,n})t} - 1}{4Re(\lambda_{m,n})} \right\} \\ & m,n = 0, \pm 1, \cdots, \pm\infty; \quad m^2+n^2 \neq 0 \end{aligned} \tag{5.21}$$

where $Im(\lambda_{m,n})$ denotes the imaginary part of $\lambda_{m,n}$. Thus, we can use Eq.5.17 to first determine the real part of the eigenvalue, and then use the Eq.5.21 to determine its imaginary part. We note that we can determine both parts of the eigenvalue using only Eq.5.21, however, in that case, the nonlinear least-square problem involved in the eigenvalue determination would be much more difficult to solve.

Remark 5.3 *Eq.5.17, Eq.5.18 and Eq.5.21 show the analytical relation that relates the linear operator and the Gaussian noise in Eq.5.4 to the statistical moments of the states of Eq.5.12 which can be obtained through multiple experimental measurements or first-principle simulations, and therefore, reveal a viable path to systematically construct a linear stochastic PDE of the form of Eq.5.4 that describes the dynamics of a microscopic process directly from experimental or simulation data.*

5.3 Model construction

Following the procedure we proposed in our previous chapter, we construct a linear stochastic PDE for the deposition process described in Section 5.2.1. The procedure includes the following steps: First, we design a set of simulation experiments that cover the complete range of process operation; second, we run multiple simulations for each simulation experiment to obtain the trajectories of the first and second statistical moments of the states (i.e., Fourier coefficients) computed from the surface snapshots; third, we compute the eigenvalues of the linear operator and covariance of the Gaussian noise based on the trajectories of the statistical moments of the states for each simulation experiment, and determine the model parameters of the stochastic PDE (i.e., the pre-derivative coefficients and the order of the stochastic PDE); finally, we investigate the dependence of the model parameters of the stochastic PDE on the process parameters and determine the least-square-optimal form of the stochastic PDE model with model parameters expressed as functions of the process parameters.

Remark 5.4 *We note that all the simulation experiments are executed using simulation lattices whose sizes are large enough to capture the dynamics of the surface evolution during the thin film growth, and we run additional simulation experi-*

ments using larger lattices to assure our results. As we have mentioned in [50], the experimental measurements obtained from the actual physical process can also be used for model construction, as long as the measurement has enough resolution to capture the surface evolution dynamics. Furthermore, since the same dynamics can be present at both large and small length scale, the resolution of the constructed model could be even better than the experimental measurements. In general, the use of a finite lattice size simulation and limited resolution measurements does not affect the accuracy of the constructed model, provided that the surface evolution dynamics are retained in the simulation/experimental data.

5.3.1 Eigenvalues and covariance

The eigenvalues and the covariance of the systems of ODEs which correspond to the deposition processes with different W and T values are identified based on the trajectories of the statistical moments. In the previous section we have shown that for a deposition process with a flat initial surface, the trajectory of the second statistical moment of the ODE state $\langle z_{m,n}(t) z^*_{m,n}(t) \rangle$ can be predicted by Eq.5.17, therefore, we can fit ς^2 and $Re(\lambda_{m,n})$ in Eq.5.17 for the profile of $\langle z_{m,n}(t) z^*_{m,n}(t) \rangle$. Similarly, $Im(\lambda_{m,n})$ can be determined based on the trajectory of $\langle Re[z_{m,n}(t)]^2 \rangle$ and Eq.5.21.

In order to obtain the profile of $\langle z_{m,n}(t) z^*_{m,n}(t) \rangle$ and $\langle Re[z_{m,n}(t)]^2 \rangle$, we need to generate snapshots of the thin film surface during each deposition simulation and compute the values of $z_{m,n}(t)$. Since the lattice consists of discrete sites, we let $h(k_x L, k_y L, t)$ be the height profile of the surface at time t with lattice constant L (k_x and k_y denote the coordinates of a specific surface site), and compute $z_{m,n}(t)$

as follows:

$$\begin{aligned} z_{m,n}(t) &= \int_0^\pi \int_0^\pi h(x,y,t)\phi^*_{m,n}(x,y)dxdy \\ &= \sum_{k_x,k_y=0}^{k_{max}} h(k_xL,k_yL,t)\int_{k_xL}^{(k_x+1)L}\int_{k_yL}^{(k_y+1)L} \phi^*_{m,n}(x,y)dxdy \end{aligned} \tag{5.22}$$

where $k_{max}L = \pi$ (i.e., the lattice is mapped to the domain $[0,\pi]^2$). Substituting Eq.5.10 into Eq.5.22, we can derive the following expression for $z_{m,n}(t)$, $z_{0,n}(t)$, $z_{m,0}(t)$ and $z_{0,0}(t)$:

$$\begin{aligned} z_{m,n}(t) &= \sum_{k_x,k_y=0}^{k_{max}} \frac{h(k_xL,k_yL,t)}{-4\pi mn} e^{-(I2mk_xL + I2nk_yL)} \\ &\quad \times (e^{-I2mL} - 1)(e^{-I2nL} - 1) \\ &\quad m,n = \pm 1, \cdots, \pm\infty \end{aligned} \tag{5.23}$$

$$\begin{aligned} z_{0,n}(t) &= \sum_{k_x,k_y=0}^{k_{max}} \frac{h(k_xL,k_yL,t)Le^{-I2k_yLn}}{-I2\pi n}(e^{-I2Ln} - 1) \\ &\quad n = \pm 1, \cdots, \pm\infty \end{aligned} \tag{5.24}$$

$$\begin{aligned} z_{m,0}(t) &= \sum_{k_x,k_y=0}^{k_{max}} \frac{h(k_xL,k_yL,t)Le^{-I2k_xLm}}{-I2\pi m}(e^{-I2Lm} - 1) \\ &\quad m = \pm 1, \cdots, \pm\infty \end{aligned} \tag{5.25}$$

$$z_{0,0}(t) = \sum_{k_x,k_y=0}^{k_{max}} \frac{h(k_xL,k_yL,t)L^2}{\pi} \tag{5.26}$$

We note that, for each simulation experiment, the profile of $\langle z_{m,n}(t)z^*_{m,n}(t)\rangle$ and $\langle Re[z_{m,n}(t)]^2\rangle$ are computed based on 100 simulation runs taking place with the same process parameters (further increase in the number of simulations led to identical results for the order and the parameters of the constructed stochastic PDE).

Fig.5.2 shows an eigenspectrum identified from a thin film deposition (we note that the identified eigenvalues are considered real since the imaginary part of the eigenvalues identified turned out to be very small). It can be seen that the identified spectrum is very close to the parabolic reference curve (appears as a line

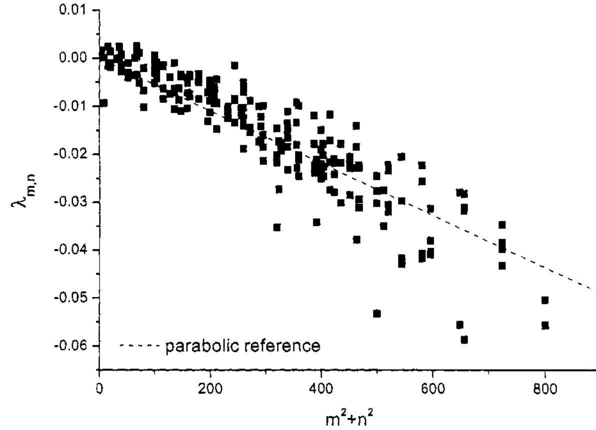

Figure 5.2: Eigenvalue spectrum of the infinite stochastic ODE systems identified from the kMC simulation of the deposition process with $W = 0.5\ 1/s$, $T = 650\ K$ and $k_{max} = 100$.

when the eigenvalue is plotted against $m^2 + n^2$). Based on Eq.5.10, this implies that a second-order stochastic PDE system of the following form would be able to describe the evolution of the surface height of this deposition process:

$$\begin{array}{ll} \dfrac{\partial h}{\partial t} = c + c_2 \bigtriangledown^2 h + \xi(x,y,t) & \\ \bigtriangledown h(0,y,t) = \bigtriangledown h(\pi,y,t), & h(0,y,t) = h(\pi,y,t), \\ \bigtriangledown h(x,0,t) = \bigtriangledown h(x,\pi,t), & h(x,0,t) = h(x,\pi,t), \\ h(x,y,0) = h_0(x,y) & \end{array} \tag{5.27}$$

in which c, c_2 and the covariance of the Gaussian noise ξ, ς, all depend on the microscopic processes and operating conditions.

Remark 5.5 *We note that it is necessary to rescale $m^2 + n^2$ with the square of the corresponding lattice size, to carry out a meaningful comparison among eigenspectrums identified from simulations using lattices of different size, and for the same reason, the covariance values should be scaled with the inverse of the square of the lattice size, $1/k_{max}^2$ (see [50] for detailed discussion).*

5.3.2 Dependence on the process parameters

We proceed now with the derivation of the parameters of the stochastic PDE of Eq.5.27. c, c_2 and ς^2 are evaluated for assorted deposition conditions and the lattice size of 100×100 (i.e., $k_{max} = 100$) is used for all the simulation runs in our study.

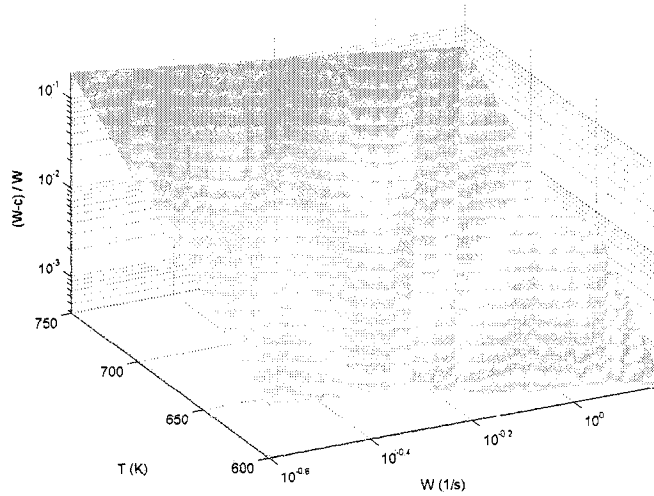

Figure 5.3: Profile of $(W-c)/W$ as a function of substrate temperature T and adsorption rate W.

Model parameter c is determined using Eq.5.18 based on the trajectory of $\langle z_{0,0}(t) \rangle$. Since $z_{0,0}(t)$ is, in fact, proportional to the average height (see Eq.5.26, i.e., the thickness of the film), c should equal the adsorption rate W when there is no desorption of surface molecules (see the process studied in [50] for example). However, desorption of surface molecules is significant in the deposition process studied in this chapter, and thus, the actual value of c should be smaller than W. Therefore, to derive the expression for c, we plot the relative difference of c and W (i.e., $(W-c)/W$) against W and T, and the result is shown in Fig.5.3. It can be seen in Fig.5.3 that $ln\left[(W-c)/W\right]$ has a quasi-linear relationship with both T

and $ln\,W$, and thus, the following expression can be obtained for c as a function of T and W through least-square fitting:

$$c(W,T) = W\left(1 - \frac{k_w}{W^{a_w} e^{-\frac{k_B T}{E_w}}}\right) \tag{5.28}$$

where $k_w = 3.3829 \times 10^{-12}$, $a_w = 0.6042$ and $E_w = 2.7 \times 10^{-3}\ eV$.

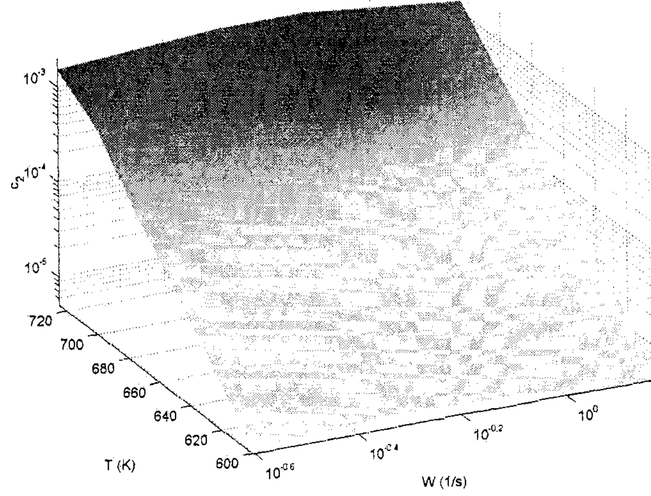

Figure 5.4: Profile of c_2 as a function of substrate temperature T and adsorption rate W.

The value of c_2 is determined by least-square fitting of Eq.5.10 and the eigen-spectrum identified from the simulation. Fig.5.4 shows the profile of c_2 as a function of T and W. It can be seen that $ln\,c_2$ has a quasi-linear relationship with both T and $ln\,W$, and thus, the following expression can be obtained for c_2 as a function of T and W through least-square fitting:

$$c_2(W,T) = \frac{k_{c0}}{W^{a_c} e^{-\frac{k_B T}{E_c}}} = \frac{k_c}{k_{max}^2 W^{a_c} e^{-\frac{k_B T}{E_c}}} \tag{5.29}$$

where $k_c = 1.0274 \times 10^{-13}$, $a_c = 0.1669$ and $E_c = 1.9 \times 10^{-3}\ eV$.

The value of ς^2 is obtained by averaging the ς^2 values determined using Eq.5.17 based on the trajectories of the second statistical moments of the states. However,

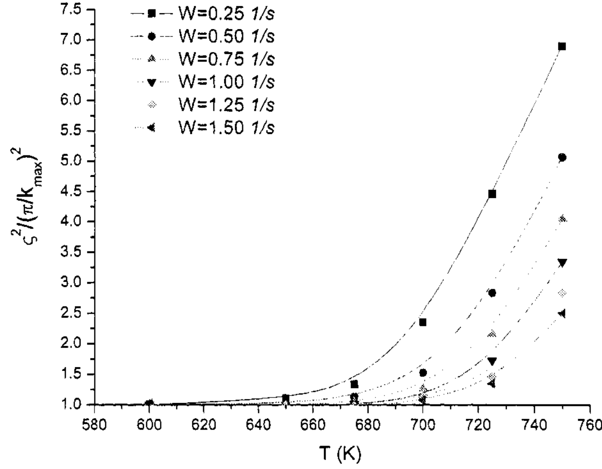

Figure 5.5: Profile of $\varsigma^2/(\pi/k_{max})^2$ as a function of substrate temperature T for different adsorption rates.

derivation of the expression of $\varsigma^2(T, W)$ is not as straightforward as the ones for c and c_2. Fig.5.5 shows the profile of the normalized ς^2 value, $\varsigma^2/(\pi/k_{max})^2$, as a function of T for different W. It can be noticed that $\varsigma^2/(\pi/k_{max})^2$ grows exponentially with W and therefore we may assume $\varsigma^2/(\pi/k_{max})^2 = 1 + e^{a_{v0} + k_{v0}T}$. Values of a_{v0} and k_{v0} are determined by least-square fitting for different W and results suggest that a_{v0} and k_{v0} are linear functions of W. Thus, the following expression is obtained for ς^2 as a function of T and W:

$$
\begin{aligned}
\varsigma^2(W, T) &= \frac{\pi^2}{k_{max}^2} W[1 + e^{-a_v - k_v W + (a_t + k_t W)T}] \\
&= \frac{\pi^2}{k_{max}^2} W[1 + \frac{e^{(a_t + k_t W)T}}{e^{a_v + k_v W}}]
\end{aligned}
\tag{5.30}
$$

where $a_v = 15.55493$, $k_v = 20.64504$, $a_t = 0.02332$ and $k_t = 0.0261$.

Therefore, the linear stochastic PDE model identified for the deposition process

is as follows:

$$
\begin{array}{l}
\dfrac{\partial h}{\partial t} = W\left(1 - \dfrac{k_w}{W^{a_w} e^{-\dfrac{k_B T}{E_w}}}\right) + \left(\dfrac{k_c}{k_{max}^2 W^{a_c} e^{-\dfrac{k_B T}{E_c}}}\right) \nabla^2 h + \xi(x,y,t) \\
\nabla h(0,y,t) = \nabla h(\pi,y,t), \quad h(0,y,t) = h(\pi,y,t), \\
\nabla h(x,0,t) = \nabla h(x,\pi,t), \quad h(x,0,t) = h(x,\pi,t), \\
h(x,y,0) = h_0(x,y)
\end{array}
\tag{5.31}
$$

where $\langle \xi(x,y,t)\xi^*(x',y',t')\rangle = \dfrac{\pi^2}{k_{max}^2} W \left[1 + \dfrac{e^{(a_t + k_t W)T}}{e^{a_v} + k_v W}\right] \delta(x-x')\delta(y-y')\delta(t-t')$.

5.3.3 Validation of stochastic PDE model

We now proceed with the validation of the stochastic PDE model of the thin film deposition process (Eq.5.31). Validation experiments are conducted for a number of deposition conditions which have not been used for the model construction. We generate surface profiles using both the stochastic PDE model and the kinetic Monte-Carlo simulation. Fig.5.6 shows the surface profile at the end of a deposition with substrate temperature $T = 610\ K$, adsorption rate $W = 0.5\ 1/s$, deposition duration of 200 s and $k_{max} = 100$; Fig.5.7 shows the surface profile at the end of a deposition with substrate temperature $T = 710\ K$, adsorption rate $W = 0.5\ 1/s$, deposition duration of 200 s and lattice size $k_{max} = 100$; we can see that both at low and high substrate temperatures, the linear stochastic PDE model constructed for the deposition process is very consistent with the kinetic Monte-Carlo simulation in terms of film thickness and surface morphology (such as surface island size distribution and aggregation). The only observable difference between the two surfaces is that the one generated by kMC simulation has finer structural details than the one generated by stochastic PDE simulation. Such

difference is caused, on the one hand, by the fact that the surface height profile in the stochastic PDE model is a continuous approximation of the discrete lattice; and on the other hand, by the error that occurs in the stochastic PDE simulation in which a finite-dimensional stochastic ODE approximation of the original stochastic PDE is used (this error can be reduced by increasing the order of the finite-dimensional approximation).

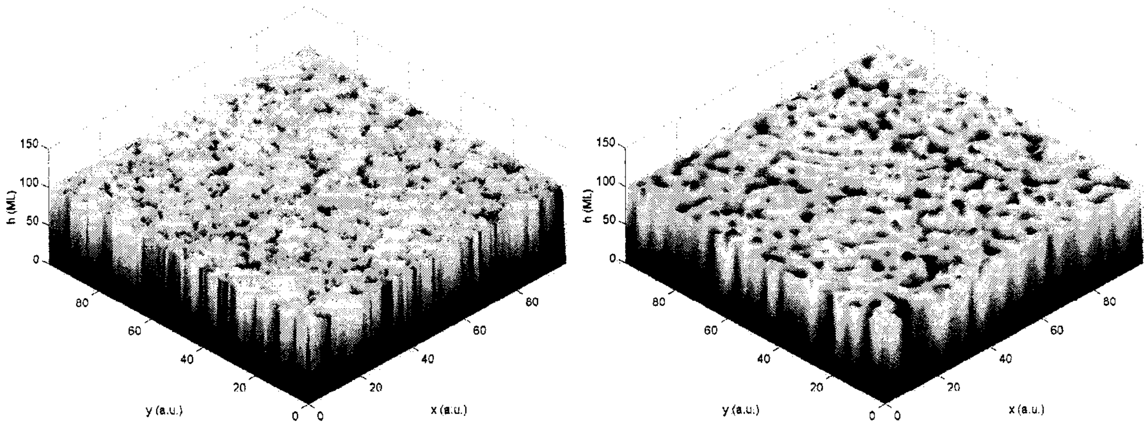

Figure 5.6: Final thin film surface profiles generated by kMC simulation (left, $k_{max} = 100$) and stochastic PDE model (right, 20×20 states) for a $200s$ deposition with substrate temperature $T = 610\ K$ and adsorption rate $W = 0.5\ 1/s$.

In addition, we generate expected surface roughness profiles using both the stochastic PDE model and the kinetic Monte-Carlo simulation (average of 100 runs) for the deposition process. For simplicity, the surface roughness is evaluated in a root-mean-square fashion as follows:

$$r(t) = \sqrt{\frac{1}{\pi} \int_0^{\pi} \int_0^{\pi} [h(x,y,t) - \bar{h}(t)]^2 dxdy} \tag{5.32}$$

where $\bar{h}(t) = \frac{1}{\pi^2} \int_0^{\pi} \int_0^{\pi} h(x,y,t) dxdy$ is the average surface height. We note that for more detailed descriptions of the surface morphology, the surface can be examined using the height-height correlation function [67] and the interface width function [1].

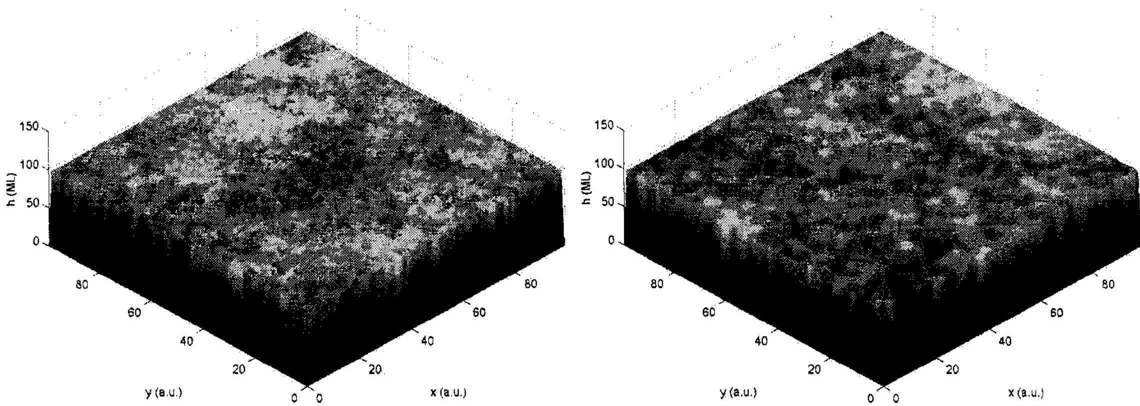

Figure 5.7: Final thin film surface profiles generated by kMC simulation (left, $k_{max} = 100$) and stochastic PDE model (right, 20×20 states) for a $200s$ deposition with substrate temperature $T = 710\ K$ and adsorption rate $W = 0.5\ 1/s$.

To calculate the expected surface roughness using the stochastic PDE model, we first expressed the surface roughness in terms of the ODE states. According to Eq.5.22, we have $\bar{h}(t) = z_{0,0}(t)\phi_{0,0}$. Therefore, $r(t)$ can be rewritten in terms of $z_{m,n}$ as follows:

$$\begin{aligned} r(t) &= \sqrt{\frac{1}{\pi^2}\int_0^\pi\int_0^\pi [h(x,y,t)-\bar{h}(t)][h(x,y,t)-\bar{h}(t)]^* dxdy} \\ &= \sqrt{\frac{1}{\pi^2}\int_0^\pi\int_0^\pi \sum_{m,n=-\infty,m^2+n^2\neq 0}^{\infty} z_{m,n}(t)\phi_{m,n}(x,y)\phi_{m,n}^*(x,y)z_{m,n}^*(t)dxdy} \\ &= \sqrt{\frac{1}{\pi^2}\sum_{m,n=-\infty,m^2+n^2\neq 0}^{\infty} z_{m,n}(t)z_{m,n}^*(t)} \end{aligned} \tag{5.33}$$

and the expected roughness can be computed as follows:

$$\langle r(t)\rangle = \sqrt{\frac{1}{\pi^2}\sum_{m,n=-\infty,m^2+n^2\neq 0}^{\infty} \langle z_{m,n}(t)z_{m,n}^*(t)\rangle} \tag{5.34}$$

Substituting Eq.5.16 and $\lambda_n = -4c_2(m^2+n^2)$ into Eq.5.34, we obtain the following expression of the trajectory of $\langle r(t)\rangle$ in terms of the parameters of the stochastic

PDE model:

$$\langle r(t)\rangle = \sqrt{\frac{1}{\pi^2}\sum_{m,n=-\infty,m^2+n^2\neq 0}^{\infty}\left[\varsigma^2\frac{e^{-8c_2(m^2+n^2)t}-1}{-8c_2(m^2+n^2)}+e^{-8c_2(m^2+n^2)t}z_{m,n,0}z^*_{m,n,0}\right]} \tag{5.35}$$

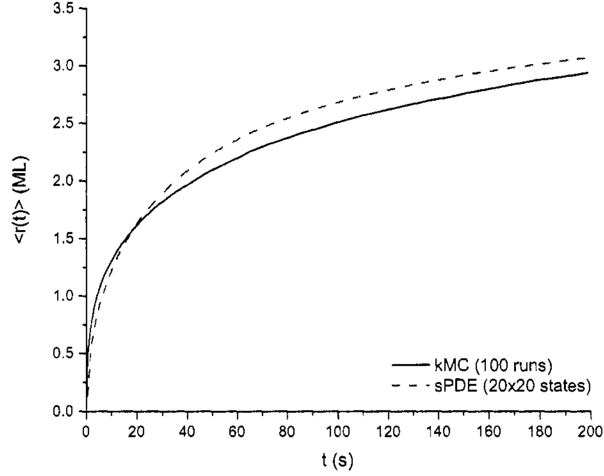

Figure 5.8: Expected surface roughness profiles generated by kMC simulation (k_{max} = 100) and stochastic PDE model for a $200s$ deposition with substrate temperature T = 610 K and adsorption rate $W = 0.5\ 1/s$.

Fig.5.8 shows the expected roughness profile of a deposition with substrate temperature $T = 610\ K$ and adsorption rate $W = 0.5\ 1/s$; Fig.5.9 shows the roughness profile of a deposition with substrate temperature $T = 710\ K$ and adsorption rate $W = 0.5\ 1/s$; we can see that the roughness profiles generated by the linear stochastic PDE model are very close to the profiles generated by the kinetic Monte-Carlo simulation, for both low and high substrate temperatures.

Furthermore, we also generate expected thin film thickness profiles using both the stochastic PDE model and the kinetic Monte-Carlo simulation (average of 100 runs) for the deposition process (shown in Fig.5.8). We can see that the thickness profiles generated by the linear stochastic PDE model are also very close to the

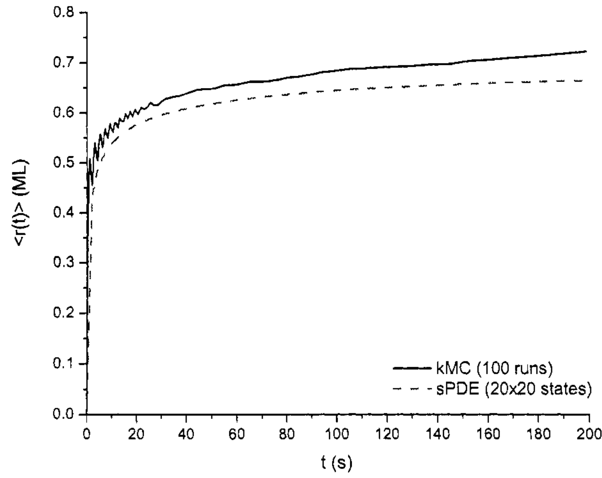

Figure 5.9: Expected surface roughness profiles generated by kMC simulation ($k_{max} = 100$) and stochastic PDE model for a $200s$ deposition with substrate temperature $T = 710\ K$ and adsorption rate $W = 0.5\ 1/s$.

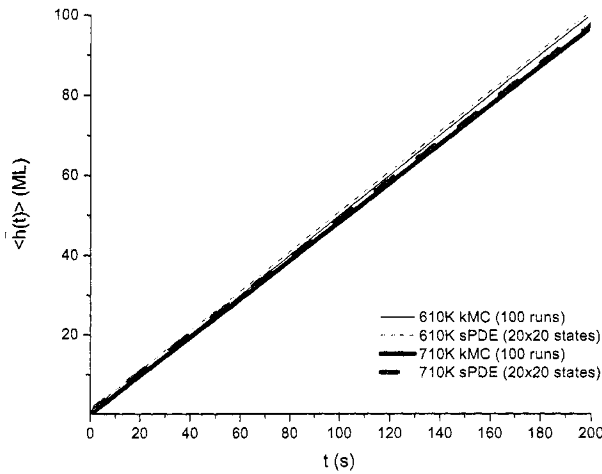

Figure 5.10: Expected thin film thickness profiles generated by kMC simulation ($k_{max} = 100$) and stochastic PDE model for: 1) a $200s$ deposition with substrate temperature $T = 610\ K$ and adsorption rate $W = 0.5\ 1/s$ (the thin lines); 2) a $200s$ deposition with substrate temperature $T = 710\ K$ and adsorption rate $W = 0.5\ 1/s$ (the thick lines).

profiles generated by the kinetic Monte-Carlo simulation, for both low and high substrate temperatures.

5.4 Feedback control

In this section, we design a multivariable state feedback controller based on the stochastic PDE model of Eq.5.31 to control the thin film thickness and surface roughness for the deposition process. The difficulty of obtaining in-situ surface measurements in real-time had been one of the obstacles for implementing feedback control system on thin film processes. Recently, researchers made possible to use some of the intrusive scanning probe based techniques such as the scanning tunneling microscopy (STM) [52] and atomic force microscopy (AFM) [45] in-situ, to observe in real-time the growth of the thin film. In [57], it was reported that a non-intrusive grazing incidence small angle x-ray scattering (GISAXS) method was successfully used to monitor the thin film growth in-situ in real-time; the method was capable of sampling large surface areas with sampling frequency up to 10 Hz and a subnanometer resolution. Such advancements in surface metrology indeed create the possibility for implementing feedback control systems which rely on real-time surface state measurements.

Since the thin film deposition is a batch process, the control objective is to control the final thin film thickness and surface roughness to the desired levels at the end of each deposition run. We use an optimization-based control problem formulation. The substrate temperature T and the adsorption rate W (W can be adjusted by varying reactor inlet gas flow rate, chamber pumping speed, etc.) are chosen to be the manipulated variables. Furthermore, since the process is stochastic in nature, the controlled variables are the expected values of the final

thin film thickness $\langle \bar{h}(t_{dep}) \rangle$ and of the surface roughness $\langle r(t_{dep}) \rangle$, where t_{dep} is the total deposition time.

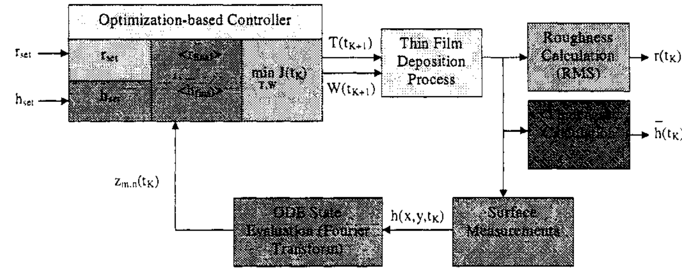

Figure 5.11: Block diagram of the closed-loop system.

Fig.5.11 shows the block diagram of the closed-loop system. The control system operates in a discrete time fashion, when the Kth real-time surface profile measurement is obtained at time t_K (i.e., $t_K = Kt_s$, where t_s is the measurement interval as well as the control interval), the states of the infinite stochastic ODE system, $z_{m,n}(t_K)$, are computed. Then, a substrate temperature $T(t_{K+1})$ and an adsorption rate $W(t_{K+1})$ are computed based on states $z_{m,n}(t_K)$ and the stochastic PDE model, under the assumption that T and W are held at designated levels for the rest of the deposition. $T(t_{K+1})$ and $W(t_{K+1})$ are then applied to the deposition process at the next measurement time t_{K+1}.

5.4.1 Predictive control design

In order to design a model-based predictive controller, we first derive the analytical expression for the trajectory of $\langle \bar{h}(t) \rangle$ and $\langle r(t) \rangle$. Due to the fact that the current deposition parameters ($T(t_K)$ and $W(t_K)$) would be used during the current control cycle before the new levels ($T(t_{K+1})$ and $W(t_{K+1})$) are applied, the estimate of the film thickness (i.e., the estimate of $\langle z_{0,0}(t_{dep}) \rangle$) and the estimate of the final surface roughness cannot be computed directly using Eqs.5.18 and 5.35

($\lambda_{m,n}$ and ς^2 are no longer constant due to the change of W and T). Therefore, we first need to derive the expressions of $z_{0,0}(t_{dep})$ and $z_{m,n}(t_{dep})$ ($m^2+n^2 \neq 0$) for this case. We consider that at time t_{K+1}, the deposition parameters are changed from $W(t_K)$ and $T(t_K)$ to $W(t_{K+1})$ and $T(t_{K+1})$ respectively. Following from Eq.5.14, we have:

$$\begin{aligned} z_{0,0}(t) &= z_{0,0}(t_0) + c^z_{0,0}(t-t_0) + \int_{t_0}^{t} \xi_{0,0}(\mu)d\mu \\ z_{m,n}(t) &= e^{\lambda_{m,n}(t-t_0)} z_{m,n}(t_0) + \int_{t_0}^{t} e^{\lambda_{m,n}(t-\mu)} \xi_{m,n}(\mu)d\mu \\ &m,n = 0,\pm 1,\cdots,\pm\infty;\ m^2+n^2 \neq 0 \end{aligned} \tag{5.36}$$

Hence, by calculating the intermediate values $z_{0,0}(t_{K+1})$ and $z_{m,n}(t_{K+1})$ ($m^2 + n^2 \neq 0$) using $z_{0,0}(t_K)$ and $z_{m,n}(t_K)$ respectively, the expressions of $z_{0,0}(t_{dep})$ and $z_{m,n}(t_{dep})$ can be derived as follows:

$$\begin{aligned} z_{0,0}(t_{dep}) &= z_{0,0}(t_K) + c^z_{0,0}(t_K)t_c + c^z_{0,0}(t_{K+1})(t_{dep}-t_{K+1}) \\ &\quad + \int_{t_K}^{t_{K+1}} \xi_{0,0}(\mu)d\mu + \int_{t_{K+1}}^{t_{dep}} \xi_{0,0}(\mu)d\mu \\ z_{m,n}(t) &= e^{\lambda_{m,n}(t_K)t_c + \lambda_{m,n}(t_{K+1})(t_{dep}-t_{K+1})} z_{m,n}(t_K) \\ &\quad + e^{\lambda_{m,n}(t_{K+1})t_c} \int_{t_K}^{t_{K+1}} e^{\lambda_{m,n}(t_K)(t_{K+1}-\mu)} \xi_{m,n}(\mu)d\mu \\ &\quad + \int_{t_{K+1}}^{t_{dep}} e^{\lambda_{m,n}(t_{K+1})(t_{dep}-\mu)} \xi_{m,n}(\mu)d\mu \\ &\quad m,n = 0,\pm 1,\cdots,\pm\infty;\ m^2+n^2 \neq 0 \end{aligned} \tag{5.37}$$

Using Result 5.1 and substituting $c^z_{0,0} = \pi c$ and $\lambda_{m,n} = -4(m^2+n^2)c_2$ (Eq.5.10), the above equations can be simplified as follows:

$$\begin{aligned} z_{0,0}(t_{dep}) &= z_{0,0}(t_K) + \pi c(t_K)t_c + \pi c(t_{K+1})(t_{dep}-t_{K+1}) \\ &\quad + \bar{\theta}_{0,0}(t_K) + \hat{\theta}_{0,0}(t_{K+1}) \\ z_{m,n}(t) &= e^{-4(m^2+n^2)\{c_2(t_K)t_c + c_2(t_{K+1})[t_{dep}-t_{K+1}]\}} z_{m,n}(t_K) \\ &\quad + \bar{\theta}_{m,n}(t_K) + \hat{\theta}_{m,n}(t_{K+1}) \\ &\quad m,n = 0,\pm 1,\cdots,\pm\infty;\ m^2+n^2 \neq 0 \end{aligned} \tag{5.38}$$

where $\bar{\theta}_{0,0}(t_K)$, $\hat{\theta}_{0,0}(t_{K+1})$, $\bar{\theta}_{m,n}(t_K)$ and $\hat{\theta}_{m,n}(t_{K+1})$ ($m^2+n^2 \neq 0$) are independent Gaussian random numbers with zero mean, and their covariances can be expressed

as follows:

$$
\begin{aligned}
&\langle\bar{\theta}_{0,0}(t_K)\bar{\theta}^*_{0,0}(t_K)\rangle = \varsigma^2(t_K)t_c \\
&\langle\hat{\theta}_{0,0}(t_{K+1})\hat{\theta}^*_{0,0}(t_{K+1})\rangle = \varsigma^2(t_{K+1})(t_{dep} - t_{K+1}) \\
&\langle\bar{\theta}_{m,n}(t_K)\bar{\theta}^*_{m,n}(t_K)\rangle = e^{-8(m^2+n^2)c_2(t_{K+1})t_c}\varsigma^2(t_K)\frac{e^{-8(m^2+n^2)c_2(t_K)t_c} - 1}{-8(m^2+n^2)c_2(t_K)} \\
&\langle\hat{\theta}_{m,n}(t_{K+1})\hat{\theta}^*_{m,n}(t_{K+1})\rangle = \varsigma^2(t_{K+1})\frac{e^{-8(m^2+n^2)c_2(t_{K+1})(t_{dep}-t_{K+1})} - 1}{-8(m^2+n^2)c_2(t_{K+1})} \\
&m,n = 0, \pm 1, \cdots, \pm\infty;\ m^2+n^2 \neq 0
\end{aligned}
\tag{5.39}
$$

Therefore, the quantities that directly relate to thickness- and roughness-estimation, $\langle z_{0,0}(t_{dep})\rangle$, $\langle z_{m,n}(t_{dep})\rangle$ and $\langle z_{m,n}(t_{dep})z^*_{m,n}(t_{dep})\rangle$, can be derived as follows:

$$
\begin{aligned}
&\langle z_{0,0}(t_{dep})\rangle = z_{0,0}(t_K) + \pi c(t_K)t_c + \pi c(t_{K+1})(t_{dep} - t_{K+1}) \\
&\langle z_{m,n}(t_{dep})\rangle = e^{-4(m^2+n^2)[c_2(t_K)t_c + c_2(t_{K+1})(t_{dep}-t_{K+1})]}z_{m,n}(t_K) \\
&\langle z_{m,n}(t_{dep})z^*_{m,n}(t_{dep})\rangle = \langle z_{m,n}(t_{dep})\rangle\langle z_{m,n}(t_{dep})\rangle^* + \langle\bar{\theta}_{m,n}(t_K)\bar{\theta}^*_{m,n}(t_K)\rangle \\
&\qquad\qquad + \langle\hat{\theta}_{m,n}(t_{K+1})\hat{\theta}^*_{m,n}(t_{K+1})\rangle \\
&m,n = 0, \pm 1, \cdots, \pm\infty;\ m^2+n^2 \neq 0
\end{aligned}
\tag{5.40}
$$

Accordingly, the expected final film thickness can be expressed as follows:

$$
\langle\bar{h}_{final}(t_K)\rangle = \frac{\langle z_{0,0}(t_{dep})\rangle}{\pi} = \frac{z_{0,0}(t_K)}{\pi} + c(t_K)t_c + c(t_{K+1})(t_{dep} - t_{K+1}) \tag{5.41}
$$

Also, by substituting the Eq.5.40 into Eq.5.34, the expected final surface roughness can be derived as follows,

$$
\begin{aligned}
\langle r_{final}(t_K)\rangle^2 &= \frac{1}{\pi^2}\sum_{m,n=-\infty;\ m^2+n^2\neq 0}^{\infty}\langle z_{m,n}(t_{dep})z_{m,n}^*(t_{dep})\rangle \\
&= \frac{1}{\pi^2}\sum_{m,n=-\infty;\ m^2+n^2\neq 0}^{\infty}[\langle z_{m,n}(t_{dep})\rangle\langle z_{m,n}(t_{dep})\rangle^* \\
&\quad +\langle\bar{\theta}_{m,n}(t_K)\bar{\theta}_{m,n}^*(t_K)\rangle + \langle\hat{\theta}_{m,n}(t_{K+1})\hat{\theta}_{m,n}^*(t_{K+1})\rangle] \\
&= \frac{1}{\pi^2}\sum_{m,n=-\infty;\ m^2+n^2\neq 0}^{\infty}\{z_{m,n}(t_K)z_{m,n}^*(t_K) \\
&\quad e^{-8(m^2+n^2)[c_2(t_K)t_c + c_2(t_{K+1})(t_{dep}-t_{K+1})]} \\
&\quad +e^{-8(m^2+n^2)c_2(t_{K+1})t_c}\varsigma^2(t_K)\frac{e^{-8(m^2+n^2)c_2(t_K)t_c}-1}{-8(m^2+n^2)c_2(t_K)} \\
&\quad +\varsigma^2(t_{K+1})\frac{e^{-8(m^2+n^2)c_2(t_{K+1})(t_{dep}-t_{K+1})}-1}{-8(m^2+n^2)c_2(t_{K+1})}\Bigg\}
\end{aligned}
\tag{5.42}
$$

Since the computation of the above equation involves infinite summations, it cannot be calculated directly in practice. A finite dimensional approximation, which only uses the first ($\pm N$th,$\pm N$th) states, is used for the computation, and is of the following form:

$$
\begin{aligned}
\langle r_{final}(t_K)\rangle^2 &= \frac{1}{\pi^2}\sum_{m,n=-N;\ m^2+n^2\neq 0}^{N}\{z_{m,n}(t_K)z_{m,n}^*(t_K) \\
&\quad e^{-8(m^2+n^2)[c_2(t_K)t_c + c_2(t_{K+1})(t_{dep}-t_{K+1})]} \\
&\quad +e^{-8(m^2+n^2)c_2(t_{K+1})t_c}\varsigma^2(t_K)\frac{e^{-8(m^2+n^2)c_2(t_K)t_c}-1}{-8(m^2+n^2)c_2(t_K)} \\
&\quad +\varsigma^2(t_{K+1})\frac{e^{-8(m^2+n^2)c_2(t_{K+1})(t_{dep}-t_{K+1})}-1}{-8(m^2+n^2)c_2(t_{K+1})}\Bigg\}
\end{aligned}
\tag{5.43}
$$

Here we note that this finite dimensional approximation can be improved by utilizing an upper bound for the residue of the infinite summation derived follow-

ing the method we proposed in our previous chapter (see Chapter 4 for detailed discussions on the convergence property of the infinite series and the determination of N for a desired approximation precision), however, such improvement is not adopted in this chapter for simplicity. Moreover, instead of direct truncation of the system of infinite dimensional stochastic ODEs, more advanced reduction techniques can be used, especially when the stochastic PDE model is nonlinear (see [16, 7] for results on nonlinear model reduction of parabolic PDEs). Therefore, the value of $T(t_{K+1})$ and $W(t_{K+1})$ are determined at each sampling time interval by solving, in the control time interval, the following optimization problem:

$$\min_{W(t_{K+1}),T(t_{K+1})} J(t_K) = q_h(h_{set} - \langle \bar{h}_{final}(t_K)\rangle)^2 + q_r(r_{set}^2 - \langle r_{final}(t_K)\rangle^2)^2 \tag{5.44}$$

subject to,

$$\langle \bar{h}_{final}(t_K)\rangle = \frac{z_{0,0}(t_K)}{\pi} + c(t_K)t_c + c(t_{K+1})(t_{dep} - t_{K+1}) \tag{5.45}$$

$$\begin{aligned} \langle r_{final}(t_K)\rangle^2 = \frac{1}{\pi^2} \sum_{m,n=-N;\ m^2+n^2\neq 0}^{N} & \{z_{m,n}(t_K)z_{m,n}^*(t_K) \\ & e^{-8(m^2+n^2)[c_2(t_K)t_c + c_2(t_{K+1})(t_{dep} - t_{K+1})]} \\ & + e^{-8(m^2+n^2)c_2(t_{K+1})t_c}\varsigma^2(K)\frac{e^{-8(m^2+n^2)c_2(t_K)t_c} - 1}{-8(m^2+n^2)c_2(t_K)} \\ & + \varsigma^2(t_{K+1})\frac{e^{-8(m^2+n^2)c_2(t_{K+1})(t_{dep}-t_{K+1})} - 1}{-8(m^2+n^2)c_2(t_{K+1})}\Bigg\} \end{aligned} \tag{5.46}$$

$$c(t_{K+1}) = W(t_{K+1})\left[1 - \frac{k_w}{W(t_{K+1})^{a_w} e^{-\frac{k_B T(t_{K+1})}{E_w}}}\right] \tag{5.47}$$

$$c_2(t_{K+1}) = \frac{k_c}{k_{max}^2 W(t_{K+1})^{a_c} e^{-\dfrac{k_B T(t_{K+1})}{E_c}}} \tag{5.48}$$

$$\varsigma^2(t_{K+1}) = \frac{\pi^2}{k_{max}^2} W(t_{K+1}) \left\{ 1 + \frac{e^{[a_t + k_t W(t_{K+1})]T(t_{K+1})}}{e^{a_v + k_v W(t_{K+1})}} \right\} \tag{5.49}$$

$$c(t_{K+1}) \geq c_{min} \tag{5.50}$$

$$T_{min} \leq T(t_{K+1}) \leq T_{max} \tag{5.51}$$

$$W_{min} \leq W(t_{K+1}) \leq W_{max} \tag{5.52}$$

where q_h and q_r are the weights of the penalties on thickness and roughness, respectively, c_{min} is the minimum growth rate, T_{min}, T_{max}, W_{min} and W_{max} are the lowest and highest substrate temperature, and the lowest and highest adsorption rate, respectively. In this study, we use $q_h = 1/h_{set}^2$, $q_r = 1/r_{set}^2$, $c_{min} = 0.1 h_{set}/t_{dep}$, $T_{min} = 400\ K$, $T_{max} = 900\ K$, $W_{min} = 0.1\ 1/s$ and $W_{max} = 2.0\ 1/s$.

We note that J corresponds to the difference between the square of the desired final surface roughness r_{set} and the square of the estimated final surface roughness $\langle r_{final} \rangle$ computed based on the current states $z_{m,n}(t_K)$. We choose to minimize the difference of the squares of the surface roughness, i.e., the mean square of the surface height, to simplify the calculation. The optimization problem is solved using a standard sequential quadratic programming (SQP) method described in [24].

Remark 5.6 *Since Eq.5.46 is a finite dimensional approximation of the predicted final surface roughness, to achieve a control precision ϵ, m should be chosen large enough for each optimization computation so that the approximation error is less than ϵ (see detailed discussion in [50]).*

Remark 5.7 *Since the control action is computed using closed-form equations, the computation cost is proportional to the number of states used, $4N^2$, but independent of the optimization horizon $t_{dep} - t$; however, to evaluate the values of the $4N^2$ states, an additional computation time of the order of $4k_{max}^2 N^2$ is needed for each surface measurement. Nevertheless, even for a lattice size that corresponds to the largest physical dimension of the sampling area that can be achieved by common surface measurement techniques (i.e., a few microns), such computation can still be completed within the control interval using currently available computing power. On the other hand, such task is almost impossible to achieve using a kMC code, whose computation cost is on the order of $k_{max}^4(t_{dep} - t)$ for merely a single run. Furthermore, we note that the evaluation of each state is independent of other states, and therefore, can be executed in parallel, while the kMC code, being a serial calculation, is unsuitable for parallel processing.*

5.4.2 Closed-loop simulations

A kMC code using a lattice size of 100×100 is used to simulate the thin film deposition process and t_c is set to be 1 s. The dimension of the finite dimensional approximation of the stochastic PDE used for optimization is $N = 10$.

Fig.5.12 shows the surface roughness and substrate temperature profiles of a closed-loop deposition process with initial substrate temperature $T = 610\ K$ and adsorption rate $W = 1.0\ 1/s$ (These initial values are picked such that, with process parameters fixed at these levels throughout the deposition, the final thickness and surface roughness of the deposited film are quite different from the

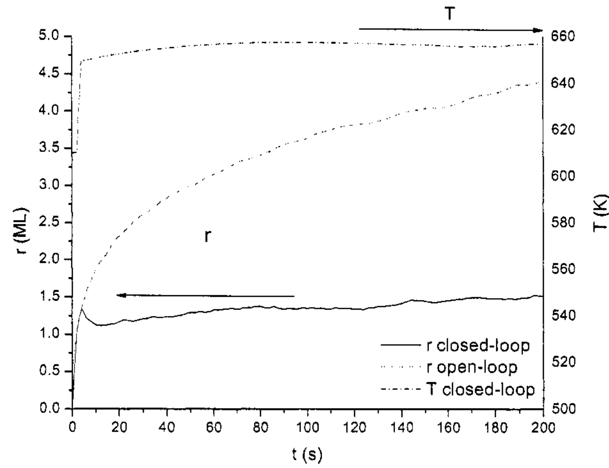

Figure 5.12: Surface roughness and substrate temperature profiles of a 200 s closed-loop deposition process with a thickness setpoint of 100 ML and a final roughness setpoint $r_{set} = 1.5\ ML$; the initial deposition conditions are $T = 610\ K$ and $W = 1.0\ 1/s$.

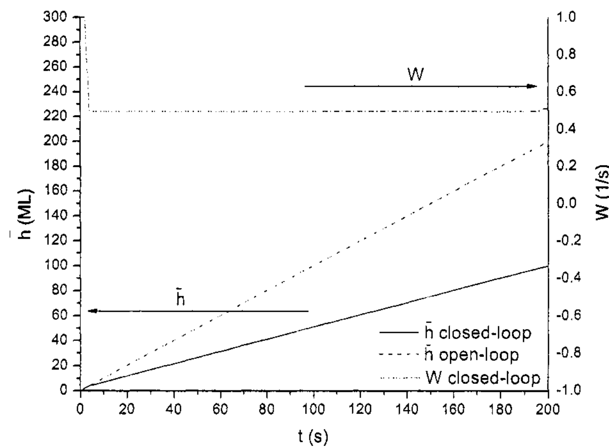

Figure 5.13: Thickness and surface adsorption rate profiles of a 200 s closed-loop deposition process with a thickness setpoint of 100 ML and a final roughness setpoint $r_{set} = 1.5\ ML$; the initial deposition conditions are $T = 610\ K$ and $W = 1.0\ 1/s$.

desired values). Fig.5.13 shows the thin film thickness and surface adsorption rate profiles of this closed-loop deposition. The control objective is to control the thin film thickness to 100 ML (*monolayers*) and to drive the final surface roughness to 1.5 ML at the end of the 200 s deposition. It can be seen that both the film thickness and the final surface roughness are controlled at the desired levels simultaneously while an open-loop deposition with the same initial deposition condition would lead to a 100% higher film thickness and a 100% higher final surface roughness as shown in Fig.5.12 and Fig.5.13.

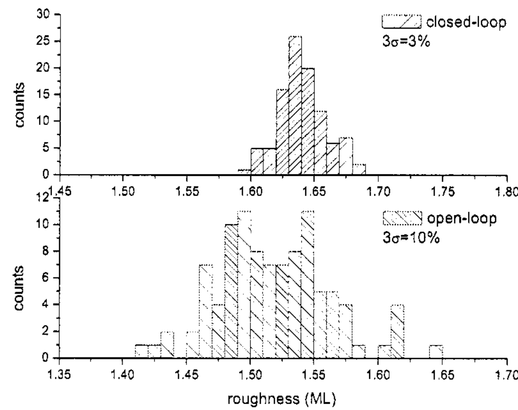

Figure 5.14: Histogram of final surface roughness of 100 closed-loop and 100 open-loop thin film depositions targeted at the same surface roughness level.

Fig.5.14 shows the final surface roughness histogram of the thin films deposited using 100 different closed-loop depositions targeting thin film thickness of 100 *monolayers* and final surface roughness of 1.65 ML and 100 different open-loop depositions with fixed substrate temperature and surface adsorption rate. The average roughness of the thin films deposited by open-loop depositions is 1.52 ML, which is quite close to the average roughness of the thin films deposited by the closed-loop depositions (1.64 ML). However, the variance among the thin films from different open-loop deposition runs is over 300% higher than that of

closed-loop depositions even though no process disturbance is considered in the simulations.

Such large variance among the films deposited by open-loop deposition can be attributed to the stochastic nature of the thin film growth process itself. Although optimal profiles of adsorption rate and substrate temperature, i.e., a well-prescribed process recipe, can be determined for the open-loop deposition, so that the average final thickness and surface roughness of the deposited films are very close to the desired levels, the stochasticity of the film growth can not be effectively handled by the pre-determined process recipes (implemented in an open-loop fashion), and therefore, results in significant film variance. On the other hand, in closed-loop depositions, as it is demonstrated in the simulation, feedback control is able to effectively compensate for the stochasticity of the process, and therefore, significantly reduce the film variance and outperform the recipe-based open-loop deposition.

5.5 Conclusions

In this chapter, we focused on a thin film deposition process which took place on a 2D lattice and was governed by three microscopic processes including molecule adsorption, surface migration and desorption. A 2D linear stochastic PDE model was initially constructed, following the methodology proposed in our previous chapter, which describes the spatio-temporal evolution of the film surface. Then, the control problem was formulated as the one of regulating the thin film thickness and surface roughness by manipulating the substrate temperature and adsorption rate. Subsequently, a computationally-efficient multivariable predictive control algorithm was developed which used a finite-dimensional approximation of the

stochastic PDE model to regulate the thin film thickness and surface roughness at desired levels at the end of the deposition. The predictive controller was then applied to the kMC simulation of the deposition process. Closed-loop system simulation results demonstrated that the model was adequately accurate and that the controller was effective in enforcing the desired control objectives and reducing the film variance caused by the stochasticity of the growth process.

Chapter 6

Conclusions and Future Work

6.1 Conclusions

This dissertation presented a comprehensive study of the application of feedback control on chemical vapor deposition processes to control the principle properties of thin films such as thickness, composition and surface roughness to enable the fabrication of smaller feature size devices.

A methodology was developed in Chapter 2 for real-time control of thin film carbon content in a PECVD process using combination of on-line gas phase measurements obtained through OES and off-line (ex-situ) measurements of film composition obtained via XPS. Using this approach, a real-time control system was developed and implemented on an experimental high density PECVD system to demonstrate the effectiveness of real-time feedback control of carbon content. Experimental results of depositions and XPS analysis of deposited thin films demonstrated the advantages of operating the process under real-time feedback control in terms of robust operation and lower carbon content.

Motivated by recent experimental results on the growth of high-κ dielectric thin

films using PECVD, a multi-component kMC model was presented in Chapter 3 for a conceptual deposition process which involves multiple gas phase species and is influenced by both short-range and long-range interactions. The dependence of the surface microstructure of the thin film on the deposition conditions was studied. Furthermore, kMC model-based feedback control schemes which used the substrate temperature to control the final surface roughness of the thin film were proposed.

Since kMC models are not available in closed-form and computationally expensive, a systematic method was proposed in Chapter 4 for the construction of linear stochastic PDE models for feedback control of surface microstructure in thin film deposition. A linear stochastic PDE model was constructed for a generic one-dimensional thin film deposition process using surface snapshots generated by kMC simulations. An optimization-based feedback controller was designed using the constructed stochastic PDE model and applied to the kMC simulation of the deposition process to control the surface roughness.

This stochastic PDE approach was then extended to two-dimensional case and applied to multivariable control problems in Chapter 5. A 2D linear stochastic PDE model was initially constructed which describes the spatio-temporal evolution of the film surface. A multivariable predictive control algorithm was developed which uses a finite-dimensional approximation of the stochastic PDE model to regulate the thin film thickness and surface roughness at desired levels at the end of the deposition.

6.2 Future work

6.2.1 Deposition plasma diagnostic study and thin films characterizations

We have used optical emission spectroscopy to investigate the correlation between the OES and the carbon concentration and the estimation model we obtained based only on one carbon containing species which in fact is not adequate to fully describe the carbon incorporation dynamics. More species could be investigated by means of OES in the future and Figure 6.1 shows the optical emission peaks and bands of the deposition plasma that could be of great interest.

Further more, due to the limitation of OES diagnostics that only excited species which emit photons during relaxation can be detected and difficult identification of complex molecules other than simple atomic of diatomic species, study of correlations between deposition plasma and other important film properties such as Zr/O ratio requires extra efforts. Quadrupole mass spectroscopy provides an excellent investigation on the species can not be monitored by OES, such as ZrO_x which are strongly correlated to ZrO_2 thin film growth, it can be used in combination with OES to provide full investigation of various species in the deposition plasma.

Comprehensive QMS study have been done to characterize the deposition plasma, figure 6.2 is mass spectra from a $ZTB/Ar/O_2$ plasma at pressure of 40 mTorr, microwave power of 300 W, and O_2/Ar flow rate ratio of 4 [14]. QMS deposition vapor characterization results have been used to investigate the deposition mechanisms, such as to reconstruct the vapor phase reaction pathways, however, the calibration of QMS data with other complementary measurements (such as OES spectra) has not been systematically formulated for the plasma

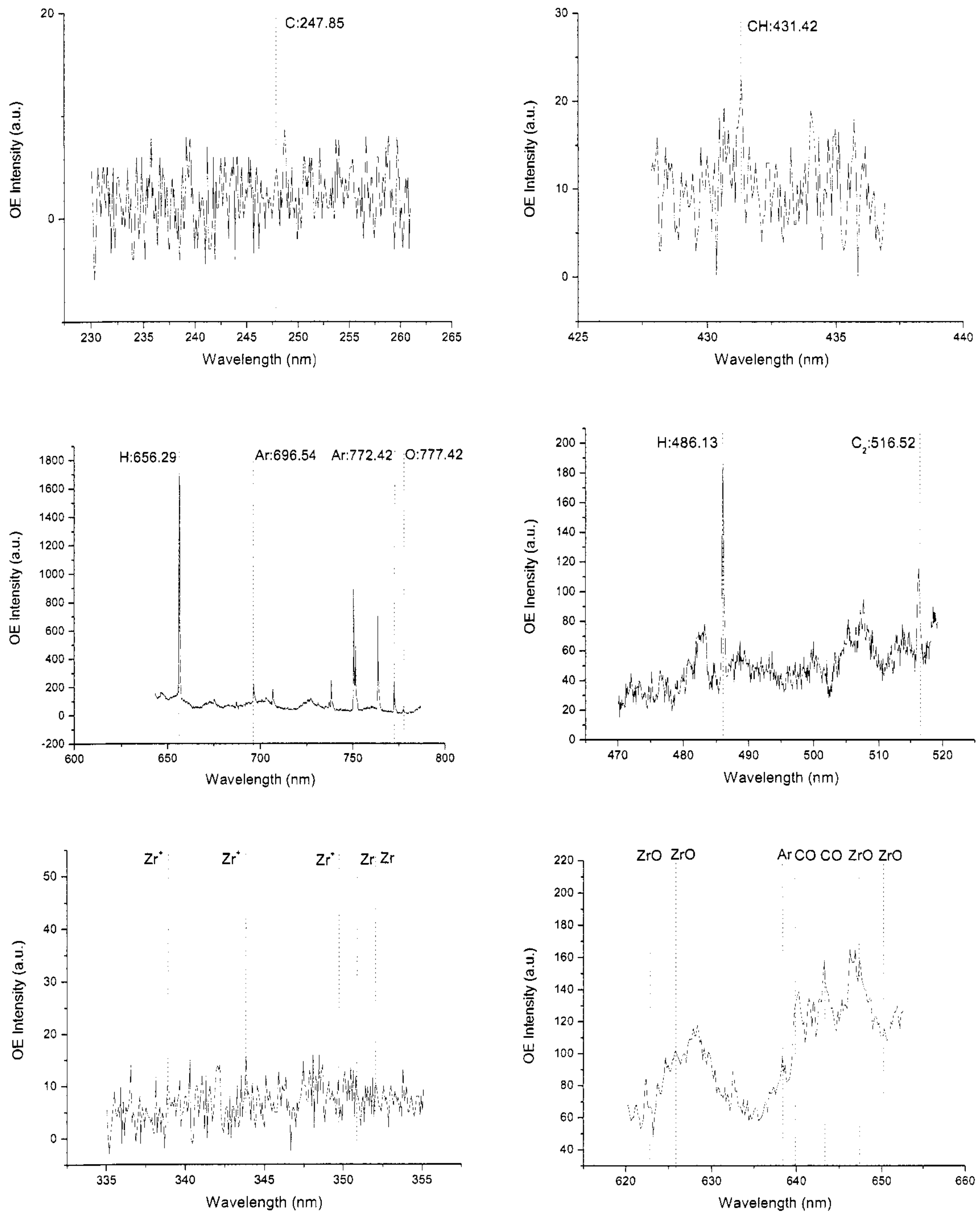

Figure 6.1: Major optical emission peaks and bands of a $ZTB/Ar/O_2$ plasma at pressure of 40 mTorr, microwave power of 300 W, and O_2/Ar flow rate ratio of 2 with no substrate bias or heating, and no silicon wafer.

deposition of high-κ thin films.

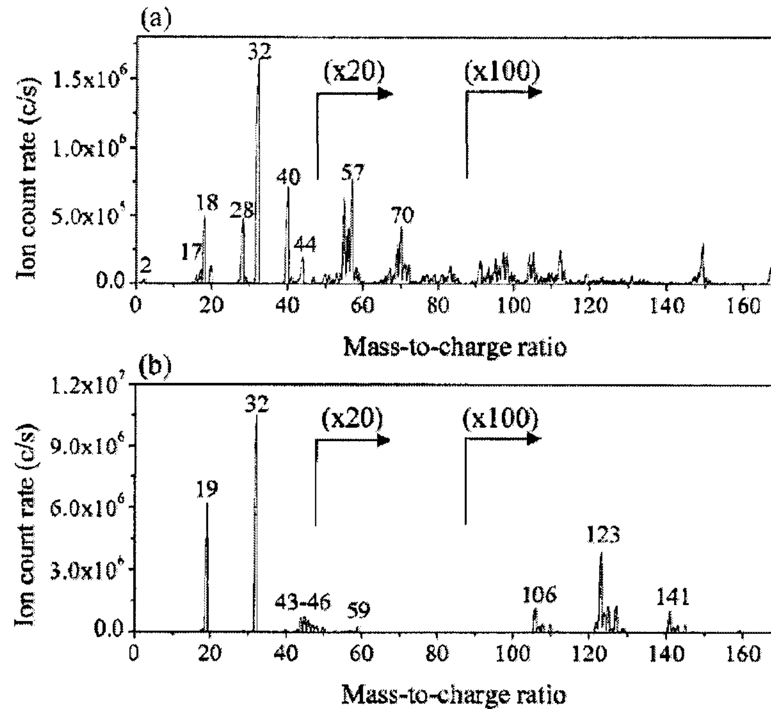

Figure 6.2: Mass spectra from a ZTB/Ar/O2 plasma [14] at pressure of 40 mTorr, microwave power of 300 W, and O_2/Ar flow rate ratio of 4. a) Neutral mass spectrum obtained by repelling plasma ions with an extractor potential of +35 V. b) Ion mass spectrum obtained by direct extraction of plasma ions with ionization filaments turned off and an extractor potential of -2 V.

By doing actinometry to the OES spectra we are able to measure the concentrations of simple atomic species in the deposition plasma, and by matching the measurements taken by QMS for the same atomic species we are able to calibrate the QMS measurements and thus obtain the concentrations of other complex molecule species which can not be quantified by OES. A mathematical model which can combined measurements by OES and QMS and compute the compositions of single atomic species C, H, O, diatomic species C_2, CH, CO, ZrO, multi-atomic species ZrO_2, ZrO_3, and other important species in the deposition plasma should

be developed in the future.

X-ray photoelectron spectroscopy is an excellent technique to characterization thin film surface composition and chemical states. Figure 6.3 shows typical peaks of major elements in a ZrO_2. However, due to the limitations of XPS that it can not differentiate functional groups shifting at the same binding energy, fourier transform infrared spectroscopy should be used as a complementary technique to quantify the hydrogen bonds in the thin film. Combined study of XPS for $C-C, C-O, Zr, Zr-O$ bonds and FTIR for hydrogen bonds such as $C-H, C-H_2, C-H_3, O-H, Zr-H$ has been done to provide a comprehensive picture of the thin film compositions and their chemical states, however, again the current combination methods are not systematically formulated.

Therefore, the development of systematic and practical frame work for merging QMS and OES, XPS and FTIR measurements for the plasma deposition of high-κ thin films will be of great interest to enable to application of these techniques for the purpose of real-time process control and fault-estimation/detection.

6.2.2 Real-time feedback control using multivariate regression model

Mathematical models to be used for optimization and real-time control of the PECVD process to maximize $Zr-O$ bonds and minimize impurities should be developed in future to enable fabrication of dielectric layers with desired material properties such as stoichiometrically full ZrO_2, and electrical properties such as high dielectric constant κ, and low fixed charge density.

Huge number of data can be obtained by OES and QMS measurements, however, only a considerably small portion of them are expected to adequately portrait the dynamics related to interested thin film properties such as compositions, which

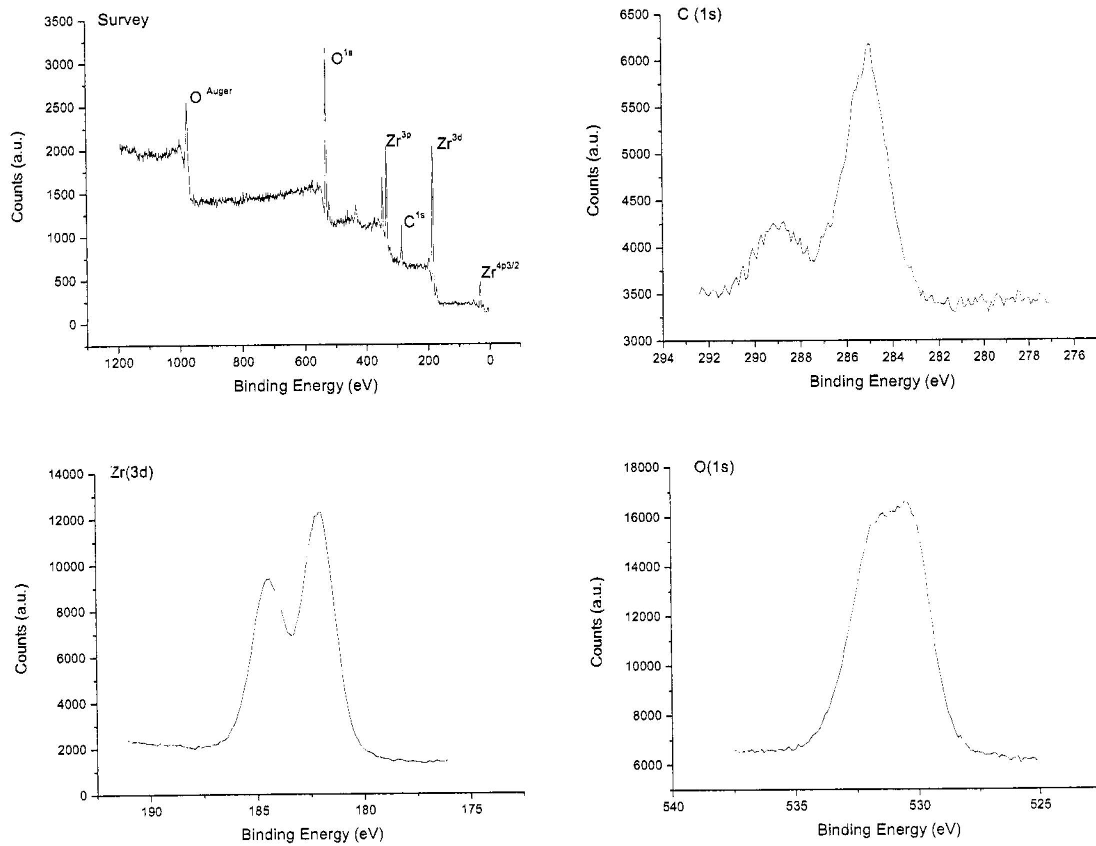

Figure 6.3: XPS spectra of a ZrO_2 thin film.

can be quantified by combined surface characterization of XPS and FTIR. To reduce the amount of measurement data to reasonably small without much loss of the prediction of the process dynamics, multivariate analysis , namely principle component (PC) analysis and partial least-square (PLS) analysis should be carried out on the experimental data to establish mathematical multivariate models to describe the relations between the plasma measurements and surface analytical results in a systematic way.

Embedding the multivariate regression models obtained from PC regression or PLS regression and simple linear regression models of the plasma in the real-time control system may requires further research for selection of various neural networks that can adapt the models with new off-line measurements. Also, special attention should be drawn on the decoupling of different control variable such as feed-in flow rate and chamber pressure. Decoupled mechanism must be adopted in the MIMO control system, and the problem of synchronizing actuators with different time constant may also need to be solved.

6.2.3 Stochastic model-based control of thin film growth

We developed a method for constructing linear stochastic PDE models using first-principle simulations and also advised methods for model-based state feedback controller design for thin film micro-structure based on stochastic PDE models has been developed. The developed methods have been successfully applied to control film thickness and surface roughness of a generic class of deposition processes.

However, thin film growth processes are usually nonlinear processes and sometimes their nonlinear dynamics significantly affect the stability and performance of these processes. Therefore, nonlinear stochastic PDE models are needed in

those cases and a method to construct stochastic PDE models with nonlinear terms should be developed to handle the nonlinear behavior of those processes. On the other hand, when the nonlinear dynamics of the processes are not important, a method to construct reduced-order linear stochastic ODE models that capture the major dynamics directly from first-principle simulations should also be an interesting research topic.

Besides the neglect of the nonlinear dynamics in our current approach, another limitation is that our controllers are all designed in a state feedback fashion. Since the state variable is a distributed variable in nature and practical measurement can only provide values of the state variable at a finite number of spatial positions, design of partial state feedback controllers based on full state estimation should be of great importance. A more challenging case would be the absence of direct state measurement, one need to design a state estimator/filter based on lumped output variable such as film thickness and surface roughness.

Bibliography

[1] J. G. Amar and F. Family. Deterministic and stochastic surface growth with generalized nonlinearity. *Phys. Rev. E*, 47:1595–1603, 1993.

[2] A. Armaou, J. Baker, and P. D. Christofides. Feedback control of plasma etching reactors for improved etching uniformity. *Chem. Eng. Sci.*, 56:1467–1475, 2001.

[3] A. Armaou and P. D. Christofides. Plasma-enhanced chemical vapor deposition: Modeling and control. *Chem. Eng. Sci.*, 54:3305–3314, 1999.

[4] A. Armaou, C. I. Siettos, and I. G. Kevrekidis. Time-steppers and 'coarse' control of distributed microscopic processes. *Int. J. Robust Nonlin. Control*, 14:89–111, 2004.

[5] K. J. Åström. *Introduction to Stochastic Control Theory.* Academic Press, New York, 1970.

[6] T. A. Badgwell, T. Breedijk, S. G. Bushman, S.W. Butler, S. Chatterjee, T. F. Edgar, A. J. Toprac, and I. Trachtenberg. *Comp. Chem. Eng.*, 19(1):1–14, 1995.

[7] J. Baker and P. D. Christofides. Finite dimensional approximation and control of nonlinear parabolic PDE systems. *Int. J. Contr.*, 73:439–456, 2000.

[8] K. S. Balakrishnana and T. F. Edgar. *Thin Solid Films*, 365, 2000.

[9] C. C. Battaile and D. J. Srolovitz. Kinetic Monte Carlo simulation of chemical vapor deposition. *Annu. Rev. Mater. Res.*, 32:297–319, 2002.

[10] E. Celik, J. Schwartz, E. Avci, H.J. Schneider-Muntau, and Y.S. Hascicek. *IEEE Tran. Appl. Superconductivity*, 9(2):2264–2267, 1999.

[11] C. Chaneliere, J. L. Autran, R. A. B. Devine, and B. Balland. Tantalum pentoxide (Ta_2O_5) thin films for advanced dielectric applications. *Mater. Sci. Eng., R.*, 22:269–322, 1998.

[12] B. Cho, J. P. Chang, J. Min, S. H. Moon, Y. W. Kim, and I. Levin. Material characteristics of electrically tunable zirconium oxide thin films. *J. Appl. Phys.*, 93:745–749, 2003.

[13] B. O. Cho, S. Lao, L. Sha, and J. P. Chang. Spectroscopic study of plasma using zirconium tetra-tert-butoxide for the plasma enhanced chemical vapor deposition of zirconium oxide. *J. Vac. Sci. Tech. A*, 19(6):2751, 2001.

[14] B. O. Cho, J. Wang, and J. P. Chang. Metalorganic precursor decomposition and oxidation mechanisms in plasma-enhanced ZrO_2 deposition. *J. Appl. Phys.*, 92(8):4238, 2002.

[15] P. D. Christofides. *Nonlinear and Robust Control of Partial Differential Equation Systems: Methods and Applications to Transport-Reaction Processes.* Birkhäuser, Boston, 2001.

[16] P. D. Christofides and P. Daoutidis. Finite-dimensional control of parabolic PDE systems using approximate inertial manifolds. *J. Math. Anal. Appl.*, 216:398–420, 1997.

[17] J. W. Coburn and M. Chen. Optical emission spectroscopy of reactive plasmas: A method for correlating emission intensities to reactive particle density. *J. Appl. Phys.*, 51(6):3134, 1980.

[18] M. Copel, M. Gribelyuk, and E.P. Gusev. Structure and stability of ultrathin zirconium oxide layers on Si(001). *Appl. Phys. Lett.*, 76:436–438, 2000.

[19] D. R. Coughanowr. *Process Systems Analysis and Control.* McGraw-Hill, New York, 1991.

[20] S. F. Edwards and D. R. Wilkinson. The surface statistics of a granular aggregate. *Proc. R. Soc. Lond. A*, 381:17–31, 1982.

[21] T. L. Einstein. *Handbook of Surface Science*, volume 1, chapter 11, pages 577–650. Elsevier, Amsterdam, 1996.

[22] I. L. Eisgruber, J. R. Engel, R. E. Hollingsworth, P. K. Bhat, and R. Wendt. Intelligent process control of indium tin oxide sputter deposition using optical emission spectroscopy. *J. Vac. Sci. Tech. A*, 17(1):190, 1999.

[23] K. A. Fichthorn and W. H. Weinberg. Theoretical foundations of dynamic Monte Carlo simulations. *J. Chem. Phys.*, 95:1090–1096, 1991.

[24] R. Fletcher. *Practical methods of optimization.* John Wiley & Sons, second edition, 1987.

[25] M. G. Flynn, R. Smith, P. Abraham, and S. DenBaars. *IEEE Tran. Control. Sys. Technol.*, 9(5), 2001.

[26] H. J. Frenck, E. Oesterschulze, R. Beckmann, W. Kulisch, and R. Kassing. Low temperature remote plasma-enhanced deposition of thin metal oxide films by decomposition of metal alkoxides. *Mater. Sci. Eng., A*, 139:394–400, 1991.

[27] M. A. Gallivan and R. M. Murray. Reduction and identification methods for Markovian control systems, with application to thin film deposition. *Int. J. Robust Nonlin. Control*, 14:113–132, 2004.

[28] P. E. Gill, W. Murray, M. A. Saunders, and M. H. Wright. Procedures for optimization problems with a mixture of bounds and general linear constraints. *ACM Trans. Math. Software*, 10:282–298, 1984.

[29] D. T. Gillespie. A general method for numerical simulating the stochastic time evolution of coupled chemical reactions. *J. Comp. Phys.*, 22:403–434, 1976.

[30] G. H. Gilmer, H. Huang, and C. Roland. Thin film deposition: fundamentals and modeling. *Comp. Mater. Sci.*, 12:354–380, 1998.

[31] Y. Ide, H. Era, and K. Kishitake. Formation and properties of cr-n films by dc reactive sputtering. *J. Jap. Inst. Metals*, 65(6):502, 2001.

[32] H. Iwai and H. S. Momose. Ultra-thin gate oxides performance and reliability. *IEDM Tech. Dig.*, pages 163–166, 1998.

[33] M. A. Katsoulakis, A. J. Majda, and D. G. Vlachos. Coarse-grained stochastic processes and Monte Carlo simulations in lattice systems. *J. Comp. Phys.*, 186:250–278, 2003.

[34] T. J. Knight, D. W. Greve, X. Cheng, and B. H. Krogh. Real-time multivariable control of pecvd silicon nitride film properties. *IEEE Trans. Semiconduct. Manufact.*, 10(1):137, 1997.

[35] E. Kreyszig. *Advanced Engineering Mathematics.* John Wiley & Sons, sixth edition, 1988.

[36] R. Lam and D. G. Vlachos. Multiscale model for epitaxial growth of films: Growth mode transition. *Phys. Rev. B*, 64:035401, 2001.

[37] K. B. Lauritsen, R. Cuerno, and H. A. Makse. Noisy Kuramote-Sivashinsky equation for an erosion model. *Phys. Rev. E*, 54:3577–3580, 2003.

[38] H. H. Lee. *Fundamentals of microelectronics processing.* McGraw-Hill, New York, 1990.

[39] S. H. Lo, D. A. Buchanan, Y. Taur, and W. Wang. Quantum-mechanical modeling of electron tunneling current from the inversion layer of ultra-thin-oxide nMOSFET's. *IEEE Electron. Device Lett.*, 18:209–211, 1997.

[40] Y. Lou and P. D. Christofides. Estimation and control of surface roughness in thin film growth using kinetic Monte-Carlo models. *Chem. Eng. Sci.*, 58:3115–3129, 2003.

[41] Y. Lou and P. D. Christofides. Feedback control of growth rate and surface roughness in thin film growth. *AIChE J.*, 49:2099–2113, 2003.

[42] Y. Lou and P. D. Christofides. Feedback control of surface roughness in sputtering processes using the stochastic Kuramoto-Sivashinsky equation. *Comp. & Chem. Eng.,* in press, 2005.

[43] Y. Lou and P. D. Christofides. Feedback control of surface roughness of GaAs (001) thin films using kinetic Monte-Carlo models. *Comp. & Chem. Eng.*, 29:225–241, 2005.

[44] Y. Lou and P. D. Christofides. Feedback control of surface roughness using stochastic PDEs. *AIChE J.*, 51:345–352, 2005.

[45] G. Z. Mao, L. Lobo, R. Scaringe, and M. D. Ward. Nanoscale visualization of crystal habit modification by atomic force microscopy. *Chem. Mater.*, 9:773–783, 1997.

[46] M. Marsili, A. Maritan, F. Toigo, and J. R. Banavar. Stochastic growth equations and reparametrization invariance. *Rev. Mod. Phys.*, 68:963–983, 1996.

[47] F. Maury, L. Gueroudji, and C. Vahlas. Selection of metalorganic precursors for MOCVD of metallurgical coatings: Application to Cr-based coatings. *Surf. Coat. Technol.*, 87:316–324, 1996.

[48] M. L. Merrick, W. Luo, and K. A. Fichthorn. Substrate-mediated interactions on solid surfaces: theory, experiment, and consequences for thin-film morphology. *Prog. Surf. Sci.*, 72:117–134, 2003.

[49] J. F. Moulder, K. D. Bomben, P. E. Sobol W. F. Stickle, and J. Chastain. *Handbook of X-Ray Photoelectron Spectroscopy: A Reference Book of Standard Spectra for Identification and Interpretation of XPS Data.* Perkin-Elmer, Physical Electronics Division, 1992.

[50] D. Ni and P. D. Christofides. Construction of stochastic PDEs for feedback control of surface roughness in thin film deposition. *Int. J. Robust. Nonlin. Control,* accepted, 2005.

[51] D. Ni and P. D. Christofides. Multivariable predictive control of thin film deposition using a stochastic PDE model. *Ind. Eng. Chem. Res.,* in press, 2005.

[52] Y. Nitta, M. Shibata, K. Fujita, and M. Ichikawa. Nanometer-scale *Ge* selective growth on $Si(001)$ using ultrathin SiO_2 film. *Surf. Sci.*, 462:587–593, 2000.

[53] S. Park, D. Kim, and J. Park. Derivation of continuum stochastic equations for discrete growth models. *Phys. Rev. E*, 65:015102(R), 2002.

[54] R. W. B. Pearse and A. G. Gaydon. *The Identification of Molecular Spectra.* Wiley, New York, 1976.

[55] C. Rebholz, J.M. Schneider, H. Ziegele, B. Rahle, A. Leyland, and A. Matthews. Deposition and characterisation of carbon-containing tungsten coatings prepared by reactive magnetron sputtering. *Vacuum*, 49(4):265, 1998.

[56] J. S. Reese, S. Raimondeau, and D. G. Vlachos. Monte Carlo algorithms for complex surface reaction mechanisms: Efficiency and accuracy. *Journal of Computational Physics*, 173:302–321, 2001.

[57] G. Renaud, R. Lazzari, C. Revenant, A. Barbier, M. Noblet, O. Ulrich, F. Leroy, J. Jupille, Y. Borensztein, C. R. Henry, J. P. Deville, F. Scheurer, and J. Mane-Mane. Real-time monitoring of growing nanoparticles. *Science*, 300:1416–1419, 2003.

[58] M. Ritala, M. Leskel, J. Dekker, C. Mutsaers 2, P.J. Soininen, and J. Skarp. *Chem. Vap. Deposition*, 5(1):7–9, 1999.

[59] M. Ritala, M. Leskela, E. Rauhala, and P. Haussalo. *J. Electrochem. Soc.*, 142, 1995.

[60] S. M. Rossnagel, A. Sherman, and F. Turner. *J. Vac. Technol. B*, 18(4), 2000.

[61] D. Shi, M. Li, and P. D. Christofides. Metco diamond jet HVOF thermal spray: Rule-based modeling of coating microstructure. *Ind. Eng. Chem. Res.* in press, 2004.

[62] T. Shitara, D. D. Vvedensky, M. R. Wilby, J. Zhang, J. H. Neave, and B. A. Joyce. Step-density variations and reflection high-energy electron-diffraction intensity oscillations during epitaxial growth on vicinal GaAs(001). *Physical Review B*, 46:6815–6824, 1992.

[63] C. I. Siettos, A. Armaou, A. G. Makeev, and I. G. Kevrekidis. Microscopic/stochastic timesteppers and "coarse" control: a KMC example. *AIChE J.*, 49:1922–1926, 2003.

[64] A. R. Striganov and N. S. Sventitskii. *Tables of Spectral Lines of Neutral and Ionized Atoms.* IFI/Plenum, New York, 1968.

[65] T. Suntola. *Handbook of Thin Film Process Technology.* Institute of Physics, London, 1995.

[66] W. J. Campbell C. Pfeiffer C. Bode S. B. Hwang K. S. Balakrishnan J. Hahn T. F. Edgar, S. W. Butler. *Automatica*, 36:1567–1603, 2000.

[67] M. E. Taylor and H. A. Atwater. Monte Carlo simulations of epitaxial growth: comparison of pulsed laser deposition and molecular beam epitaxy. *Appl. Surf. Sci.*, 127:159–163, 1998.

[68] J. W. Uhm, S. S. Lee, J. W. Lee, T. H. Cha, K. S. Yi, Y. D. Kim, and H. Jeon. *J. Korean Phys. Soc.*, 35, 1999.

[69] C. Vahlas, F. Maury, and L. Gueroudji. A thermodynamic approach to the CVD of chromium and of chromium carbides starting from Cr(C_6H_6)(2). *Chem. Vap. Deposition*, 4:69–76, 1998.

[70] D. G. Vlachos. Multiscale integration hybrid algorithms for homogeneous-heterogeneous reactors. *AIChE J.*, 43:3031, 1997.

[71] D. D. Vvedensky. Edwards-Wilkinson eqaution from lattice transition rules. *Phys. Rev. E*, 67:025102(R), 2003.

[72] D. D. Vvedensky, A. Zangwill, C. N. Luse, and M. R. Wilby. Stochastic equations of motion for epitaxial growth. *Phys. Rev. E*, 48:852–862, 1993.

[73] S. C. Warnick and M. A. Dahleh. *IEEE Tran. Control. Sys. Technol.*, 6(1), 1998.

[74] B. Yu, H. Wang, C. Ricobene, Q. Xiang, and M. R. Lin. *VLSI Tech. Dig.*, pages 39–40, 2000.

[75] Z. H. Zhou and R. Reif. Epi-film thickness measurements using emission fourier transferm infrared spectroscopy-part ii: Real-time in situ process monitoring and control. *IEEE Trans. Semiconduct. Manufact.*, 8(3):340, 1995.